

NQ

3 9 5 8 4

U M I
MICROFILMED 1999

INFORMATION TO USERS

This manuscript has been reproduced from the microfilm master. UMI films the text directly from the original or copy submitted. Thus, some thesis and dissertation copies are in typewriter face, while others may be from any type of computer printer.

The quality of this reproduction is dependent upon the quality of the copy submitted. Broken or indistinct print, colored or poor quality illustrations and photographs, print bleedthrough, substandard margins, and improper alignment can adversely affect reproduction.

In the unlikely event that the author did not send UMI a complete manuscript and there are missing pages, these will be noted. Also, if unauthorized copyright material had to be removed, a note will indicate the deletion.

Oversize materials (e.g., maps, drawings, charts) are reproduced by sectioning the original, beginning at the upper left-hand corner and continuing from left to right in equal sections with small overlaps. Each original is also photographed in one exposure and is included in reduced form at the back of the book.

Photographs included in the original manuscript have been reproduced xerographically in this copy. Higher quality 6" x 9" black and white photographic prints are available for any photographs or illustrations appearing in this copy for an additional charge. Contact UMI directly to order.

UMI[®]

Bell & Howell Information and Learning
300 North Zeeb Road, Ann Arbor, MI 48106-1346 USA
800-521-0600

UNIVERSITY OF ALBERTA

Understanding Fluidic Mechanics
and its Application to Integrating Calibration
with On-chip Immunological Reactions

by

Xiangming Charmaine Qiu



A Thesis submitted to the Faculty of Graduate Studies and Research
in partial fulfillment of the requirements of the degree of

Doctor of Philosophy

Department of Chemistry

Edmonton, Alberta
Spring 1999



National Library
of Canada

Acquisitions and
Bibliographic Services

395 Wellington Street
Ottawa ON K1A 0N4
Canada

Bibliothèque nationale
du Canada

Acquisitions et
services bibliographiques

395, rue Wellington
Ottawa ON K1A 0N4
Canada

Your file Votre référence

Our file Notre référence

The author has granted a non-exclusive licence allowing the National Library of Canada to reproduce, loan, distribute or sell copies of this thesis in microform, paper or electronic formats.

The author retains ownership of the copyright in this thesis. Neither the thesis nor substantial extracts from it may be printed or otherwise reproduced without the author's permission.

L'auteur a accordé une licence non exclusive permettant à la Bibliothèque nationale du Canada de reproduire, prêter, distribuer ou vendre des copies de cette thèse sous la forme de microfiche/film, de reproduction sur papier ou sur format électronique.

L'auteur conserve la propriété du droit d'auteur qui protège cette thèse. Ni la thèse ni des extraits substantiels de celle-ci ne doivent être imprimés ou autrement reproduits sans son autorisation.

0-612-39584-7

Canada

University of Alberta

Library Release Form

NAME OF AUTHOR: **Xiangming Charmaine Qiu**

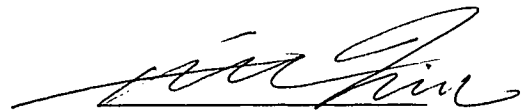
TITLE OF THESIS: **Understanding Fluid Mechanics and its Application
to Integrating Calibration with On-chip
Immunological Reactions**

DEGREE: **Doctor of Philosophy**

YEAR THIS DEGREE GRANTED: **1999**

Permission is hereby granted to the University of Alberta Library to reproduce single copies of this thesis and to lend or sell such copies for private, scholarly, or scientific research purposes only.

The author reserves all other publication and other rights in association with the copyright in the thesis, and except as hereinbefore provided, neither the thesis nor any substantial portion thereof may be printed or otherwise reproduced in any material form whatsoever without the author's prior written permission.



X. Charmaine Qiu
#6, 8616-108 st
Edmonton, AB
T6E 4M4

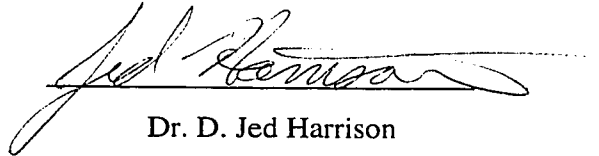
Date: November 17, 1998

University of Alberta

Faculty of Graduate Studies and Research

The undersigned certify that they have read, and recommend to the Faculty of Graduate Studies and Research for acceptance, a thesis entitled **Understanding Fluid Mechanics and its Application to Integrating Calibration with On-chip Immunological Reactions** submitted by **Xiangming Charmaine Qiu** in partial fulfillment of the requirements for the degree of **Doctor of Philosophy**.

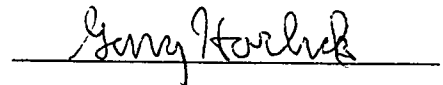
Supervisor



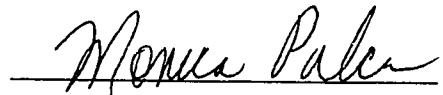
Dr. D. Jed Harrison



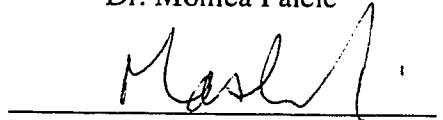
Dr. Norman J. Dovichi



Dr. Gary Horlick

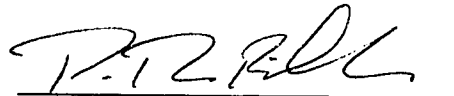


Dr. Monica Palcic



Dr. Jacob Masliyah

External Examiner



Dr. Peter Fielden

Oct. 21, 1998

*To my parents, my brothers, and my son
for their love and support*

Abstract

In the past few years much attention has been given to performing separations in microfabricated devices. Of all the reported μ -TAS chip devices, those based on electrically driven separations such as capillary electrophoresis have been the most successful. The power of these devices lies not only in the highly efficient, rapid separations, but also in the very precise, valveless fluid manipulation in the etched microchannel networks. While the demand for these devices continues to increase and the commercialization as analysis tool is underway, the challenges remaining are better understanding of the fluidic mechanism in the microfabricated channels and fully automation on-chip.

As applications for microfluidic systems become increasingly complex, design techniques based on the fluidic mechanism inside the microfabricated channel networks are essential to quality solvent delivery and mixing. We present here the experimental results from channels with a “T” intersection showing how the fluidic flow behavior would be affected by the side channel length and its location on the main channel. We also showed the deviation of the measured dye velocity from the simple electroosmotic prediction when the fluid had imbalanced ζ potential inside the system. Our results are comparable to the fluidic model prediction.

The chemical processing for complete on-chip immunoassays has been achieved. The integrated immunoreactor, which incorporates a method for performing on-chip calibration, on-chip mixing, reaction and separation of immunoreagents, samples and products are presented. This platform contains on-chip calibration standards for routing

quantitation of samples and for internal calibration dilution. The success of this on-board calibration demonstrated the precise fluid control on the microfabricated channels, and promised the potential possibility of fully automation on chip.

Acknowledgments

I find myself indebted to so many people that my acknowledgments could be extended to several pages. I would like to express my sincere gratitude to all of them who have assisted me during the time I was pursuing my Ph.D. program in University of Alberta. Here in particular, I would like to mention the following.

First and uppermost, I would like to thank my supervisor, Professor D. Jed Harrison. Without his introduction and the guidance, I could have never accomplished the thesis work in this exciting and promising research field. I am truly grateful for all he has done for me in all these years.

My sincere thanks go to the fellow members in Professor Harrison's research group for their support and sharing experience and knowledge. Special thanks to Loranelle Shultz-lockyear, who volunteered to read my very early drafts of two chapters and gave me encouragement as well the constructive suggestions for clear scientific writing; to Thompson Tang, who helped me with the instrument connections and program writings when I joined this group; to Gregor Ocvirk, who assisted me searching for any web informations that I needed desperately and immediately; to Cameron Skinner, who helped my thesis formatting; to Guifeng Jiang for being good friend and sharing all the enjoyable weekends as well the delicious food together.

I wish to express my gratitude to Dr. N. Dovichi, Dr. G. Horlick, Dr. M. Palcic, Dr. J. Masliyah, and Dr. P. Fielden for being my examining committee, their constructive comments and suggestions are highly appreciated. My thanks also extended to the technical support staff in the chemistry general office, electronic shop,

glass shop, and machine shop. I am grateful to Alberta Microelectronic Center (AMC) for the device fabrication and allowing my accessing their facilities for glass etching, device inspection, high pressure washing and other procedures of the microfabrication.

I am indebted to my parents and my brothers for their constant love and support. I appreciate the sacrifices and bearing of my son, who admires scientists, as he is the inspiration for, but seldom the frustration behind this thesis work.

Finally, the financial supports for these research projects, which were from National Sciences and Engineering Research Council (NSERC) of Canada, and Defense Advanced Research Project Agent (DARPA) of USA are greatly appreciated.

Table of Contents

UNDERSTANDING FLUIDIC MECHANICS AND ITS APPLICATION TO INTEGRATING CALIBRATION WITH ON-CHIP IMMUNOLOGICAL REACTIONS.....	
ABSTRACT.....	
ACKNOWLEDGMENTS.....	
LIST OF TABLES.....	
LIST OF FIGURES.....	
CHAPTER 1 INTRODUCTION	1
<i>1.1 Introduction</i>	1
<i>1.2 Capillary Electrophoresis</i>	4
1.2.1 Electrophoretic and electroosmotic mobilities	8
1.2.2 Electroosmosis and double layer theory.....	10
1.2.3 Electrolyte system and ζ potential dependence	16
<i>1.2.3.1 Buffer pH</i>	17
<i>1.2.3.2 Ionic strength</i>	18
<i>1.2.3.3 Organic additives and surfactants</i>	19
<i>1.2.3.4 Effect of applied voltage on mobility</i>	20
<i>1.2.3.5 Column material and treatment</i>	21
1.2.4 Separation Efficiency and Resolution	22

1.3 Micromachining.....	25
1.4 Mathematical Formulation	29
1.5 Immunoassay	31
1.5.1 Antibody	32
1.5.2 Antigen	35
1.6 Scope of Thesis.....	35
References	39

CHAPTER 2 UNDERSTANDING FLUID MECHANICS WITHIN MICROFLUIDIC DEVICE44

Abstract.....	44
2.1 Introduction.....	45
2.2 Theory.....	48
2.2.1 Definitions of different velocities used in this chapter	48
2.2.2 The model	48
2.3 Experimental Section.....	55
2.3.1 Device fabrication	55
2.3.2 Device design.....	58
2.3.3 Instrument	60
2.3.4 Materials and reagents	62
2.3.5 Operating procedure.....	63
2.4 Results and Discussions.....	64
2.4.1 Electroosmotic mobility.....	64
2.4.1.1 Electroosmotic mobility study from capillary.....	65

2.4.1.2 Electroosmotic mobility on chip	68
2.4.2 Velocity measurement.....	73
2.4.2.1 Particle counting.....	73
2.4.2.2 Fluorescein-based velocity calibration curve.....	79*
2.4.3 Leakage from floating side channel.....	81
2.4.4 Calculations of potential and flow for a potential controlled side channel	86
2.4.5 Side channel length effect	89
2.4.5.1 Side channels located 10.0 mm from the inlet of the main channels.....	91
2.4.5.2 Side channels locate at the center of the main channels.....	93
2.4.5.3 Side channels locate at the 38.0 mm from the inlet of the main channels	94
2.4.6 Fixed side channel length and varying the intersection positions.....	101
2.4.6.1 Short side channel length of 10.0 mm.....	101
2.4.6.2 Side channel length of 20.0 mm.....	102
2.4.6.3 Long side channel length of 40.0 mm	104
2.5 Conclusion.....	108
References	110

CHAPTER 3 VELOCITY DEPENDENCE ON EOF AND MIXING WITH IMBALANCED

ZETA POTENTIALS	113
Abstract.....	113
3.1 Introduction.....	114

3.2 Theory.....	115
3.3 Experimental Section.....	119
3.3.1 Device fabrication	119
3.3.2 Instrumentation	119
3.3.3 Materials and reagents	119
3.3.4 Operation procedure.....	120
3.4 Results and Discussion	122
3.4.1. Dye velocity at different pH.....	122
3.4.1.1 Dye velocity change with main channel buffer pH--Side channel floating	122
3.4.1.2 Dye velocity change with buffer pH--controlled side channel.....	128
3.4.2 Dependence of dye velocity at different side channel length.....	136
3.4.3. Mixing pattern and its dependence on ζ potential	140
3.4.4. Flow “misbehavior”--no EOF.....	144
3.5 Conclusion.....	147
References	148

CHAPTER 4 INTEGRATED CALIBRATION WITH ON-BOARD IMMUNOLOGICAL

REACTION.....	150
Abstract.....	150
4.1 Introduction.....	151
4.2 Theoretical Calculation	153
4.3 Experimental Section.....	157

4.3.1 Device fabrication.....	157
4.3.2 Instrumentation	158
4.3.3 Materials and reagents	159
4.3.4 Set-up and operation	160
4.3.4.1. <i>Mixing/dilution of FITC-Arginine</i>	160
4.3.4.2. <i>Integrated calibration of on-chip immunological reaction</i>	166
4.4 Results and Discussions.....	168
4.4.1 Mixing/dilution of FITC-Arginine.....	168
4.4.1.1 <i>Mixing measurement</i>	168
4.4.1.2 <i>Peak height/area change with concentration</i>	171
4.4.2 Integrated calibration of on-chip immunological reaction.....	175
4.4.2.1 <i>Calibration curve</i>	175
4.4.2.2 <i>Samples with known concentrations measured by the calibration</i> <i>curve</i>	187
4.4.3 Assessment of sample carryover.....	192
4.5 Conclusion.....	194
References	195
CHAPTER 5 CONCLUSIONS AND SUGGESTIONS FOR FUTURE WORK	196

List of Tables

Table 2-1 Definitions and Reduced Variables	50
Table 2-2 Boundary Conditions	51
Table 2-3 Measured mobilities in capillary (using mesityl oxide).....	66
Table 2-4 Electroosmotic mobility measurements on a Pyrex chip.....	72
Table 2-5 Calibrate the bead velocity under certain applied voltages	75
Table 2-6 Bead velocity in the side channel due to main stream flow.....	77
Table 2-7 pH shifts due to electrolysis in waste reservoir.....	100
Table 4-1 Channel length and width of the device used	162
Table 4-2 Relation between applied voltage and mixing ratio.	165
Table 4-3 Applied voltage and resulting IgG introduced to reaction.....	182
Table 4-4 Reacted IgG concentration with dilution consideration.	184

List of Figures

Figure 1-1	Schematic diagram of a capillary electrophoresis system.....	6
Figure 1-2	(a) The formation of double-layer at a silica-solution interface and the generation of electroosmosis under an electric field. (b) The nearly flat electroosmotic flow profile. Both cations and anions experience electroosmotic flow at the same time. (c) A generic electrophoregram.....	7
Figure 1-3	Schematic drawing of double layer model.....	12
Figure 1-4	Schematic diagram of electroosmotic flow of electrolyte through a fused silica capillary.. ..	14
Figure 1-5	Schematic representation of the electrophoretic and electroosmotic components of cation, neutral, and anion in an electric field.....	15
Figure 1-6	The sequence of one mask microfabrication process.....	26
Figure 1-7	Schematic diagram of antibody.....	33
Figure 2-1	Coordinates and boundary conditions used for calculations.....	52
Figure 2-2	Pressure profiles along the centerline of the channel for different main channel length	54
Figure 2-3	The sequence of photolithographic fabrication.....	56
Figure 2-4	Channel dimensions and layout of the devices.	59
Figure 2-5	Block diagram of the high voltage relay controlled system, with computer control and digital data acquisition of laser excited fluorescence.	61
Figure 2-6	Electroosmotic mobility of buffer at different pH values.	67
Figure 2-7	Migration time varied with the voltage applied to the main channel. --with ionic strength control.....	70
Figure 2-8	Measured overall mobility at different pH --without ionic strength control.....	71
Figure 2-9	Calibration curve for bead velocity with the applied voltage.....	76
Figure 2-10	Bead leakage velocity from the side channel due to the potential applied to the main channel.	78
Figure 2-11	Calibration curve showing fluorescent intensity vs. dye velocity.....	80
Figure 2-12	Calculated leakage ratio of solvent velocity in the side channel to velocity in the main channel	83
Figure 2-13	Leakage dye velocity from the side channel as a function of the solvent velocity in the main channel. Three sets of data showing the dye leakage in the side channel is channel length dependent.	85

Figure 2-14	Schematic diagram showing the relationship of junction voltage and resistance to the relevant channels.	87
Figure 2-15	Flow velocity in the side channel as a function of the electric field. (Side channel located 10.0 mm from main channel entrance).....	92
Figure 2-16	Flow velocity in the side channel as a function of the applied electric field. (Side channels were located at the center of the main channel).....	95
Figure 2-17	Flow velocity in the side channel as a function of the applied electric field there. (Side channels were at 38.0 mm from the main channel entrance). 97	
Figure 2-18	Flow velocity in the side channel as a function of the applied electric field there. (Side channel length: 10.0 mm.)	103
Figure 2-19	Flow velocity in the side channel as a function of the applied electric field there. (Side channel length: 20.0 mm.)	105
Figure 2-20	Flow velocity in the side channel as a function of the applied electric field there. (Side channel length: 40.0 mm.)	107
Figure 3-1	Calculated linear dimensionless velocities entering the channels from main (U_{in}) and side (V), while exiting main channel outlet (U_{out}).	118
Figure 3-2a	Measured dye velocity with the driving force in the main channel.....	124
Figure 3-3a	Measured dye velocity with the driving force in the main channel.....	126
Figure 3-4	Measured fluorescent intensity as a function of voltage applied to the main channel.	130
Figure 3-5	The ratio of measured flow velocity compared to the theoretical velocity in the side channel as a function of different buffer pH in the main channel.132	
Figure 3-6	Measured velocity ratio of dye in the side channel as the pH in the main channel drops below the value in the side channel..	135
Figure 3-7	Dye velocity ratio in the side channel as the pH in the main channel drops. Different side channel lengths as indicated. Same main channel electric field strength applied.....	138
Figure 3-8	Dye velocity ratio in the side channel as the pH in the main channel drops. Different side channel lengths as indicated. Same side channel electric field strength applied.....	139
Figure 3-9	Measured dye velocity, v , in the side channel as a function of applied potential on the main cahnnel. With same pH in the two channels	142
Figure 3-10	Measured dye velocity, v , in the side channel as a function of applied potential on the main cahnnel. With differing pH values in the two channels.....	143
Figure 4-1	Schematic layout of mixing channels showing two reagents coming from two reservoirs 1 and 2 to meet at the intersection and flow to a third reservoir 3.....	154

Figure 4-2	Channel layout of the device IACE.....	161
Figure 4-3	Detailed channel layout of mixing tester.....	163
Figure 4-4	Detailed channel layout of immunoreactor.	164
Figure 4-5	The linear response of intensity as a function of the relative voltage applied to the dye reservoir compared to the constant Ground voltage applied the buffer reservoir.....	169
Figure 4-6	The converted response of intensity vs. concentration of the dye.....	170
Figure 4-7	The series of electrophoregram showing the signal intensity decreasing with the buffer reservoir voltage increase.	172
Figure 4-8	The series of electrophoregram showing the signal intensity increasing with the dye reservoir voltage increase.	173
Figure 4-9	Calibration curve showing Peak Height vs. Dye Concentration.....	174
Figure 4-10	On-chip reaction of BSA* and IgG.....	176
Figure 4-11	Selected traces from on-board calibration series showing the intensity change as a function of anti-BSA delivered.....	177
Figure 4-12	Labeling scheme identifying the channel resistances and lengths (R and l) by subscripts associated with the channel segment between intersection J_b and each of the reservoirs.....	179
Figure 4-13	Labeling scheme identifying the channel resistances and lengths between intersection J_a and each of the reservoirs.	180
Figure 4-14	Calibration curve showing the complex fluorescence intensity increased with the increasing Antibody IgG amount. Meanwhile, the intensity from free BSA* decreased due to consumption.....	185
Figure 4-15	Calibration curve showing complex intensity increase and Free BSA* decrease with the increasing IgG concentration. Dilution effect from V_{jb} was considered.	186
Figure 4-16	Known concentration samples were well fitted to the calibration curve..	189
Figure 4-17	Known concentration samples on the calibration curve. Dilution from the junction V_{jb} was considered.....	190
Figure 4-18	Sample carryover test showing no interference from the previous more concentrated sample.	191

Chapter 1

Introduction

1.1 Introduction

Employing electrokinetic effects to provide pumping action, fluid flow control, and separation within a monolithic planar chip has created a powerful format for performing analytical measurements. It is a fast growing and convenient new technique to perform liquid phase analysis on microfabricated substrates. Among the variety of techniques that have been implemented on microchips, capillary electrophoresis (CE) (1,2,3), synchronized cyclic electrophoresis (4), free-flow electrophoresis (5), and capillary gel electrophoresis (6,7) have been demonstrated for the separation of ions, and open channel electrochromatography (OCEC) (8), micellar electrokinetic chromatography (MEKC) (9), and packed bed liquid chromatography (10) for the separation of neutral species. It is possible and convenient to achieve coupling of sample handling and reactions with separation techniques to provide complete chemical analysis, i.e., the Lab-on-a-Chip concept. Some simple monolithically integrated devices have appeared in the literature and include pre- and post-column (11,12) chemical reactions in conjunctions with electrophoretic separations.

The first published demonstrations of capillary electrophoresis on a chip appeared in 1992 (13,14). Harrison et al. (14) showed that small bore capillary channels

etched in planar glass substrates, which were referred to as “chips”, could be used to perform capillary electrophoresis. The first demonstration was a separation of fluorescein and calcein. The performance at that time was limited by instrumentation, but was rapidly improved to yield separations of amino acids with 100,000 to 160,000 theoretical plates in periods of 2 minutes (15) to as little as 14 seconds (2). By decreasing the channel length and sacrificing baseline resolution (16,1), separation of the same mixture could be achieved in 3 seconds (13). The resolution of chips for amino acid separations was shown to be similar to that seen in silica capillaries, with similar applied field strengths (15,2,16). Jacobson et al. (3) later showed that entire separations could be performed in a total of 150 ms for compounds with differing charges. Chips were shown to withstand voltages of at least 25 kV across 5 cm of channel length (15), and improved heat dissipation relative to fused silica capillaries allowed powers as high as 2.5 W/m without heating of the running buffers, compared to the 1 W/m value in uncooled silica capillaries (16). These results made it clear that high performance on-chip separations by CE were readily achieved using glass substrates.

The early work establishes that separation can be performed on-chip, and showed some evidence of mixing and reaction. However, no rational studies of mixing at fluid junctions within these devices had been performed at the beginning of this thesis project. If the field is to grow rapidly and successfully, researchers will need design criteria for electrokinetically controlled micro-fluidic devices. The effort in this thesis is directed towards understanding the factors that influence mixing and pumping within fluidic manifold on a chip.

As more features are integrated into a planar format, performance optimization becomes essential. This includes achieving better separation resolution, improving sample plug shape, and controlling flow behavior within the intersecting networks. It is our interest to study the leakage phenomenon at the intersection of channels, and its dependence on the intersecting channel geometry, as well as the mixing behavior and the velocity profile at the intersection when two streams meet each other. All these are very important for control of an integrated analytical device, and the knowledge from this study provides the basis for better design rules. The application of the mixing knowledge gained here also lays a firm foundation for automatic calibration on-chip.

Electrophoresis and electroosmosis were the dominant effects governing all of the observations. Devices were fabricated using micromachining methods, and the results obtained with the devices were compared to some theoretical predictions. Immunological reaction was performed on chip to achieve on-board mixing and calibration. The remainder of this chapter provides some of the background for these elements of the thesis project.

1.2 Capillary Electrophoresis

Capillary electrophoresis is a widely used modern analytical technique permitting rapid and efficient separations in a small sample volume (17, 18). Electrophoresis is a well known phenomenon since 1897 (19). Skoog (20) defined electrophoresis as the “migration of particles through a solution under the influence of an electric field”. Tiselius (21) introduced the technique of moving boundary electrophoresis in 1937. However, it was not until 1967 that Hjerten (18,22) demonstrated the use of narrow-bore tubes for zone electrophoresis. High efficiency electrophoresis separations were finally achieved by Jorgenson and Lukacs (23, 24). Their contributions are often credited for popularization of this method, which is also called capillary zone electrophoresis (CZE) or high performance capillary electrophoresis (HPCE) (25). Characterized by low sample consumption, high resolution and efficient separation, CE has occupied its own niche in scientific research, and has become more popular in industry as well, with the introduction of a variety of CE instruments have been commercially available in recent years (26).

Capillary electrophoresis very closely resembles elution chromatography. A uniform buffer fills the capillary, as well as the reservoirs in which both capillary ends are submerged. The sample, which is introduced to the capillary as a very narrow plug at one end, represents the only discontinuous element. The principle of separation in CE is based on the differences in the electrophoretic mobilities of the differently charged species present in the solution contained in the capillary when there is an

electric field applied. As shown in Figure 1-1, capillary electrophoresis is carried out in a capillary tube which is usually 25 to 75 μm inner diameter, up to a meter in length. Typically, a ~ 0.01 M buffer, pH between 4 and 10, is used for separation. Voltage, which is furnished by a high voltage power supply, is up to 30 kV, though the current is very small, typically a few microamps. On-column detection is often used to avoid loss of separation efficiency caused by detector dead volume. Capillary used for CE is mostly made of fused silica, which contains surface silanol groups. At a given pH, these silanol groups may become ionized (27). At high pH, the surface is negatively charged. There are counter ions in solution that form a double layer. This immobile layer acts as a pumping force to generate migration of fluid through the capillary, which is called electroosmotic flow. The generation of electroosmosis, which is occasionally called electroendosmosis (18,28), is schematically demonstrated in Figure 1-2 (29). In this electropherogram, we can see that cations migrate first, followed by neutral molecules, with anions last. This is because cations experience both electrophoretic and electroosmotic mobilities in the same forward direction in the applied electric field, while neutral analytes migrate only under the electroosmotic effect, and the anions are affected by electrophoretic and electroosmotic mobilities in the opposite directions. Electroosmosis has an indirect influence on the separation. Electroosmotic flow gives a plug shaped flow profile instead of a parabolic flow profile as in pressure-driven flow, so that the solvent flow profile does not contribute to band-broadening. However, as will be shown in Equation 1-13 below, the resolution can be degraded by electroosmotic flow.

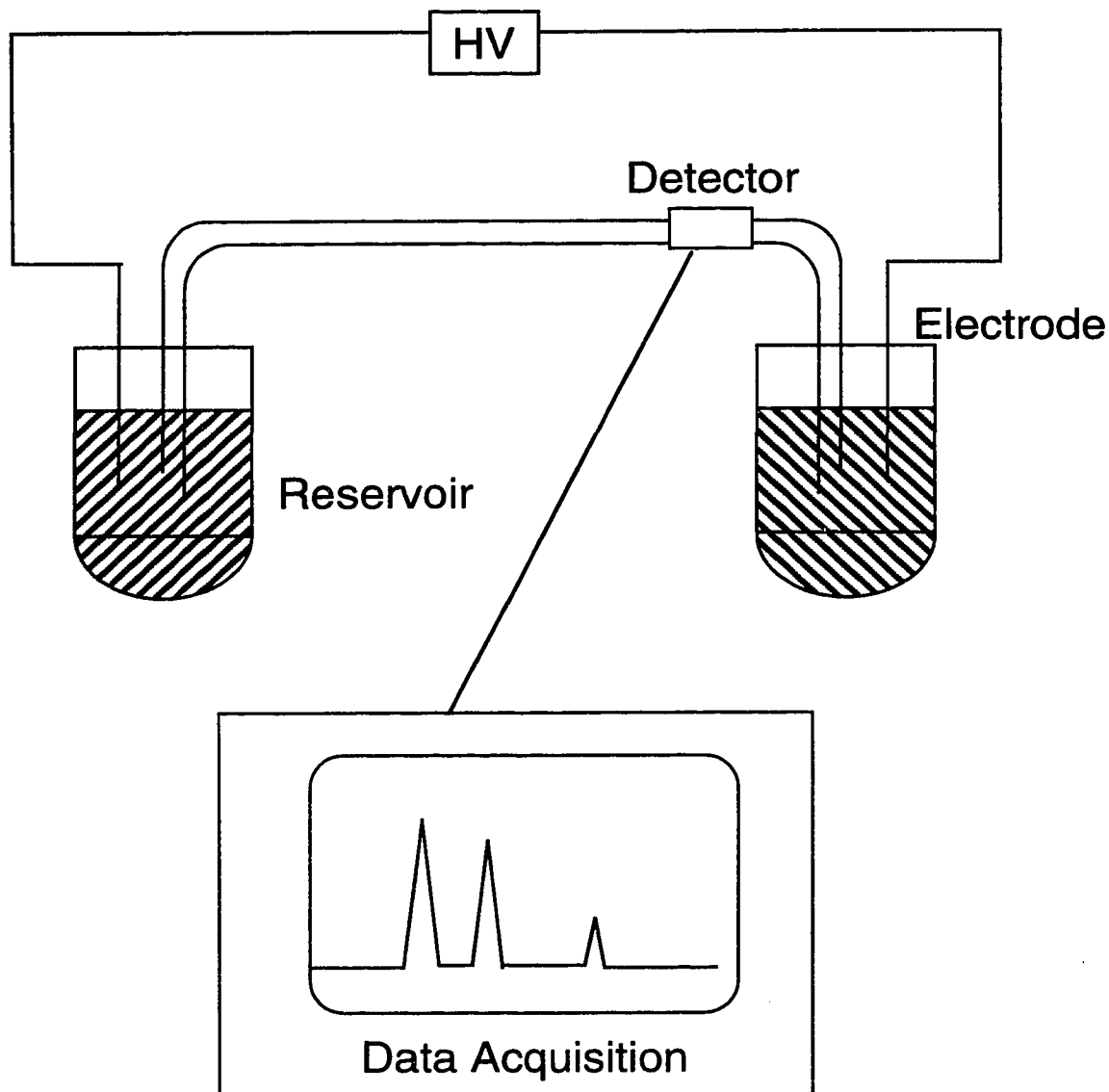


Figure 1-1 Schematic diagram of a capillary electrophoresis system.

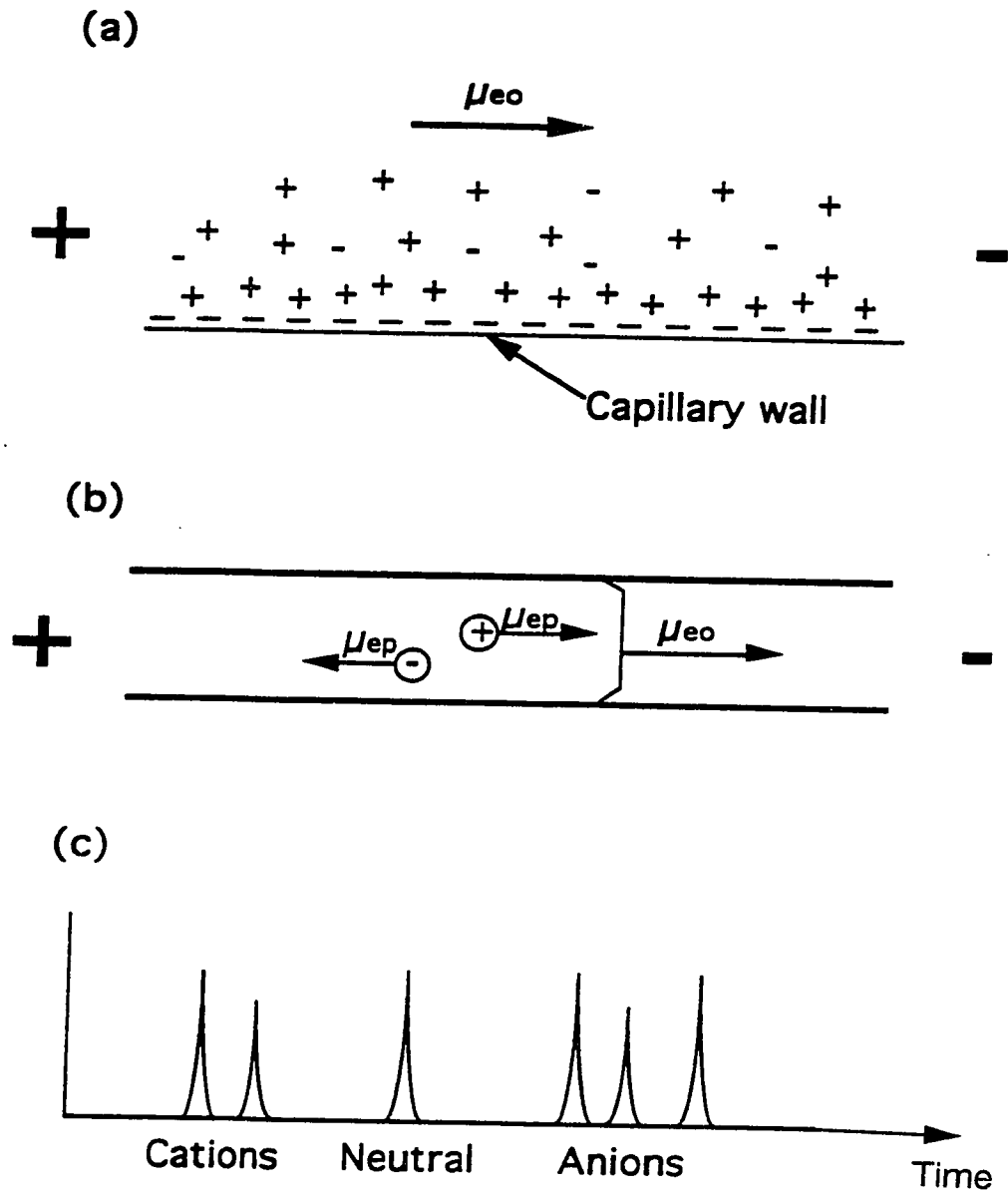


Figure 1-2 (a) The formation of double-layer at a silica-solution interface and the generation of electroosmosis under an electric field. (b) The nearly flat electroosmotic flow profile. Both cations and anions experience electroosmotic flow at the same time. (c) A generic electropherogram. (Adapted from reference 29)

1.2.1 Electrophoretic and electroosmotic mobilities

The basic theoretical concept of electrophoresis is relatively simply, and these concepts were reviewed by Hjerten (18). It involves the migration of charged species in an electrophoretic medium under the influence of an electric field. Cationic, neutral and anionic solutes are separated based on their difference in charge, size, and shape. When a charged particle is placed in an electric field, E , it experiences a force that is proportional to its effective charge, q , and electric field strength. The translational movement of the particle is opposed by a viscous drag force that is proportional to the particle velocity, v_{ep} , hydrodynamic radius, r , and medium viscosity, η . When the two forces are counterbalanced, the particle moves with a steady-state velocity, as shown in Equation 1-1 (This equation is true when $\kappa r \ll 1$, and κ is the reciprocal of the Debye length):

$$v_{ep} = \mu_{ep}E \quad 1-1$$

where μ_{ep} , electrophoretic mobility is described as Equation 1-2:

$$\mu_{ep} = \frac{q}{6\pi\eta r} \quad 1-2$$

Since the electrophoretic mobility is related to the zeta potential according to Huckle (18), it can be expressed as Equation 1-3 for small molecules, i.e. $\kappa r \ll 1$:

$$\mu_{ep} = \frac{\epsilon \zeta_{ep}}{6\pi\eta} \quad 1-3$$

where ζ_{ep} is the electrophoretic zeta potential and ϵ is the dielectric constant of solvent.

According to Henry (18), the Helmholtz von Smoluchowski Equation 1-4, which differs from Equation 1-3 by a constant factor of 2/3 is a more accurate representation of the electrophoretic mobility for the system having large particles, i.e. $\kappa r \gg 1$:

$$\mu_{ep} = \frac{\epsilon \zeta_{ep}}{4\pi\eta} \quad 1-4$$

Zeta potential is inversely proportional to the square root of ionic strength of the buffer, thus providing a relation between the electrophoretic mobility and buffer type and concentration.

The electroosmosis flow mobility expressions are identical to those developed for electrophoresis, since both phenomena are complementary. The electroosmotic velocity, v_{eo} , is given by Equation 1-5:

$$v_{eo} = \mu_{eo} E \quad 1-5$$

where μ_{eo} (electroosmotic mobility) is represented by an expression similar to Equation 1-4, for the case when $\kappa r \gg 1$, this is shown in Equation 1-6:

$$\mu_{eo} = \frac{\epsilon \zeta_{eo}}{4\pi\eta} \quad 1-6$$

where ζ_{eo} is electroosmotic zeta potential, and all other terms are as defined in the earlier equation. When electric field is applied to an analyte in its medium, both electrophoretic and electroosmotic forces simultaneously act on the ion. The ion's net mobility or observed mobility as it is sometimes called is the algebraic sum of Equation 1-1 and 1-5, which is shown as Equation 1-7:

$$v_{obs} = \mu_{obs}E = (\mu_{ep} + \mu_{eo})E \quad 1-7$$

With the net mobility, the ionic migration time (t_m) is given by Equation 1-8:

$$t_m = \frac{L}{(\mu_{ep} + \mu_{eo})E} = \frac{L^2}{(\mu_{ep} + \mu_{eo})V} \quad 1-8$$

where L is the column length, V is the voltage applied to the capillary (23, 24).

1.2.2 Electroosmosis and double layer theory

In most CE systems, electroosmosis, a type of bulk convective transport, plays a prominent role in species transport. Electroosmosis is usually present to some degree in all types of electrophoresis, but is particularly important in capillary electrophoresis because of the high surface-to-volume ratio of the capillary, the relatively low viscosity of most CE solvents, and the extremely high electric fields encountered in CE. Electroosmosis is one of a group of phenomena known as electrokinetic phenomena, in which either an electric potential or current brings about the movement of an electrolyte solution (as in electroosmosis) or the movement of an electrolyte solution brings a potential difference or current.

In order for electroosmotic flow to occur, there must be a space-charge region along the inner walls of the capillary column which can be acted upon by the applied electric field. In fused silica capillaries, which are mostly employed in CE work, this space-charge region develops in response to the ionization of silanol (Si-OH) groups to produce a negatively charged surface:



Additionally, a negatively charged surface may arise in very basic solutions due to the adsorption of hydroxide ions by the fused silica. Cations in solution will distribute themselves so as to counter this negatively charged surface, thus forming a net positive region of charge. Now, when a potential difference is imposed along the length of the capillary, anions will migrate toward the positive electrode (also known as the anode) and cations toward the negative electrode (also known as the cathode).

When the capillary wall is negatively charged, the region of solution immediately adjacent to the capillary wall will be rich in counter ions. According to Helmholtz (30), each charge on the wall would be exactly matched by an adjacent counterion in solution, thereby forming an electric double layer. Gouy and Chapman (31,32) later suggested that, due to the thermal motion of solvent molecules, the counterions would not necessarily be fixed along the charged wall. Instead, the counter charge would extend into the solution for some distance, thereby forming a diffuse layer. Stern (33) combined the models of Helmholtz and Gouy-Chapman, hypothesizing the some of the counter charge resides in the compact layer immediately adjacent to the wall, while the remainder resides in a neighboring diffuse zone. This model of the double layer theory is illustrated in Figure 1-3. Using the Stern Model, it is possible to determine how the potential ϕ and the charge density ρ vary as functions of the distance y from the capillary wall. This information, in turn, will allow an expression for electroosmotic flow velocity to be determined.

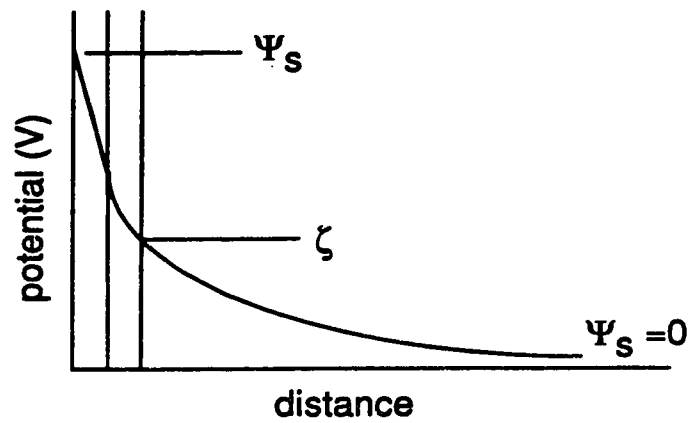
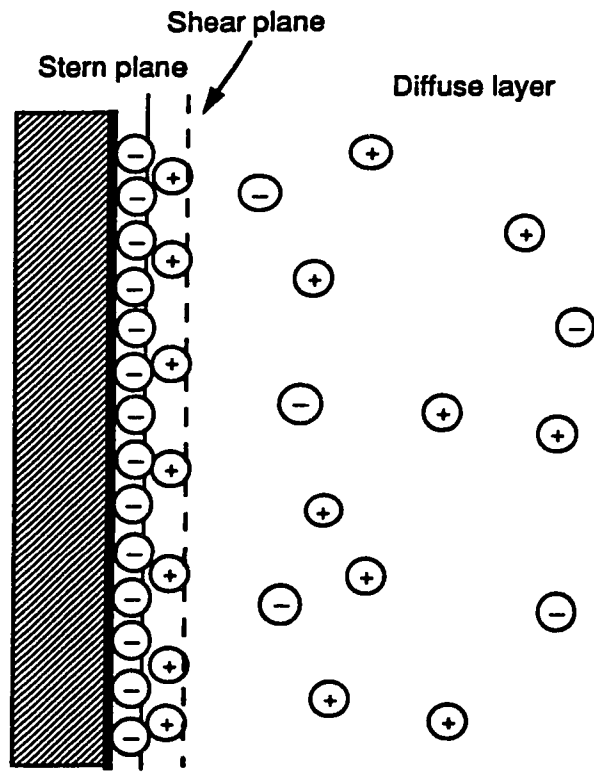


Figure 1-3 Schematic drawing of double layer model. Ψ_s is the electric potential at any distance from the wall, ζ represents the potential at the plane of shear.

When electric potential is applied to the capillary, the positively charged ions move toward the cathode, and the negatively charged ions move toward the anode. The capillary wall is negatively charged due to the ionization of the surface silanol group, and this immobile layer can not move towards the anode. However, the applied field exerts a force along the cathode direction on the excess positively charged ions near the surface. Therefore the positively charged ions drag the electrolyte solution along and there is a net flow of solvent towards the cathode. This is the origin of electroosmotic flow. Electroosmotic flow affects all species equally, as it acts to sweep the solution as a whole through the capillary column, as shown in Figure 1-4. Electroosmosis and electrophoresis may take place simultaneously, and so the two modes of ion transport may either agree with or oppose one another, depending on the direction of each. This is illustrated schematically in the Figure 1-5.

Silica-water systems are reported to have a zeta potential of approximately 25-150 mV, and the estimated double layer thickness (r_D) for a 1×10^{-2} M monovalent cation-anion salt in water was 3 nm (34). This double layer thickness can be estimated roughly for CE buffer, which is usually in diluted concentration in the analytical applications. A flat-fronted flow velocity profile is expected with electroosmosis if the capillary tube radius is greater than about seven times r_D (35,36). The flat-fronted flow profile is the most celebrated advantage to using electroosmotic flow in capillary electrophoresis. The resulting reduction in solute diffusion, in comparison with pressure-driven flow, greatly improves column efficiency.

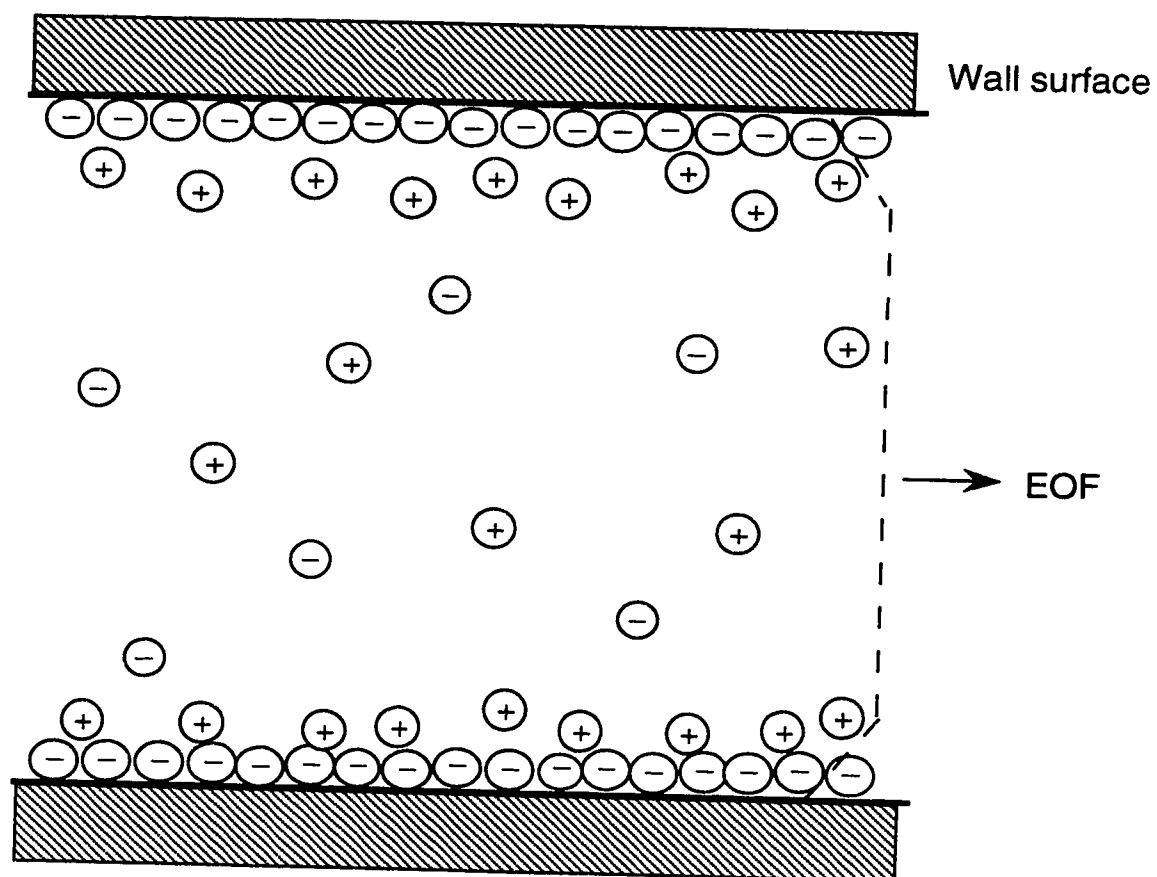


Figure 1-4 Schematic diagram of electroosmotic flow of electrolyte through a fused silica capillary. The dashed line shows the plug flow velocity profile.

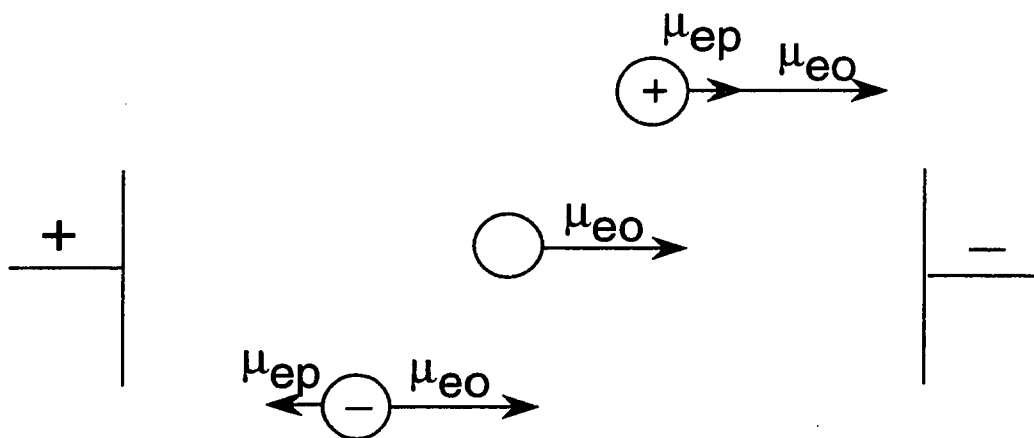


Figure 1-5 Schematic representation of the electrophoretic and electroosmotic components of cation, neutral, and anion in an electric field.

1.2.3 Electrolyte system and ζ potential dependence

The electrophoresis buffer is of key importance in capillary electrophoresis, because its composition fundamentally determines the migration behavior of the analytes. The overall stability of the system and satisfactory separation of the analytes can be achieved only with a suitable electrolyte system. A wide variety of electrolyte system have been used in CE to effect the required separation. The majority of these are aqueous buffers. There are several parameters to consider when selecting an appropriate separation buffer.

The net effect of ion migration from electroosmosis and electrophoresis can be expressed quantitatively with equations, but in practice, electroosmotic flow is often difficult to control and/or reproduce due to its dependence on many system-specific variables, such as the surface zeta potential and solution viscosity and permittivity. The well known formula of Von Smoluchowski relates electroosmotic mobility, μ_{eo} , with the properties of the liquid (permittivity ϵ and viscosity η) and ζ potential, which is the electrical potential at the radius of shear to its value in the distant bulk medium. This was given as Equation 1-6. Furthermore, ζ itself is dependent upon the surface charge density and the double-layer thickness, which, in turn, is dependent upon the magnitude of ionic charge and concentration, ionic strength, pH, viscosity, permittivity, capillary material, and capillary pretreatment. Each of these will be briefly considered below.

1.2.3.1 Buffer pH

Buffer plays an important role in the quality of a separation. Buffers provide a constant conductive medium in CE, so that the charged analyte molecules can migrate freely in the electric field without the restriction of carrying the majority of the current. The electroosmotic mobility depends on solution pH (27,37-41). As the hydrogen ion concentration is increased, the number of negative sites on the capillary wall decreases due to neutralization and so the surface charge density decreases. This will result in a decrease in the electroosmotic velocity. There is often a sigmoidal dependence of electroosmotic mobility on pH resembling a titration curve. The inflection point of such a curve corresponds to the pK_a of the capillary wall groups which are responsible for the surface charge (42). More important, the buffer also provides selectivity in the electrophoretic process by allowing the manipulation of sample analyte mobility. The reproducibility of a series of analyses is dependent on the buffering strength of the buffer at a given pH value, whereas efficiency and resolution is dependent on the separation current and the resulting Joule heating inside the capillary.

Once we have information about our sample to be analyzed, we usually choose a buffer whose separation pH approximates the pK of the solute mixture. With crude biological mixtures, the average pK is typically close to neutral. Increasing the separation buffer pH will result in an increase in the EOF, which will result in a increase in the flow velocity, as predicted in Equation 1-5 and Equation 1-6. Consequently, as shown later in the presentation of Equation 1-10 on page 23, the separation efficiency will also be affected by the buffer pH.

1.2.3.2 Ionic strength

Ionic strength or concentration of the buffer has significant effects on solute mobilities and separation efficiency (43). The dependence of mobility on buffer concentration has been known to CE workers for years with the contributions from several groups (44-48). The electroosmotic mobility is inversely proportional to the ionic strength, which is dependent upon buffer type and concentration of an electrolyte solution (49-51). In general, increasing the ionic strength of a solution leads to a decrease in the double-layer thickness, which, in turn, decreases ζ and then the electroosmotic mobility (37,52). The two major advantages of increasing ionic strength are the improvement in buffer capacity and the effect on decreasing analyte-wall interactions (53). The net effect on the separation, therefore, will be to increase resolution, provided that capillary thermostating capability is not overcome and that unwanted analyte dissociative processes (eg. equilibria of peptide/protein dimers) do not occur. On the other hand, an increase in ionic strength might improve resolution in mixtures by decreasing nonspecific analyte-analyte interactions (54).

High ionic strength buffers have been used to enhance efficiencies in protein separations. Green and Jorgenson (55) devised a method to minimize the adsorption of proteins on fused silica capillaries in CE by using K^+ concentrations of 0.3 M and above in the operating buffer. The increased ionic strength resulted in a competition between K^+ and proteins for cation-exchange sites on the silica surface. However, a drawback of this method is due to the increase in ionic strength and the subsequent increase in conductivity and Joule heating. It would be necessary to use lower voltages and

capillaries of small diameter to allow adequate heat dispersion. This leads to lower efficiencies or to poor detection limits, respectively.

1.2.3.3 Organic additives and surfactants

Addition of organic solvents to the electrophoretic buffer permits the analysis of some analytes which are not normally soluble in H₂O by improving their solubility in the buffer (42,56,57,58). Organic solvents are also known to reduce the electroosmotic flow, which may result in better resolution at the expense of a longer analysis time. The addition of organic modifiers to the separation buffer will have differing effects, depending on the nature of the additives. Similarly, surfactants can be used in conventional CE to adjust electroosmotic flow, and could be used for chip applications for the same purpose (59). When surfactants are present in solution at sub-micellar concentration, they will generate hydrophobic interactions to influence separation resolution and selectivity (60). Differently charged surfactants can be used to control the electroosmotic flow in CE.

Anionic surfactants, such as SDS (60,61,74,76), can be added to electrolyte system to interact with the capillary wall so as to eliminate the analyte-wall adsorption; meanwhile it provides a source of negatively charged surface, which will enhance the electroosmotic flow. Cationic surfactants serve the same purpose as to eliminate the analyte-wall interaction, but decrease the electroosmotic flow mobility. Other than these, polyoxyethylene surfactants, such as Tween series (Tween 20, Tween 40, Tween

80) and Brij 35, are used to create a hydrophilic surface on the capillary wall, which allows protein separation (61,74,76).

1.2.3.4 Effect of applied voltage on mobility

The effect of applied voltage on solute mobility and separation parameters in CZE was thoroughly investigated by several groups (27,62-66). According to Equation 1-1, the solute velocity is linearly proportional to the applied voltage. In practice, however, the solute velocity is not a linear function of voltage (62). It has been argued that, as voltage is increased, the heat generated results in an increase in temperature and the formation of a radial temperature gradient, with the temperature near the wall (where the heat is dissipated to the surroundings) being lower than that at the center. Higher temperature results in increased buffer conductivity, solute diffusion coefficient and double layer thickness, and decreased buffer density and viscosity (67). The net effect of these changes is an increase in solute mobility and a decrease in column efficiency.

Results from Issaq et al. (68) demonstrate that the effect of applied voltage on electrophoretic and electroosmotic mobility is quantitatively similar. In both cases, the mobility increases with increasing applied voltage, in agreement with Altria and Simpson's findings (45). At low buffer concentration (25 mM), the mobility increases linearly with increasing applied voltage. Since the mobility is not a constant, even under conditions for which joule heating may not be a disruptive factor, plots of migration velocity versus voltage are not expected to be linear, in contrast to what was originally believed (23).

The observable effect of increasing mobility with increasing voltage is mainly attributed to temperature increases inside the column, as a result of Joule heating. Specifically, this is a direct consequence of the larger temperature coefficient of viscosity ($2\%/^{\circ}\text{C}$). There are other factors besides temperature that, if operative, may increase solute mobility with increasing applied voltage (61). However, these factors are significant only at extreme cases, which are not normally used in CZE.

1.2.3.5 Column material and treatment

Finally, the column material and/or treatment have a pronounced effect on electroosmotic flow. CE systems mostly use fused silica capillaries, which typically have negatively charged walls as described previously. Synthetic organic polymer capillaries, such as polyfluorocarbon, polyethylene, and polyvinylchloride, also exhibit negative zeta potentials, presumably due to the ionization of carboxylic acid groups present on the walls as a result of the synthesis process (69) or hydrophobic sorption forces (70). However, the electroosmotic flow in polymer capillaries is often significantly less than that in silica capillaries, indicating that the surface charge density is less. Regardless of the capillary material itself, capillary age, treatments and conditioning procedures can have a significant effect on electroosmotic flow (39,71). Capillaries tend to demonstrate a sort of “memory effect” or hysteresis after being exposed to harsh conditions, such as strong acidic or basic media, which results in the alteration of the electroosmotic flow rate even after the conditions have been returned to “normal”(38). The effects of capillary treatment on electroosmotic flow are attributed

to the relatively slow equilibration of the surface charge at the wall-solution interface. Also the variations of the electroosmotic mobility were affected by the ion exchange properties of the silica wall (72), and the influence of the radial electric field (73), which keeps embedding cations into the silica wall (physically driving them to penetrate the wall) to such an extent as to continuously alter the EOF.

In spite of the irreproducibility of electroosmotic flow, this bulk solution transport mechanism is essential to effect certain separations in CE. Electroosmosis allows for the simultaneous determination of cations, anions and neutrals (74), is responsible for the mobilization of concentration boundaries (75) and is an integral part of micellar electrokinetic techniques (76). In addition, electroosmosis can be used as a solvent pump or sample injection mechanism (77-80).

1.2.4 Separation Efficiency and Resolution

High separation efficiency can be achieved when using capillary electrophoresis. This results in part from the unique plug-shaped flow profile under the effect of the electrokinetic flow (28). Peaks are usually Gaussian shaped. The major sources of band broadening are due to mass diffusion, injection and detection volume, detection time constant, and residual interaction of the analyte with the capillary walls, and thermal gradients induced by Joule heating.

The peak variance due to mass diffusion is given by Equation 1-9:

$$\sigma = \sqrt{2Dt_m} = \sqrt{\frac{2DL^2}{\mu_{obs}V}} \quad 1-9$$

where V is the voltage drop between the injector and the detector, and the number of theoretic plates can be expressed as Equation 1-10 (23, 24):

$$N = \frac{(\mu_{ep} + \mu_{eo})V}{2D} \quad 1-10$$

N and D are the theoretical plate number and the diffusion coefficient. This equation is accurate only when longitudinal diffusion is the major source of band broadening and other sources are negligible.

The resolution, R , measures the separation of two peaks, which can be expressed as Equation 1-11 (20):

$$R = \frac{t_2 - t_1}{\frac{1}{2}(W_1 + W_2)} \quad 1-11$$

where W_1 and W_2 are baseline bandwidth of peaks. According to Giddings (28), resolution is related to the number of theoretic plates as shown in Equation 1-12:

$$R = \frac{\sqrt{N}}{4} \times \frac{\Delta v}{v} \quad 1-12$$

where Δv is the difference in component flow velocity and v is the average velocity.

Resolution can be represented with mobilities as in Equation 1-13 (23,24):

$$R = \frac{\sqrt{N}}{4} \times \frac{(\mu_2 - \mu_1)}{\mu} \quad 1-13$$

where μ_1 and μ_2 are the overall mobilities of the two components and μ is the average mobility. Because μ includes the contribution of μ_{eo} , increasing electroosmotic flow rates tends to decrease resolution.

1.3 Micromachining

Micromachining is a rapidly growing technique for the fabrication of three dimensional micromechanical structures and related devices in the silicon or other materials using electronics fabrication technology (81). Several major processes involved in the micromachining are film deposition, photolithography, etching, diffusion or ion implantation, and bonding. All of these processes have been commonly used in integrated circuit manufacture (82, 83).

As stated by Z.H. Fan (84), a standard one mask fabrication process starts with the deposition of a layer of silicon dioxide on a silicon or glass wafer using thermal oxidation, as Figure 1-6 a. Other film deposition techniques used are spin coating, physical vapor deposition (PVD), chemical vapor deposition (CVD), low pressure CVD, plasma enhanced CVD, and sputtering (83). SiO_2 or Si_3N_4 is mostly used as a mask when Si is the substrate to be etched. A photoresist (PR), which is light sensitive, is usually spin coated on the surface (Figure 1-6 a). Residue solvent in the photoresist is removed by so-called soft-baking at certain temperatures. Photolithographic patterning is then performed as shown in Figure 1-6 b. The desired pattern is made in the master mask and ultraviolet (UV) light is usually used as the radiation source. The exposed area of photoresist undergoes photochemical reactions, which change the physical and/or chemical property of the film.

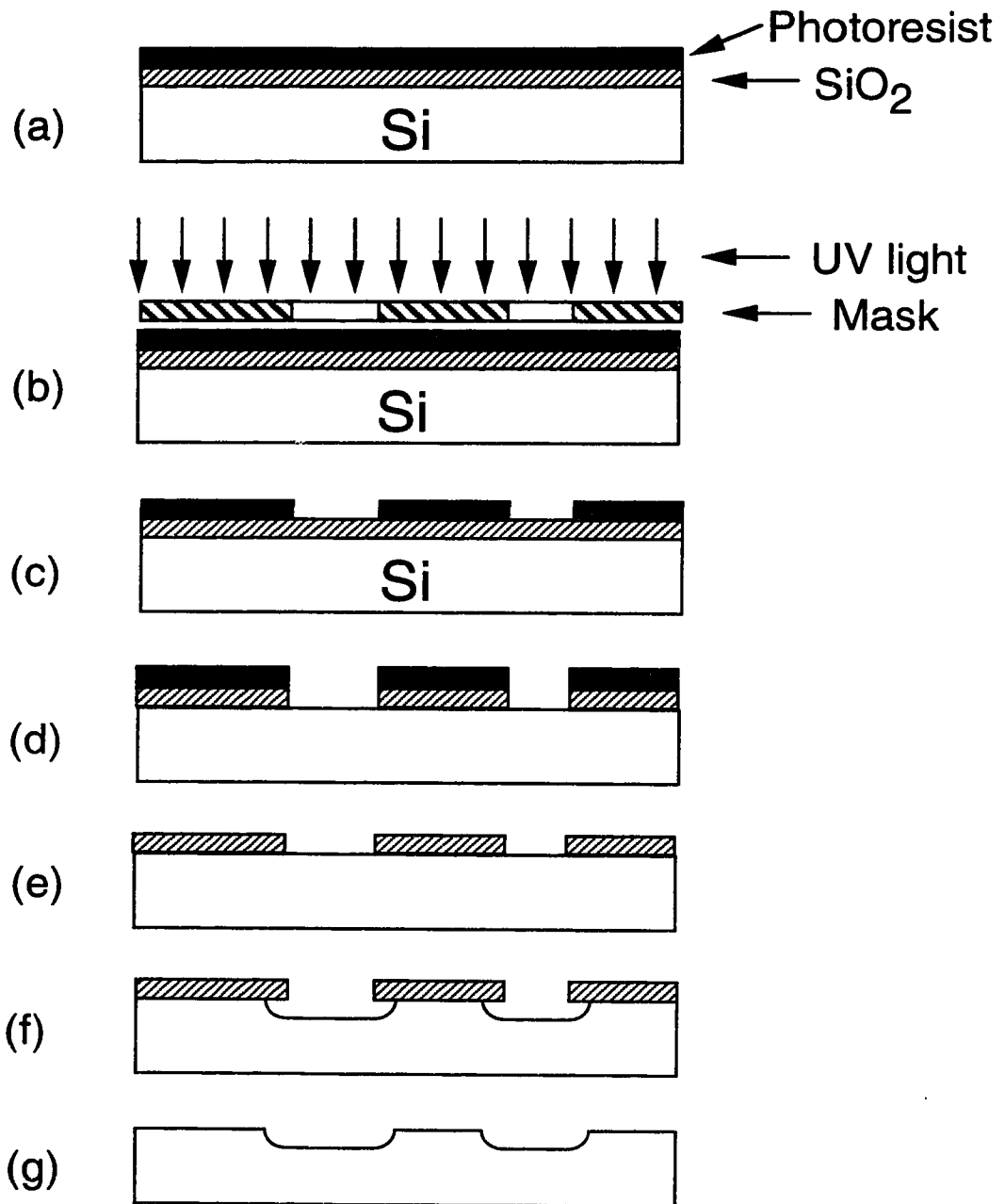
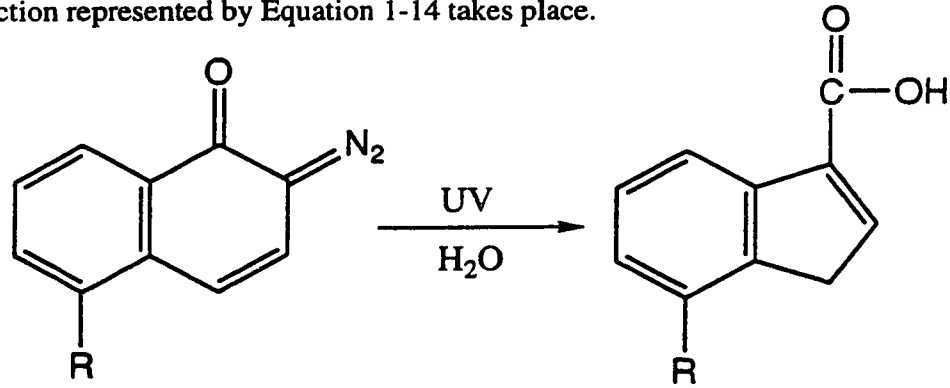


Figure 1-6 The sequence of one mask microfabrication process. (See text for discussion)

Photoresist (PR) consists of a photosensitizer molecule, i.e., diazonaphthoquinone or its substitute, and a polymer, both of which are dissolved in an organic solvent. The polymer acts as a matrix to form a film. Upon radiation exposure, the reaction represented by Equation 1-14 takes place.



The R group in diazonaphthoquinone varies with the product and the manufacturer. The carboxylic acid produced accelerates the film dissolution (development) by the basic developer, and the exposed area is stripped off as shown in Figure 1-6 c.

After development, hard-baking at a high temperature is often carried out to improve polymer-wafer adhesion. The next step is to etch the exposed silicon oxide layer (Figure 1-6 d), followed by removing the rest of the photoresist (Figure 1-6 e). Si substrate is then etched while the remaining SiO₂ functions as a mask layer (Figure 1-6 f). Different channel shapes can be obtained by choosing anisotropic etching, which depends on etchants (85). After the SiO₂ layer is removed, the desired pattern appears in the Si wafer (Figure 1-6 g). To complete the fabrication of a device, bonding and packaging procedures are needed, although they are not shown in the figure.

Using micromachining technology, many micromechanical structures have been fabricated and reported in the literature. For example, micromachined pumps and

valves have been designed, and even integrated into chemical sensors to handle liquid or gas flow (86, 87). Other examples include micromachined motors, rotators, mass flow meters, neural probes, atomic force microscopes, etc. (81, 85, 88). Many of the applications are not related to chemistry.

The strength in the micromachining technology lies in the ability to make miniaturized 3-dimensional structures integrated together or with electronics in large batch processes. Mass production can result in excellent reproducibility, and potential inexpensive devices.

The devices used in this thesis project were all made from glass, which material brings the promise to have further low cost devices that can be disposable. The micromachining procedures are slightly different, which will be described in detail in Chapter 2.

1.4 Mathematical Formulation

In most of the microchip based capillary electrophoresis studies, the injection and separation of the sample into the micro channels were achieved using the electroosmotic flow driven by an applied potential along the injection or separation channel. The electroosmotic flow inside the channel is influenced by various parameters. We only have some experimental studies with the electroosmotic flow behavior, however, it would be more desirable to perform such investigations through both experiment and numerical simulations.

It was Rice and Whitehead (89) that started formulating the equations for the electroosmotic flow in a capillary in the 60's. In the early 80's, Jorgenson and Lukacs (90) developed a one-dimensional model for the capillary electrophoresis. It was not until the 90's, that Andreev and Lisin (91) presented a mathematical model for capillary electrophoresis and studied the influence of the electroosmotic flow profile on the efficiency of separation. For a better control of the flow behavior in the microfluidic device, we required a specific and detailed numerical model for thorough understanding of fluid mechanics within electroosmotically pumped fluid networks.

A numerical study developed by Hu and Masliyah (92), in the department of Chemical Engineering, University of Alberta, has successfully demonstrated the prediction of steady state electroosmotic flow in the three channels under different conditions, with the potential at one of the reservoirs either fixed or left uncontrolled while an electric potential is applied across the remaining two reservoirs. With the

proper assumptions, the study showed that the electroosmotic flow in a capillary channel can be mathematically solved by using the Poisson-Boltzmann equation, mass conservation and the Navier-Stokes transport equations coupled with the Nernst-Planck equation. Some of the details of this model are highly relevant to this thesis, which provided experimental data for the model, as well as verification tests. Some of the detailed fundamentals of this model are presented in Chapter 2.

1.5 Immunoassay

Immunoassay refers to a group of assay methods using immunological recognition reactions which are quantitative, specific, and sensitive (93,94,95). The presence of “humoral factors” in blood capable of neutralizing and presumably combining with toxins or microorganisms, forms the basis of these attractive methods. Whether cells or antibodies are the attackers, the target of the host’s attack is always the “antigen”. This exclusive nature of these “anti-bodies” in protecting the host benefits immunologists as well other scientists who use the techniques as tools. Early studies on antibody-antigen interactions using radiolabelled proteins (96) helped to lay the groundwork for the first such method able to perform the assay. The development of competitive binding assays using radiolabelled ligands as described by Berson and Yalow in 1958 stimulated the applications of this new technique, particularly in the fields of biomedical research and clinical chemistry.

The excellent performance characteristics of radioimmunoassay, most notably its sensitivity (down to 10^{-17} mol) and specificity, have resulted in its becoming a primary analytical tool not just in the clinical field, where it receives its most frequent use, but in many other basic and applied scientific fields as well. Nevertheless, the use of radionuclides as immunochemical labels does have certain inherent drawbacks, such as the relatively short shelf-life of the reagents and the potential health hazards. Partly in response to the challenge posed by these drawbacks, a wide variety of nonisotopic immunoassay techniques has arisen. One of the two most successful techniques that

have been shown to compete favorably with radioimmunoassay in many areas of performance is fluorescence immunoassay. To serve a better understanding of immunoassay technology, we give the following terminologies here.

1.5.1 Antibody

In present day terminology, an antibody is a member of the family of mildly glycosylated proteins called immunoglobulins, which can specifically combine with an antigen. The region of an antigen which binds to an antibody is termed an epitope. There are two types of antibodies used in immunoassays - monoclonal and polyclonal antibodies. Monoclonal antibodies are specific for a single epitope. Polyclonal antibodies have the ability to bind to several epitopes on a single antigen. Antibodies are so highly specific that slight modification in the epitope structure may prevent recognition. Immunoglobulins are a diverse group of proteins sharing a number of important and diagnostic structural features. As elegantly reviewed elsewhere (97, 98), each immunoglobulin is composed of equal molar concentrations of heavy (50,000 to 75,000 mol wt) and light (22,500 mol wt) polypeptide chains. The N-terminal 110 amino acid sequence of each is referred to as the variable region. The term variable was coined because sequence analyses of this region in different proteins revealed an extremely low probability of finding two alike. Within the intact molecule, variable region sequences of both heavy and light chains are structurally associated with each other and form the antibody combining site (that region of the molecule which binds to the antigen and is responsible to the antibody specificity). Immunoglobulin G (IgG)

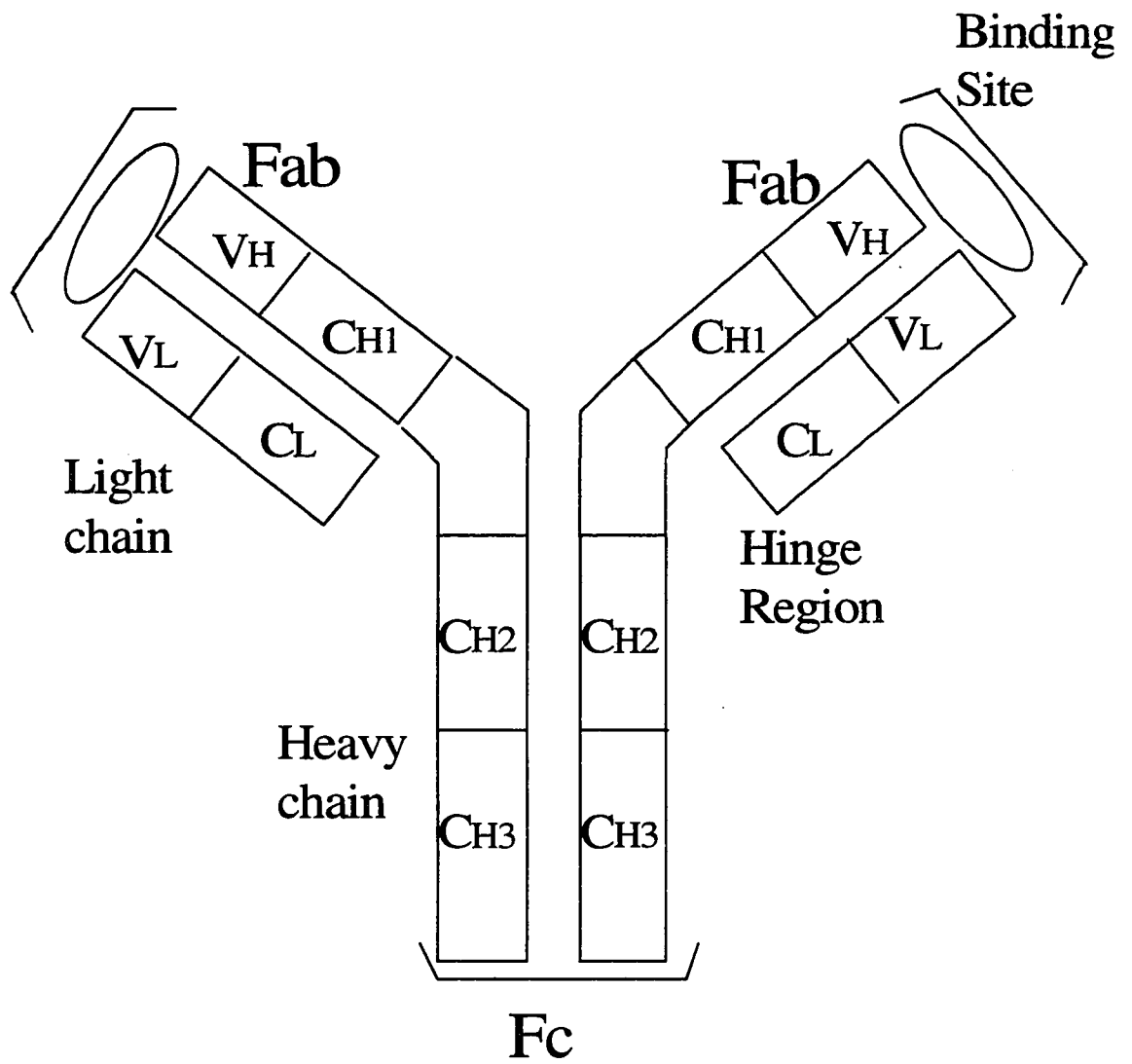
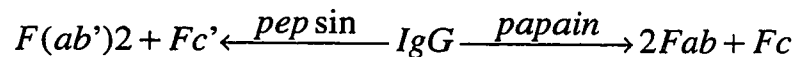


Figure 1-7 Schematic diagram of antibody.

occur as monomers and possess a pair of identical heavy and light chains which provide two identical combining sites. Polymeric antibodies have multiples of this bivalency. The remaining region of both heavy and light chains constitute the constant region sequence, and contain antigenic markers which determine the isotype (i.e. class, subclass, or light chain type) of an immunoglobulin or antibody. In humans and many animals, two light chain isotypes, kappa and lambda, and five heavy chain class isotypes, IgG, IgM, IgA, IgD, and IgE, have been identified.

IgG molecules contain only one structural Y unit and consist of three protein domains. The protein domains are comprised of two identical Fab domains and one F_c domain as illustrated in Figure 1-7. The heavy and light chains in the Fab domain and the two heavy chains in the F_c domain are cross-linked by di-sulphide bonds. Each Fab domain contain an antigen binding site. The F_c domain is responsible for immune response. The two Fab and the F_c domains may be cleaved using pepsin or papain to produce independent Fab and F_c fractions. Using pepsin, cleavage occurs along the F_c domain between the two di-sulphide bonds to produce an F_c fragment where the two heavy chains are connected by one di-sulphide bond and a Fab fraction where the two arms of the Y are linked by one di-sulphide bond. In this case, the Fab fragment is referred to as $F(ab')_2$. Using papain, cleavage occurs such that the two di-sulphide bonds in the F_c domain remain with the F_c fragment. This cleavage results in two separate Fab fragments. The following equation represents the two types of cleavage of antibodies.



The IgG antibody molecule has a molecular weight of about 150,000 Daltons. With papain cleavage, the two Fab fragments and the F_c fragment are approximately 50,000 Daltons each. In the case of pepsin cleavage, the F(ab')₂ fragment is 102,000 Daltons and the F_c portion is about 48,000 Daltons.

1.5.2 Antigen

The term antigen has a more complex terminology than does antibody. Simplistically, an antigen is merely the substance to which the antibody binds. As initially shown by Landsteiner, antibodies can bind and have specificity for relatively small chemical groupings (99). It has been estimated that this chemical group may be as large as a pentasaccharide (100) or a tetrapeptide (101). An antigen can be an entire protein molecule, a microorganism, or a mammalian cell. Hence, the actual site of antibody attachment is best referred to as an antigenic determinant or an epitope. Antigens therefore may be multivalent, such as proteins and bacteria, or may be univalent such as haptens or very small hormones.

1.6 Scope of Thesis

As a rapidly growing technique, microfabrication is widely used in multidisciplinary applications. Given the potential demand of these new, microfabricated analytical devices, there is a strong need to have a better understanding of the design rules. Flow behavior in micro-fluidic device attracts the interest of researchers, as does the mixing process where two streams meet. Leakage studies provide us the knowledge of how the side channel geometry will affect leakage flow, which can then form the basis of our future design rules. Better and more effective control can be achieved with the understanding of the fact that mixing of two streams with different electroosmotic mobilities gives complicated velocity profiles.

Automation is an important issue within the commercialization possibilities of microfluidic devices. It is hoped these devices will be used by people with multidisciplinary backgrounds, or with minimum training. With the powerful control of fluid flow that is possible, on-board calibration should be achievable, as meeting the promise of approaching fully automated on-chip analysis. Demonstration of this goal is another key part of this thesis.

In Chapter 1, we give the relevant background to this thesis work, which includes the concept of capillary electrophoresis and some basic equations, the technique to make microfabricated devices, and the introduction of the need of mathematical formulation.

In Chapter 2, leakage phenomena are investigated and discussed. With the brief introduction to the model of electrokinetically driven manifolds developed in the

Masters Thesis of L. Hu in Department of Chemical Engineering, University of Alberta, we present the comparable experimental results of the leakage study. The extent of leakage with a “T” intersection network will be presented. The effect of varying side channel length or side channel position on the main channel is examined. From this chapter, we understand that the side channel geometry plays an important role in the leakage phenomenon. This provides us better knowledge for developing design rules.

Building a calibration curve for velocity measurements is also an important issue in Chapter 2. The calibration curve relates the signal intensity with the dye flow velocity, which functions as a powerful tool to measure the leakage flow velocity. Junction voltage calculation methods are introduced so that we can calculate the effective electric field and distinguish the electrically driven dye flow from the leakage flow.

In Chapter 3, we present the results from the study of variable electroosmotic flow rate and the consequent effect on mixing behavior in the T-shaped intersecting channels. When electroosmotic mobilities are not identical in the mixing channels, the mixing will become complicated, and the resulting flow velocity profiles are unpredictable when only the electrokinetically driving force is considered. Different electroosmotic mobilities are introduced to the system using buffers with a different pH in each channel. The complex behavior seen is described, and linked to the flow model where possible.

In Chapter 4, we present the on-board calibration of an immunological reaction. With the understanding of the flow behavior and the mixing problem outlined in

Chapter 2 and Chapter 3, we have better design and control in our miniaturized “Lab-on-a-chip” device. Using a complicated immunological reactor, we achieved the on-board dilution of the antibody to be reacted with our antigen. This work is very important in achieving the final goal of full automation on-chip. A calibration curve from the on-board dilution is presented, and its performance as a calibration tool is evaluated.

Chapter 5 gives the summary of the previous individual chapters. The future outlook is briefly discussed.

References

- 1 Harrison, D.J.; Fluri, K.; Seiler, K.; Fan, Z.; Effenhauser, C.S.; Manz, A., *Science*, **261**, 895-897, **1993**
- 2 Effenhauser, C.S.; Manz, A.; Widmer, H.M., *Anal. Chem.*, **65**, 2637-2642, **1993**
- 3 Jacobson, S.C.; Hergenroder, R.; Koutny, L.B.; Ramsey, J.M., *Anal. Chem.*, **66**, 1114-1118, **1994**
- 4 Burggraf, N.; Manz, A.; Effenhauser, C.S.; Verpoorte, E.; de Rooij, N.F.; Widmer, H.M., *J. High Res. Chromatogr.* **16**, 594, **1993**
- 5 Raymond, D.E.; Manz, A.; Widmer, H.M., *Anal. Chem.* **66**, 2858, **1994**
- 6 Effenhauser, C.S.; Paulus, A.; Manz, A.; Widmer, H.M., *Anal. Chem.*, **66**, 2949, **1994**
- 7 Wooley, A.T.; Mathies, R.A., *Proc. Natl. Acad. Sci. USA*, **91**, 11348, **1994**
- 8 Jacobson, S.C.; Hergenroder, R.; Koutny, L.B.; Ramsey, J.M., *Anal. Chem.*, **66**, 2369, **1994**
- 9 Moore, A.W.; Jacobson, S.C.; Ramsey, J.M., *Anal. Chem.*, **67**, 4184, **1995**
- 10 Ocvirk, G.; Verpoorte, E.; Manz, A.; Grasserbauer, M.; Widmer, H.M., *Anal. Methods Instrum.* **2**, 74, **1995**
- 11 Jacobson, S.C.; Ramsey, J.M., *Anal. Chem.*, **68**, 720, **1996**
- 12 Fluri, K.; Fitzpatrick, G.; Chiem, N.; Harrison, D.J., *Anal. Chem.*, **68**, 4285, **1996**
- 13 Manz, A.; Harrison, D.J.; Verpoorte, E.M.J.; Fettingner, J.C.; Paulus, A.; Ludi, H.; Widmer, H.M., *J. Chromatogr.* **593**, 253-258, **1992**
- 14 Harrison, D.J.; Manz, A.; Fan, Z.; Ludi, H.; Widmer, J.M., *Anal. Chem.* **64**, 1926-1932, **1992**
- 15 Seiler, K.; Harrison, D.J.; Manz, A., *Anal. Chem.*, **65**, 1481-1488, **1993**
- 16 Fan, Z.H.; Harrison, D.J., *Anal. Chem.*, **66**, 177-184, **1994**
- 17 Tiselius, A., *Trans. Faraday Soc.*, **33**, 524-531., **1937**
- 18 Hjerten, S., *Chromatogr. Rev.*, **9**, 122-224, **1967**
- 19 Kohlrausch, F., *Ann. Phys (Leipzig)*, **62**, 209, **1897**

-
- 20 Skoog, D.A., *Principles of instrumental Analysis (3rd Ed.)*, Saunders College Publishing, Philadelphia, P. 847, **1985**
- 21 Tiselius, A., *Trans. Faraday Soc.*, 33, 524, **1937**
- 22 Catsimpooolas, N., *Sep Sci.*, 6, 435, **1971**
- 23 Jorgenson, J.; Lukacs, K.D., *Anal. Chem.*, 53, 1298-1302, **1981**
- 24 Jorgenson, J.; Lukacs, K.D., *Science*, 222, 266-272, **1983**
- 25 Gordon, M.J.; Huang, X.; Pentoney, S. L.; Zare, R. N., *Science*, 242, 224-228, **1988**
- 26 Terabe, S., *Anal. Chem.*, 62, 605A-607A, **1990**
- 27 Lukacs, K. D.; Jorgenson, J., *J. HRC & CC*, 8, 407-411, **1985**
- 28 Grossman, P. D.; Colburn, J.C., *Capillary Electrophoresis: Theory and Practice*, Academic Press: San Diego, CA, **1992**
- 29 Ewing, A.; Wallingford, R. A.; Olefirowicz, T. M., *Anal. Chem.*, 61, 292A-303A, **1989**
- 30 von Hemholtz, H.L.F., *Wiss. Abhandl. Physik-tech. Reichsanstalt*, 1, 925, **1879**
- 31 Gouy, G., *J. Phys.*, 9 457, **1910**
- 32 Chapman, D.L., *phil.Mag.*, 25, 475, **1913**
- 33 Stern, O., *Elektrochem.*, 30, 508, **1924**
- 34 Stevens, T.S.; Cortes, H.J., *Anal. Chem.* 55, 1365, **1983**
- 35 Pretorius, V.; Hopkins, B.J.; Schieke, J.D., *J. Chromatogr.*, 99, 23, **1974**
- 36 Rice, L.L.; Whitehead, R.J., *Phys. Chem.*, 69, 4017-4024, **1965**
- 37 Reid, R.H.P., *J. Chromatogr. A*, 669, 151-183, **1994**
- 38 Lambert, W.J., Middleton, D.L., *Anal. Chem.*, 62, 1587-1591, **1990**,
- 39 Huang, T.L., *Chromatogr.*, 35, 395-398, **1993**
- 40 Long, C. (Editor), *Biochemist's Handbook*, Van Nastrand, Princeton, New Jersey, **1961**
- 41 Issac, H.J.; Janini, G.M.; Atamna, I.Z.; Muschik, G.M.; Lukszo, J., *J. Liq. Chromatogr.*, 15, 1129-1142, **1992**
- 42 Schutzner, W.; Kenndler, E., *Anal. Chem.*, 64, 1991-1995, **1992**

-
- 43 Li, S.F.Y., *Capillary Electrophoresis: principles, practice and applications*, Journal of Chromatography Library, Vol. 52, Chapter 5, **1992**
- 44 Issaq, H.; Atamna, I.; Muschik, G.; Janini, G., *Chromatographia*, 32, 155, **1991**
- 45 Altria, K.D.; Simpson, C.F., *Chromatographia*, 24, 527, **1987**
- 46 Altria, K.D.; Simpson, C.F., *Anal. Proc.*, 25, 85, **1988**
- 47 Bruin, G.J.; Chang, J.; Kuhlman, R.; Zegers, K.; Kraak, J.; Poppe, H., *J. Chromatogr.*, 13, 679, **1990**
- 48 Nashabeh, W.; Rassi, Z.E., *J. Chromatogr.*, 514, 57, **1990**
- 49 Issac, H.J.; Atamna, I.Z.; Metral, C.J.; Muschik, G.M., *J. Liq. Chromatogr.*, 13, 1247-1259, **1990**
- 50 Atamna, I.Z.; Metral, C.J.; Muschik, G.M.; Issac, H.J., *J. Liq. Chromatogr.*, 13, 2517-2527, **1990**
- 51 Issac, H.J.; Atamna, I.Z.; Muschik, G.M.; Janini, G.M., *Chromatogr.*, 34, 155-161, **1991**
- 52 VanOrmann, B.B.; Liversidge, G.G.; McIntire, G.L.; Olefirowicz, T.M.; Ewing, A.G., *J. Microcol. Sep.*, 2, 176-180, **1990**
- 53 Bushey, M.; Jorgenson, J., *J. Chromatogr.* 480, 301, **1989**
- 54 Landers, J.P.; Oda, R.P.; Spesberg, T.C.; Nolan, J.A.; Ulfelder, K.J., *Biotechniques*, 14, 98, **1993**
- 55 Green, J.S.; Jorgenson, J.W., *J. Chromatogr.*, 63, 478, **1989**
- 56 Schwer, C.; Kenndler, E., *Anal. Chem.*, 63, 1801-1807, **1991**
- 57 Fujiwara, S.; Honda, S., *Anal. Chem.*, 59, 487-490, **1987**
- 58 Fluri, K.; Qiu, X.; Harrison, J., *Analytical Methods & Instrumentation, Special Issue μ TAS'96*, 209-210, **1996**
- 59 Pfeffer, W.D.; Yeung, E.S., *Anal. Chem.*, 62, 2178, **1990**
- 60 Moring, S.; Nolan, J., *International Symposium on High Performance Capillary Electrophoresis*, San Francisco, **1990**

-
- 61 Guzman, N. A. (Editor), *Capillary Electrophoresis Technology*, Marcel Dekker, Inc., **1993**
- 62 Tsuda, T.; Nomura, K.; Nakagawa, G., *J. Chromatogr.*, **264**, 385, **1983**
- 63 Lee, C.S.; Blanchard, W.C.; Wu, C.-T., *Anal. Chem.*, **62**, 1550, **1990**
- 64 Rasmussen, H.T.; McNair, H.M., *J. Chromatogr.*, **516**, 223, **1990**
- 65 Grossman, P.D.; Soane, D.S., *Anal. Chem.*, **62**, 1593, **1990**
- 66 Atamna, I.Z.; Issaq, H.J.; Muschik, G.M.; Janini, G.M., *J. Chromatogr.*, **588**, 315, **1991**
- 67 Wieme, R.J., *Chromatographia, A Laboratory Handbook of Chromatographic and Electrophoretic Methods, Chap. 10*, 3rd ed., Van Nostrand Reinhold, New York, **1975**
- 68 Issaq, H.J.; Atamna, I.Z.; Muschik, G.M.; Janini, G.M., *Chromatographia*, **32**, 155, **1991**
- 69 Schutzner, W.; Kenndler, E., *Anal. Chem.*, **64**, 1991-1995, 1992
- 70 Rohlicek, V.; Deyl, Z.; Miksik, I., *J. Chromatogr. A*, **662**, 369-373, 1994
- 71 Coufal, P.; Stulik, K.; Claessens, H.A.; Cramers, C.A., *J. High Resoln. Chromatogr.*, **17**, 325-34, 1994
- 72 Virtanen, R., *Acta Polytechnica Scand.*, **123**, 1-67, 1974
- 73 Bello, M.S.; Capilli, L.; Righetti, P.G., *J. Chromatogr. A*, **684**, 311-322, 1994
- 74 Camilleri, P., in Camilleri, P.(Editor), *Capillary Electrophoresis: Theory and Practice*, CRC Press, Boca Raton, 1993, Ch. 1
- 75 Chien, R.-L.; Helmer, J.C., *Anal. Chem.*, **63**, 1354-1361, 1991
- 76 Sepaniak, M.J.; Powell, A.C.; Swaile, D.F.; Cole, R.O., in Grossman P.D. and Colburn, J.C. (Editors), *Capillary Electrophoresis: Theory and Practice*, Academic Press, Inc., San Diego, 1992, ch. 6
- 77 Liu, S.; Dasgupta, P.K., *Anal. Chim. Acta*, **283**, 739-745, 1993
- 78 Burgi, D.S., *Anal. Chem.*, **65**, 3726-3729, 1993
- 79 Stevens T.S.; Cortes, H.J., *Anal. Chem.*, **55**, 1365-1370, 1983
- 80 Seiler, K.; Fan, Z.F.; Fluri, K.; Harrison, D.J., *Anal. Chem.*, **66**, 3485-3491, 1994

-
- 81 Delapierre, G. *Sensors and Actuators*, 17, 123-138, **1989**
- 82 Gies, P. E.; Blanchard, R. B., *Semiconductor and Integrated Circuit Fabrication Techniques*, Peston Publishing Co.:Reston, VA, **1979**
- 83 Ko, W. H.; Suminto, J.T., in *Sensors: A Comprehensive Survey*, Grandke, T.; Ko, W. H.; Eds, VCH Press: Weinheim, Germany, 1, 107-168, **1989**
- 84 Fan, Z.H., *Ph.D Thesis*, University of Alberta, **1994**
- 85 Petersen, K.E., *Proceedings of the IEEE*, 70, 420-457, **1982**
- 86 Shoji, S.; Esashi, M.; Matsuo, T., *Sensors and Actuators*, 14, 101-107, **1988**
- 87 Van der Schoot, B. H.; Heanneret, S.; van der Berg, A.; de Rooij, N. F., *Sensors and Actuators*, B6, 57-60, **1992**
- 88 Wise, K. D.; Najafa, K., *Science*, 254, 1335-1342, **1991**
- 89 Rice, C.L.; Whitehead, R., *J. Phys. Chem.* 69, 4017-4024, **1965**
- 90 Jorgenson, J.M.; Lukacs, K.D., *Anal. Chem.* 53, 1298-1302, **1981**
- 91 Andreev, V.P.; Lisin, E.E., *Chromatogr.* 37, 202-210, **1993**
- 92 Hu, L., *Master Thesis*, Univ. Of Alberta, **1997**
- 93 Price, C.P.; Newman, D.J., Eds. *Principles and practice of Immunoassay*, Stockton Press: London, **1991**
- 94 Diamandis, E.P.; Christopoulos, T.K., Eds. *Immunoassay*, Academic: San Diego, CA, **1996**
- 95 Wild, D.G.; Davies, C.J., In *The Immunoassay Handbook*, Wild, D.C., Ed. Stockton Press: New York, **1994**
- 96 Pressman, D.; Eisen, H.N., *J.Immunol.*, 4,273, **1950**.
- 97 Nisonoff, A.; Hooper, J. E.; Spring, S. B., *The Antibody Molecule*, ,542, **1975**
- 98 Gally, J.A., *The Antigen*, Vol.1,Sela, M.,Ed., Acedemic Press, New York, 161, **1973**
- 99 Landsteiner, K., *The Specificity of Serological Reactions*, Dover, New York, 330, **1962**
- 100 Kabat, E.A., *J. Immuno.*,77,377, **1956**
- 101 Schechter,B.; Schechter, I.; Sela, M., *Immunochemistry*, 7, 587, **1970**

Chapter 2

Understanding Fluid Mechanics Within Microfluidic Device

Abstract

Leakage phenomenon is always an important issue when using the microfabricated device. We need to understand this phenomenon and have better controls to minimize this drawback. In this chapter, we investigate the leakage with T-shaped intersecting channels. With the different side channel lengths and side channel locations on the main channel, we come to the conclusion that leakage is affected strongly by the side channel geometry. Our result is compared to a newly developed model of fluidic mechanics with electrokinetically controlled manifolds. The efforts may provide a basis for future design rules for microfluidic devices.

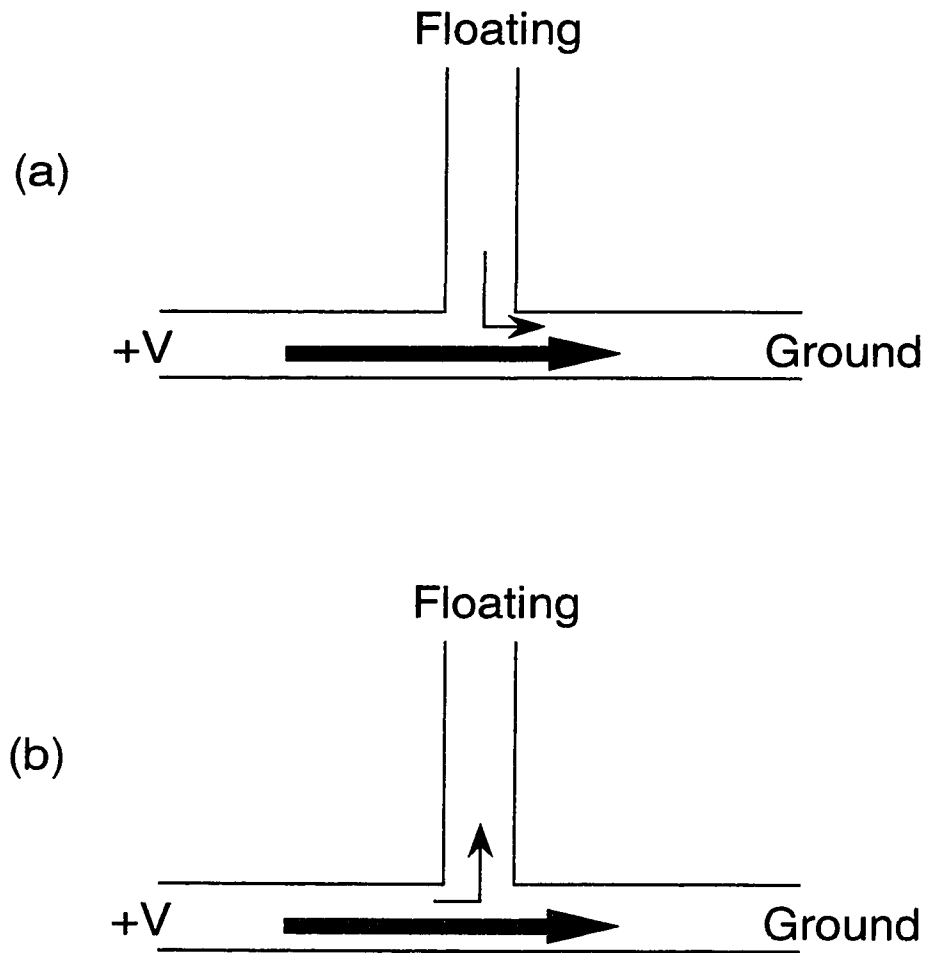
2.1 Introduction

Electrokinetic effects can be used to advantage to provide both separation and pumping action within glass microchip devices (1-26). Complex manifolds of channels have been utilized to drive mixing, reactions and separations within a chip, without the need for micropumps or valves. It is very important for us to understand the flow behavior in the microfabricated channels, so that we can properly design the chip to control the flow effectively. In this chapter we use a newly developed model that can describe the fluid mechanics within electroosmotically pumped flow manifolds, and then we present the experimental measurements which can be correlated with these predictions. No quantitative design rules for layouts exist at present, although some simple rules of thumb have been developed (1-3). A thorough understanding of fluid mechanics within electroosmotically pumped fluid networks will be of considerable benefit to their engineering.

In a manifold of capillary channels that has no valves, leakage of liquid between channels will occur at the intersection. In previous studies (3-6) it was reported that contamination of buffer by sample occurs during the separation step. This is due to diffusional leakage and convective mixing occurring at the intersection. The leakage phenomenon increased background signal and decreased the dynamic range of detection. However, the amount of leakage flow is dependent on the layout of the channels, such as the geometry of the intersection and the differences in resistance to fluid flow which result from capillary dimensions. Previous study (3-6) indicated that the electroosmotic flow along one of the channels caused convective flow out of the

intersecting channel. The convective flow most likely arises from frictional forces within the solvent that lead to a transfer of momentum from flowing stream to the stagnant fluid in the side channel (27). This is consistent with the observed leakage flow directions (5,6). Scheme Ia illustrates leakage from a side channel. In some experimentation a phenomenon referred to as pushback is observed, in which flow unexpectedly enters into a side channel instead of leaking from it. This concept is illustrated in Scheme Ib.

Leakage or pushback flow can be suppressed by applying an active voltage to push sample back towards the sample reservoir during the separation period (4). This control voltage should be chosen carefully so that the electrical back pressure balances the leakage force. Resistance simulation (3) is very effective in predicting the potential at a particular point and guiding selection of an appropriate potential for each reservoir. However, these values are not completely accurate owing to the effects of fluid mechanics. We need to make the most suitable design to achieve our on-chip sample introduction, mixing, reaction and separation, and we must have thorough control over all of these processes. Consequently, it is essential to understand the fluid mechanics within electroosmotically pumped flow manifolds.



Scheme I (a) Leakage flow from a side channel. (b) Pushback flow into a side channel.

2.2 Theory

2.2.1 Definitions of different velocities used in this chapter

There are several different velocity terms used in this chapter. To make them clear, we give the following definitions.

Electrophoretic velocity is the component of the linear velocity of the dye that is due to the electrophoretic mobility of the dye.

EOF is the electroosmotic flow rate given by μ_{eo} and the electric field applied.

Dye velocity is the observed linear flow rate of the dye, which is determined by the vector sum of the electroosmotic mobility of the solvent, μ_{eo} , the electrophoretic mobility of the dye, μ_{ep} , and any pressure driven flow. Any or all of these components may be present, depending upon conditions.

Solvent velocity is the linear flow rate of the solvent, determined by μ_{eo} and any pressure driven flow. Either or both of these components may be present, depending upon conditions.

2.2.2 The model

A theoretical model (28-30) of electrokinetic flow in microfluidic devices was developed by Hu and Masliyah of the department of Chemical Engineering, in collaboration with Harrison of the Department of Chemistry at the University of Alberta. This model is described below and is referred to as “the model” throughout

Chapter 2 and 3 of this thesis. This model considers electroosmotic flow of an electrolyte solution inside a parallel plate channel with a uniform parallel inlet axial velocity distribution. The pressures at the ends of the channels are of the same value.

The electrolyte solution is idealized as a fluid with a constant bulk concentration, viscosity, density and dielectric constant. This has the advantage that the use of the Nernst-Planck equation can be avoided once the bulk ionic concentration is taken as constant along the channel. Following Henry's (31) classical analysis of electrokinetic flow, it is assumed that total electrostatic potential can be expressed as a linear superposition of the potential due to the electric double layer (ψ), which would exist in the absence of the applied electric field, and the potential that arises from the applied external field (ϕ). Figure 2-1 shows the coordinates of the T shaped channels for which ultimately we will obtain the total potential. It is assumed that $\phi_{\text{total}} = \phi + \psi$. ϕ_1 , ϕ_2 and ϕ_3 are electric potentials applied at each reservoir. ψ_s and ψ'_s are the surface potentials in the main and side channel respectively. According to the Guoy-Chapman model, the surface potential is taken to be the zeta potential and the ions are modelled as point charges.

The governing equations are based on the Navier-Stokes equation with a term for electrokinetic migration included, which is coupled to the Guoy-Chapman model of the interfacial double layer that drives electroosmotic pumping. Three sets of equations must be solved simultaneously in the two dimensions indicated in Figure 2-1, x and y: the Poisson-Boltzmann equation for the double layer potential ψ , the Laplacian for the applied electrostatic field, ϕ , and the Navier-Stokes equation modified to include

electrokinetic migration. The transport equations, expressed in dimensionless variables become:

$$\frac{\partial P}{\partial X} = \frac{\partial^2 U}{\partial X^2} + \frac{\partial^2 U}{\partial Y^2} + \sinh \Psi \frac{\partial(\Psi + \Phi)}{\partial X} \quad 2-1$$

$$\frac{\partial P}{\partial Y} = \frac{\partial^2 V}{\partial X^2} + \frac{\partial^2 V}{\partial Y^2} + \sinh \Psi \frac{\partial(\Psi + \Phi)}{\partial Y} \quad 2-2$$

$$\frac{\partial U}{\partial X} + \frac{\partial V}{\partial Y} = 0 \quad 2-3$$

Definitions of the symbols and the boundary equations used are given in Tables 1 and 2, and the coordinate system for this 2-D model is illustrated in Figure 2-1. All these variables for the theoretical model are reduced variables.

Table 2-1 Definitions and Reduced Variables

Ψ = double layer potential	v = linear velocity along y dimension	$\sigma = ze/kT = \frac{1}{25} \text{ mV at } 25^\circ\text{C}$
Ψ_s = surface potential	p = pressure	$\Psi = \sigma\Psi; \zeta = \sigma\Psi_s; \Phi = \sigma\phi$
a = half width of channel	μ = viscosity	$U = u/\langle u \rangle; V = v/\langle u \rangle; P = \frac{ap}{\mu \langle u \rangle}$
κ = Debye double layer length	P_0 = reduced inlet and outlet pressure	$\langle u \rangle = 2 n_\infty a kT/\mu$
u = linear velocity along x dimension	n_∞ = # density of charged particles (m^{-3})	$X = x/a; Y = y/a$

Table 2-2 Boundary Conditions

Walls

$$Y = \pm 1 \quad \Psi = \zeta \quad ; \quad X = \pm 1 \quad \Psi = \zeta' \quad \frac{\Phi}{X} = \frac{\Phi}{Y} = 0 \quad ; \text{ no slip wall boundaries}$$

Ends

$$\frac{d^2\Psi}{dY^2} = (\kappa a)^2 \sinh \Psi \quad ; \quad \frac{d\Psi}{dY} = 0 \text{ at } Y = 0 \quad \Psi = \zeta \text{ at } Y = \pm 1 \text{ Plus equivalent expressions in } Y\text{-dimensions}$$

$$\Phi = \Phi_1 \text{ at } X = -L_1 \quad \Phi = \Phi_3 \text{ at } X = L_3 \quad \Phi = \Phi_2 \text{ at } X = L_2 \quad \frac{dU}{dX} = 0, V = 0 \text{ at } X = L_2, -1 < Y < 1$$

$$U = U_m, V = 0 \text{ at } X = -L_1, -1 < Y < 1 \quad V = V_m, U = 0 \text{ at } Y = L_s, -1 < X < 1 \quad P = \cosh \Psi + P_0$$

Assuming equilibrium, the Poisson-Boltzmann equation for the double layer and the Laplacian equation for the external electric potential distribution can be decoupled from the transport equation. The electric potential distribution due to the double layer and the electric field are obtained first, and the velocity and pressure profile can be obtained. The numerical method used to solve the Poisson-Boltzmann and the Laplacian equation is straight forward, therefore, the results of the electric potential distributions due to the electrical double layer and the external electric field can be calculated.

The next step is the numerical implementation of the flow equation. The normalized governing transport equations form a set of elliptic partial differential

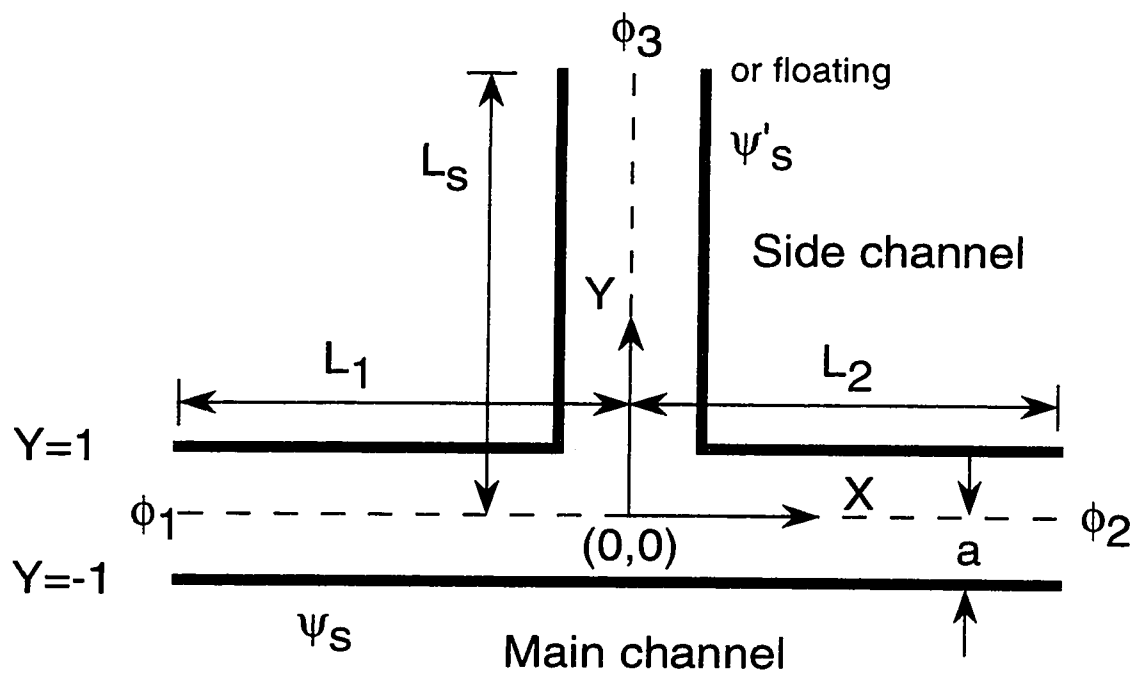


Figure 2-1 Coordinates and boundary conditions used for calculations. See Table 2-1 and Table 2-2 for definitions. All variables are reduced variables. (Adapted from references 30,35)

equations, which can only be solved numerically. Based on the assumption that the flow is in the creeping flow regime and that the Boltzmann distribution can be invoked, the potential distribution can be decoupled from the transport equations. The extreme dimensional difference between the double layer thickness and the fluid channels made a variable grid method especially critical (28,30), and the character of the double layer meant special care was required in stating the boundary conditions. Once the electrical potential distributions are obtained, the major calculation step is the solution of the transport equations as presented by the modified Navier-Stokes and the continuity equations (31-34).

The entrance effect on the electroosmotic flow obtained from the calculation shows that the pressure profile along the centerline of the channel undergoes a sharp drop at the entrance mouth, as shown in Figure 2-2. This is because of a transverse pressure distribution due to the electric double layer when the electrolyte enters the capillary channel. The pressure then gradually recovers to the outlet value, which is the same as the inlet pressure. With this concept, the model leads to the result that both electrokinetics and pressure play important roles in the control of the electroosmotic flow in capillary electrophoresis. From these results one can expect that hydrodynamic effects can be very important for a manifold channel system in which both sample injector and electrophoresis system are integrated together. Many further details of this model are presented in the thesis of L. Hu (30), in Department of Chemical Engineering, University of Alberta. Comparisons to those calculations will be presented throughout this chapter.

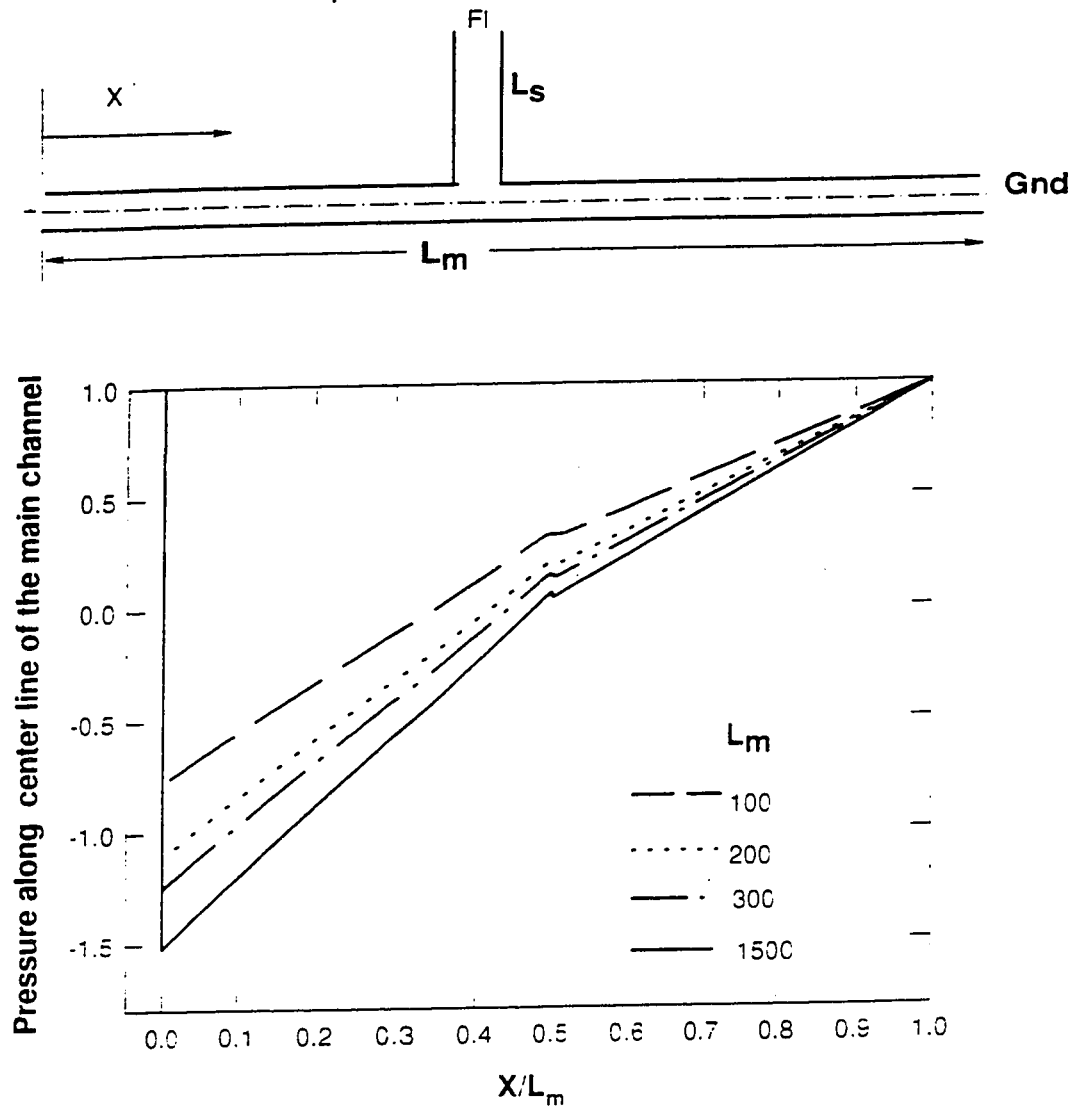


Figure 2-2 Pressure profiles along the centerline of the channel for different main channel length, L_m , showing a pressure drop at the entrance of the channel. (Adapted from reference 30)

2.3 Experimental Section

2.3.1 Device fabrication

Glass devices (3 in. X 3 in.) were fabricated at the Alberta Microelectronics Center, using microlithographic patterning and an HF/HNO₃ etchant, with a modified silicon micromachining technique (6). The substrates were 200 µm thick 0211 glass plates (Corning Glass Works, Corning NY), Pyrex glass (paragon Optical, Reading, PA), and Photomask glass (Agfa-Gevaert, Belgium) . They were cleaned ultrasonically in detergent (5% Sparkleen, Fisher Scientific), methanol (Reagent Grade), and deionized water in an ultrasonic bath in a class 100 clean room environment. A H₂SO₄/H₂O₂ etch was also used as an option. A metal mask, normally consisting of Cr/Au/Cr (200/1000/200 Å thickness), was evaporatively deposited under vacuum (<10⁻⁶ torr), and trace organics were then removed in H₂SO₄ (98%) : H₂O₂ (30%) at a 3:1 ratio. A 1.4 µm thick positive photoresist (Waycoat HPR 504, Olin Hunt) was spin coated on the metal with a Solitec photoresist coater/developer (3500 rpm), then soft-baked at 110 °C for 5 minutes, as Figure 2-3a.

Photomask layout was designed with L-Edit software (Tanner Research Inc., Pasadena, CA), and the master mask was manufactured by Precision Photomask (Ottawa, Canada). A contact mask aligner (Karl Suss MA4) was used to align the mask with the glass substrates. The photoresist was exposed to UV light (365-405 nm) for about 3 seconds, Figure 2-3b, and Microdeposit 354 (Shipley, Newton MA) was used as

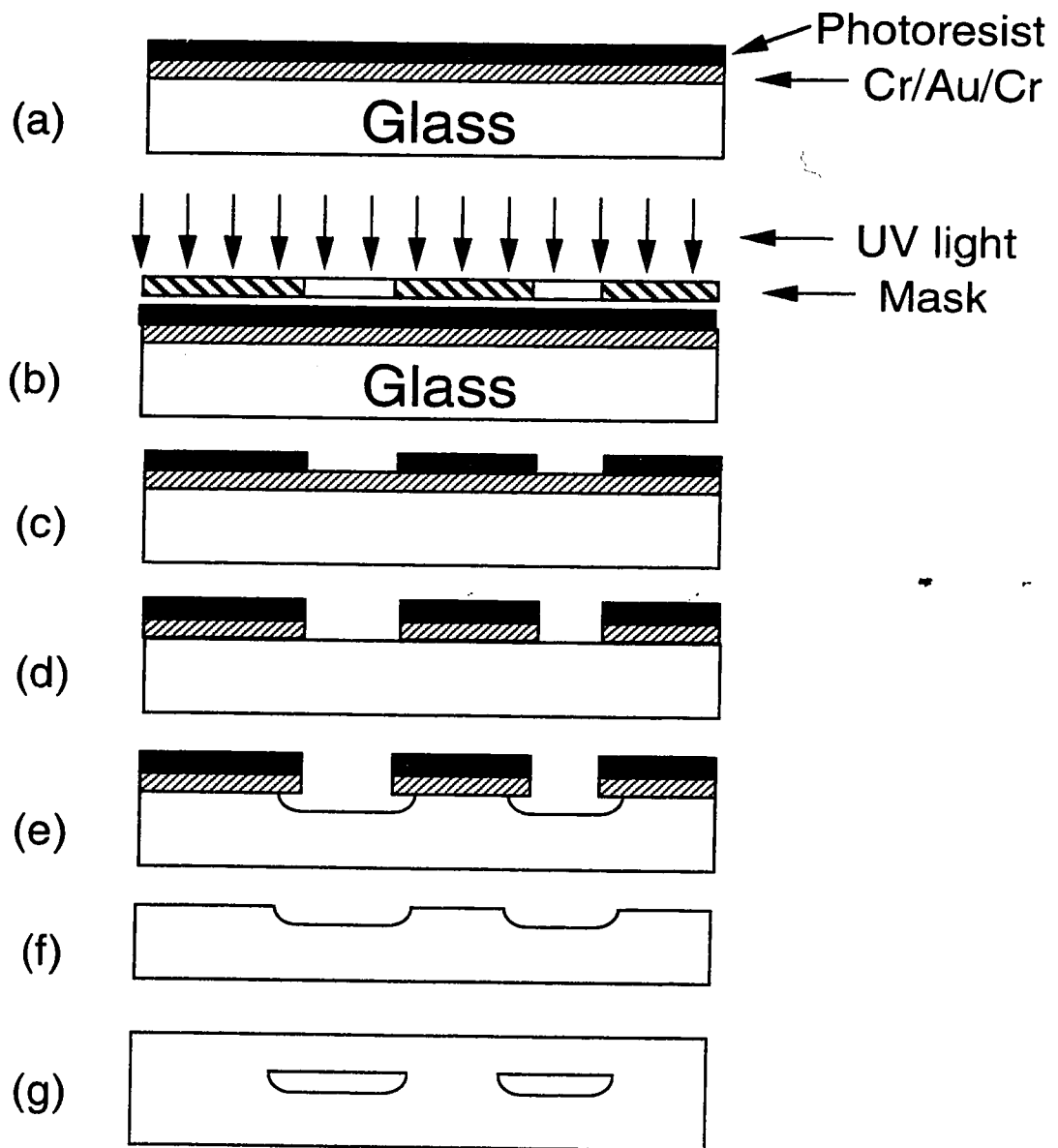


Figure 2-3 The sequence of photolithographic fabrication: (a) Cr and Au masked glass plate is coated with photoresist; (b) Sample is exposed to light through a master mask; (c) Photoresist is developed; (d) Exposed metal mask is etched; (e) Exposed glass is etched; (f) Resist and metal are stripped; (g) Glass cover plate is bonded to form capillary (Adapted from Z. Fan, Ph.D Thesis).

developer to obtain a 10-200 μm line-width for channel definition, Figure 2-3c. Following a hard baking at 120 $^{\circ}\text{C}$, 5 minutes, the metal layer was etched away with *aqua regia* and a commercial Cr etch (KTI Chemicals, Sunnyside, CA), as shown in Figure 2-3d. The photoresist was not removed from the remaining metal layer, so as to reduce the impact of pinholes in the metal. The exposed glass was etched in a slowly stirred mixture of concentrated $\text{HF}:\text{HNO}_3:\text{H}_2\text{O}$ (20:14:66), Figure 2-3e. The channel depth during etching was monitored with an Alpha-step profilometer (Tencor Ind., Mountain View, CA) to establish the etch rate, and was then controlled by timing the etch period. The photoresist and metal masks were then removed with the etches described above, Figure 2-3f.

In this experiment, channels of 10 μm depth were etched on one glass plate. Both the etched glass and a cover plate with holes (1.5 mm) drilled with a diamond drill bit for external access, were cleaned as described above, followed by pressure washing using a Model 2066 High Pressure Cleaning Station (MicroAutomation, CA) under a class 100 clean hood. With careful alignment of the access holes to the etched channels, the cover plate is thermally bonded to the etched plate, Figure 2-3g. The temperature used for photomask and 0211 glass was at 595 $^{\circ}\text{C}$ for 6 hours, and for Pyrex and borofloat glass was at 650 $^{\circ}\text{C}$ for 6 hours. Complete contact between the two glass plates was ensured so no weight was added for the initial bonding, however, small pieces of weight would be put on the unbounded areas for repeating the temperature program if the initial bonding was not successful. The maximum used heating cycles were three. The bonding quality was satisfactory for all four kinds of glass materials.

Plastic pipette tips, which were cut to fit the access hole and glued to the top plate with epoxy, served as the solution reservoirs.

2.3.2 Device design

To evaluate the leakage phenomenon, we designed a series of layouts with “T” shaped channels, from which leakage is expected (3,5,6). The layouts of devices UACQ1 and UACQ2 are shown on the top of Figure 2-4. In both of the devices, all main channels are 49.0 mm long, all channels have a width of $30\text{ }\mu\text{m} \pm 2\text{ }\mu\text{m}$, and a channel depth of $10\text{ }\mu\text{m} \pm 2\text{ }\mu\text{m}$. Side channels have different lengths; they are 5.0 mm, 10.0 mm, 20.0 mm and 40.0 mm for each layout, labeled #1, #2, #3, and #4, respectively, in both devices. For device UACQ1, all of the side channels are located in the center of the main channels. For device UACQ2, all side channels are located 10.0 mm from one end and 38.0 mm from the other end of the main channels. Wider channels, 300 μm , were added in some of the layouts to allow the access holes to be located further away from the position of the microscope objective. The length of the wider channel was converted to the equivalent length of the normal channel (5), and was included in the total length described above. On the bottom of Figure 2-4, the layout indicates the definitions used, where the horizontal channel is the main channel, and the vertical one is the side channel, which contains the sample dye solution. L_1 and L_2 indicate the lengths of the main and side channels, V_1 and V_2 are the voltages applied to main and side channels. V_3 was always held at Ground in these experiments.

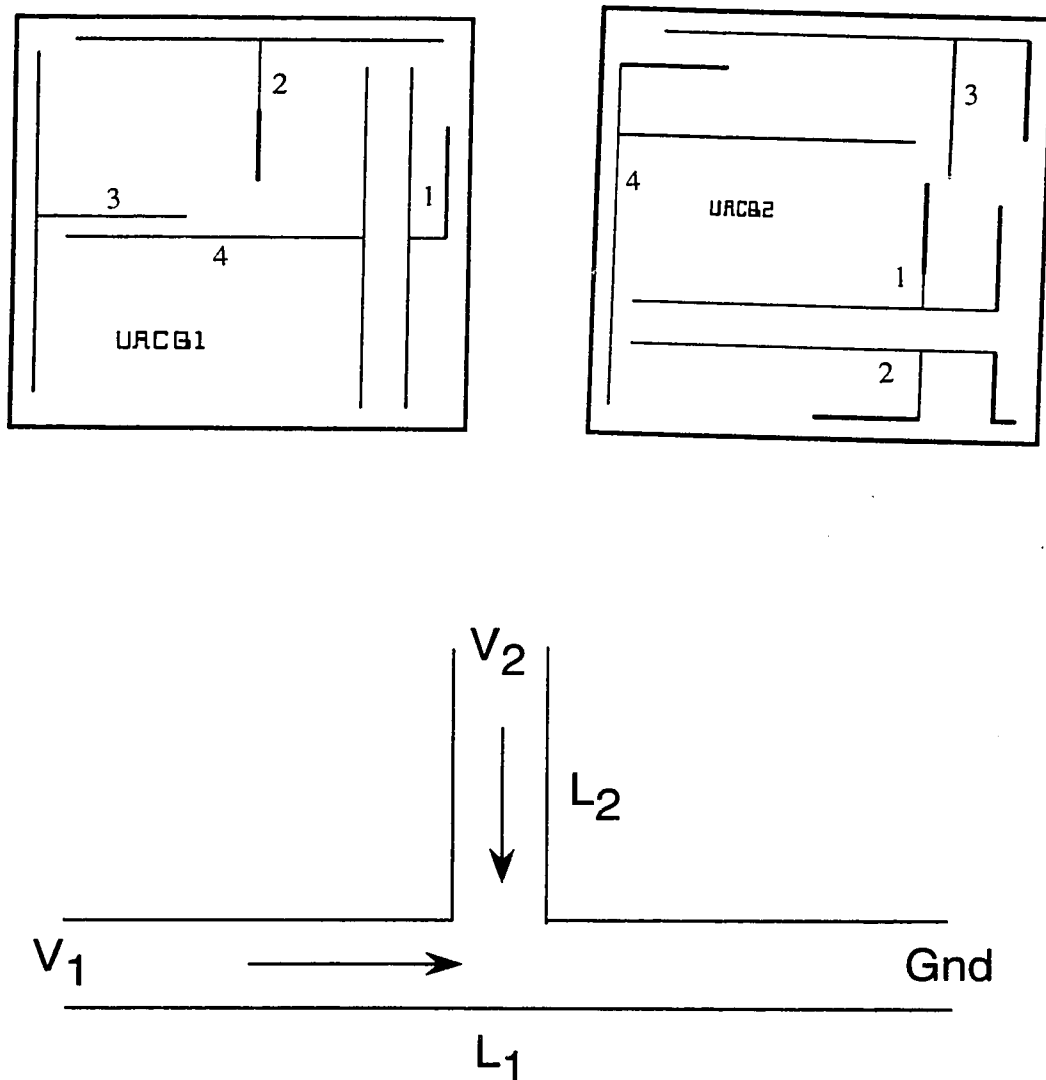


Figure 2-4 Channel dimensions and layout of the devices. All channels are $10\text{ }\mu\text{m}$ deep and $30\text{ }\mu\text{m}$ wide, except for the “fat” channels of $200\text{ }\mu\text{m}$ width. All main channels are 49.0 mm in length. Devices #1: side channel 5.0 mm ; Devices #2: side channel 10.0 mm ; Devices #3: side channel 20.0 mm ; Devices #4: side channel 40.0 mm . L_1 and L_2 are the lengths of main and side channels; V_1 and V_2 are voltage applied to main and side channels.

From the above, we can see that the series of layouts was designed with the side channel located at different positions along the main channel, and with the side channel having various length. In this way, we aimed to find the best location of the side channel along the length of the main channel and the most suitable length of the side channel for minimizing the leakage phenomenon.

2.3.3 Instrument

The block diagram in Figure 2-5 illustrates the apparatus used for the experiments. The computer-controlled power supply system (± 3 kV and ± 15 kV MJ Series, Glassman High Voltage, Whitehouse Station, NJ; 30 kV Kilovac, Santa Barbara, CA) and relays (Control 488/16, IOtech Inc., Cleveland, OH) are similar to those described elsewhere (5,6). They are controlled by a Power Macintosh 7100/66 in this microfluidic study. LabView programs (National Instruments Corp., Austin, TX) written locally were used for instrument control and data acquisition/analysis. Laser induced fluorescence detection was accomplished using a 488 nm air-cooled argon ion laser (Uniphase/Ionics Model 2011, Newport, Research) operating at 3.2 mW output to excite fluorescence. The beam was focused to about a 30 μm spot size in the device channel. Emission was collected with a 7x Rolyn objective (0.2 NA), then directed onto a Hamamatsu photomultiplier tube (PMT) after passing through a 200 μm pinhole located at the image plane of the lens. A 518 nm optical band pass filter (Omega Optical, Brattleboro, VT) with 15 nm bandwidth was used to eliminate scatter of the 488 nm laser source, and to reduce background fluorescence from the glass. The

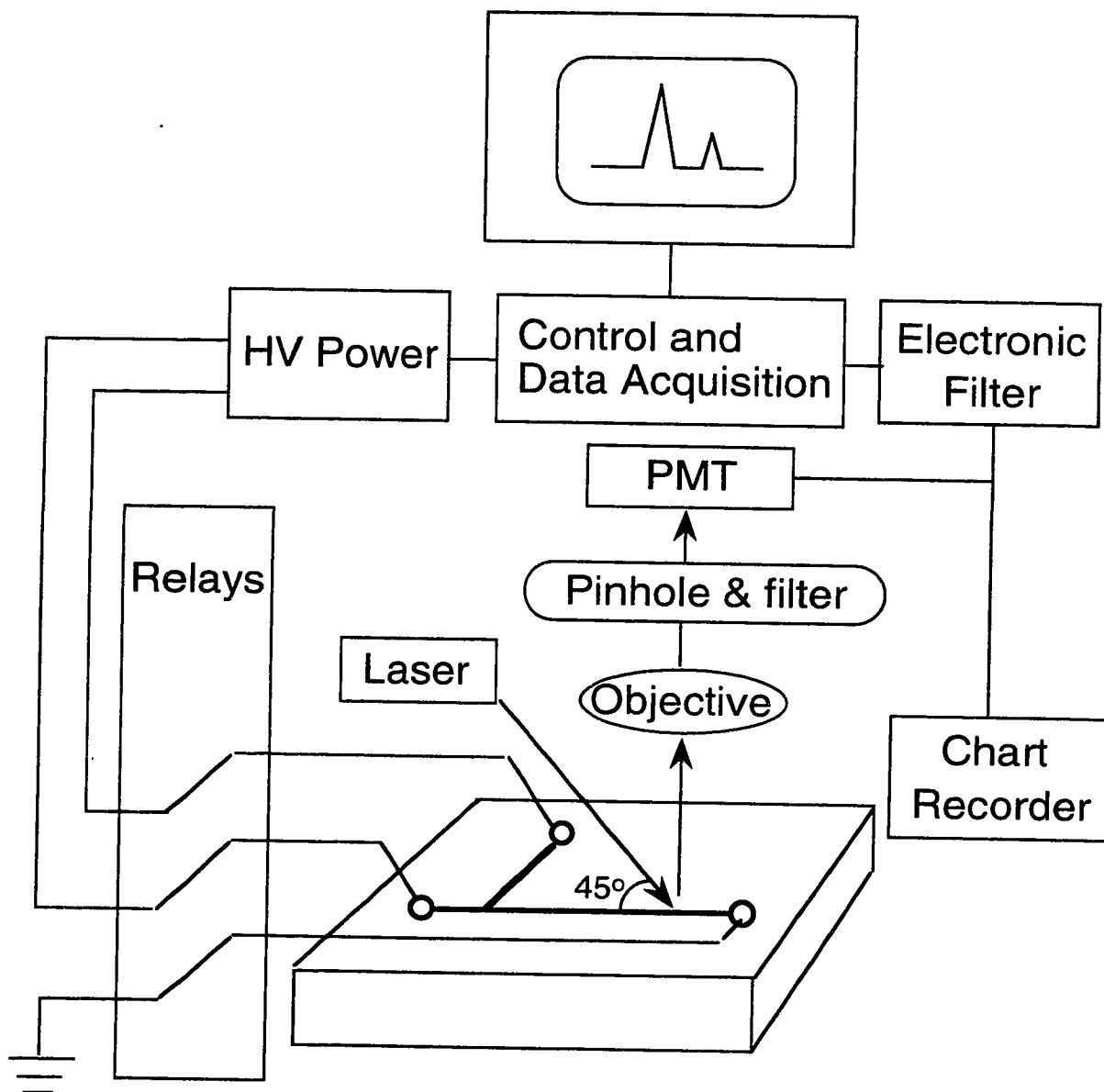


Figure 2-5 Block diagram of the high voltage relay controlled system, with computer control and digital data acquisition of laser excited fluorescence.

emission signal was electronically filtered with a cascade of active 4-pole Butterworth and 4-pole Bessel filters with 25 Hz low pass cut-off frequency and recorded simultaneously on a Fisher Linear strip chart recorder and a Macintosh 7100/66 computer. The current in the channels was monitored from the potential drop across a 10 k Ω resistor, which was located between the channel reservoir and the power supply ground, and recorded on a strip chart recorder (Model 7128, Hewlett Packard). The peak parameters, such as area and the number of theoretical plates, were calculated using statistical moments analysis. Software used were LabView (National Instrument Corp., Austin, TX) and Igor (Wavemetrics, Lake Oswego, OR).

2.3.4 Materials and Reagents

Borosilicate glass (Pyrex, Borofloat) was from Paragon Optical (Reading, PA). Photomask glass was from Agfa-Gevaert (Belgium) and 0211 glass was from Corning glass (Parkridge, IL). Microslides and Sparkleen detergent were from Fisher Scientific (Edmonton, Canada). The Hollow diamond drill bit was purchased from Lunzer (Saddle Brook, NJ). Crystal bond came from Aremco (Ossining, NY).

The buffer for all electrophoresis studies was made of 20 mM tris(hydroxymethyl)aminomethane (Tris) (Terochem, AB, Canada), 5 mM boric acid (J.T. Baker Chemical CO, Phillipsburg, NJ.) and 4 mM KCl. It was used to prepare a series of buffers with different pH values of 9.19, 9.02, 8.83, 8.62, 8.39, 8.20, 7.97, adjusted with 0.1 M HCl. With the high salt concentration of the original buffer, these buffers of different pH will remain at the same ionic strength, given the low ionization

of tris and boric acid. The Na⁺ salt of fluorescein (Molecular Probes, Eugene, OR) was dissolved into the pH 9.19 buffer at a concentration of 2.0 μ M for all of the studies except where otherwise indicated, ensuring the sample had the same ionic strength as the buffer. This prevented sample stacking effects and ensured a constant solution conductivity. Fluoresbrite Carboxy YG 6 Micron microspheres (Molecular Probes, Eugene, OR) were used in the particle counting experiment.

2.3.5 Operating Procedure

All reagents were introduced to the channels through syringes equipped with 0.22 μ m microfilters. Running buffer was introduced to all the reservoirs at the beginning of each experiment and channels were flushed with buffer by vacuum for 15 minutes. Fine Pt wires with insulating sleeves were inserted into the reservoirs on the device as electrodes. Fluorescent sample was then introduced into the side channel, and potentials were applied either between sample reservoir and sample waste, or buffer reservoir and separation waste, for injection or separation modes, respectively. Solutions in reservoirs were replenished between 15 minutes to 1 hour to prevent electrolysis. An Argon ion laser beam at 488 nm was focused into the channel, and the photomultiplier tube was aligned with the dye present in the region of detection. After use, channels were flushed by vacuum with 0.1 N NaOH for 20 minutes, followed by MilliQ Ultrapure water flush for 20 minutes. Chips were stored with pure water filling all the reservoirs and channels, and covered with parafilm to prevent water evaporation.

2.4 Results and Discussions

2.4.1 Electroosmotic mobility

Electrokinetic driving forces were used throughout this work to pump fluid and move ions. Because the overall mobility depends on μ_{eo} and μ_{ep} it is important to be able to separate these factors. In this first section we present a study of μ_{eo} and μ_{ep} for fluorescein at different pH values and in different materials. Some of this data is important for Chapter 2, while some is also highly relevant to Chapter 3.

We wanted to study the effect of varying the ζ potential at mixing points within the chip on the fluid dynamics. As a first step we needed to show the electroosmotic mobility as a function of solvent pH in our microfabricated device. In our experiment, the buffers had constant ionic strength, but with different pH values. We performed two types of separations: one was done in capillary, where we separated a neutral marker, mesityl oxide, from fluorescein in order to measure the electroosmotic mobility and electrophoretic mobility of fluorescein in a fused silica capillary. The second study was a separation of fluorescein on-chip to measure the total observed mobility of fluorescein on-chip. With these two sets of mobility measurements, we can calculate the electroosmotic mobility of solvent on-chip. We assumed that the electrophoretic mobility was the same for capillary and chip measurements.

2.4.1.1 Electroosmotic mobility study from capillary

Electroosmotic mobility was first measured in a capillary to evaluate the solvent flow behavior. The study was carried out with the Na⁺ salt of Fluorescein, which is the same dye used for mobility measurement on chip with LIF detection; mesityl oxide was used as a neutral marker added at 0.01 wt.% weight to monitor the electroosmotic mobility of the solvent. The system used was a Beckman CE P/ACE 5010, with 214 nm UV detection. The capillary was 27 cm in length, with only 20 cm to the detector window. The sample was injected under pressure for 4 seconds, followed by separation with 15 kV for 7 minutes.

The different mobilities were related by Equation 2-1:

$$\mu_{obs} = \mu_{eo} + \mu_{ep} \quad 2-1$$

where μ_{obs} is the total observed mobility, μ_{eo} is the electroosmotic mobility, and μ_{ep} is the electrophoretic mobility of the fluorescein dye. From the electrophoregram, we obtained two peaks: the first was from the neutral marker, which is due to μ_{eo} only, and the second was from the dye, which represented the total observed mobility, μ_{obs} . Knowing the retention time, t_R , and the path length between the capillary inlet to the detector window, L , the flow velocity, v , can be calculated with Equation 2-2.

$$v = \frac{L}{t_R} \quad 2-2$$

Then with Equation 2-3, individual mobilities, μ , can be calculated from velocity, v , and the electric field strength, E . E is determined by the applied voltage and the total capillary length.

$$\mu = \frac{v}{E} \quad 2-3$$

The measured μ_{eo} and μ_{obs} at room temperature, as well as the calculated μ_{ep} in the capillary in different pH buffers are listed in Table 2-3.

Table 2-3 Measured mobilities in capillary (using mesityl oxide)

Buffer pH	$\mu_{eo} \times 10^{-4} \text{ (cm}^2\text{/V}\cdot\text{s)}$	$\mu_{obs} \times 10^{-4} \text{ (cm}^2\text{/V}\cdot\text{s)}$	$\mu_{ep} \times 10^{-4} \text{ (cm}^2\text{/V}\cdot\text{s)}$
9.19	$6.45 \pm 0.02_3$	$3.39 \pm 0.02_2$	$-3.06 \pm 0.03_2$
9.02	$5.77 \pm 0.01_9$	$3.00 \pm 0.02_2$	$-2.77 \pm 0.02_9$
8.83	$5.56 \pm 0.01_7$	$2.83 \pm 0.01_9$	$-2.73 \pm 0.02_5$
8.62	$5.45 \pm 0.01_6$	$2.72 \pm 0.01_7$	$-2.73 \pm 0.02_3$
8.39	$5.38 \pm 0.01_3$	$2.69 \pm 0.01_4$	$-2.69 \pm 0.01_9$
7.97	$5.32 \pm 0.01_3$	$2.67 \pm 0.01_1$	$-2.65 \pm 0.01_7$

From the above table, we can see that with the solvent pH increase μ_{eo} increases; meanwhile the μ_{ep} of fluorescein becomes more negative. This μ_{eo} increase is due to the ζ potential increase when the pH rises. Additionally, the electroosmotic mobilities of

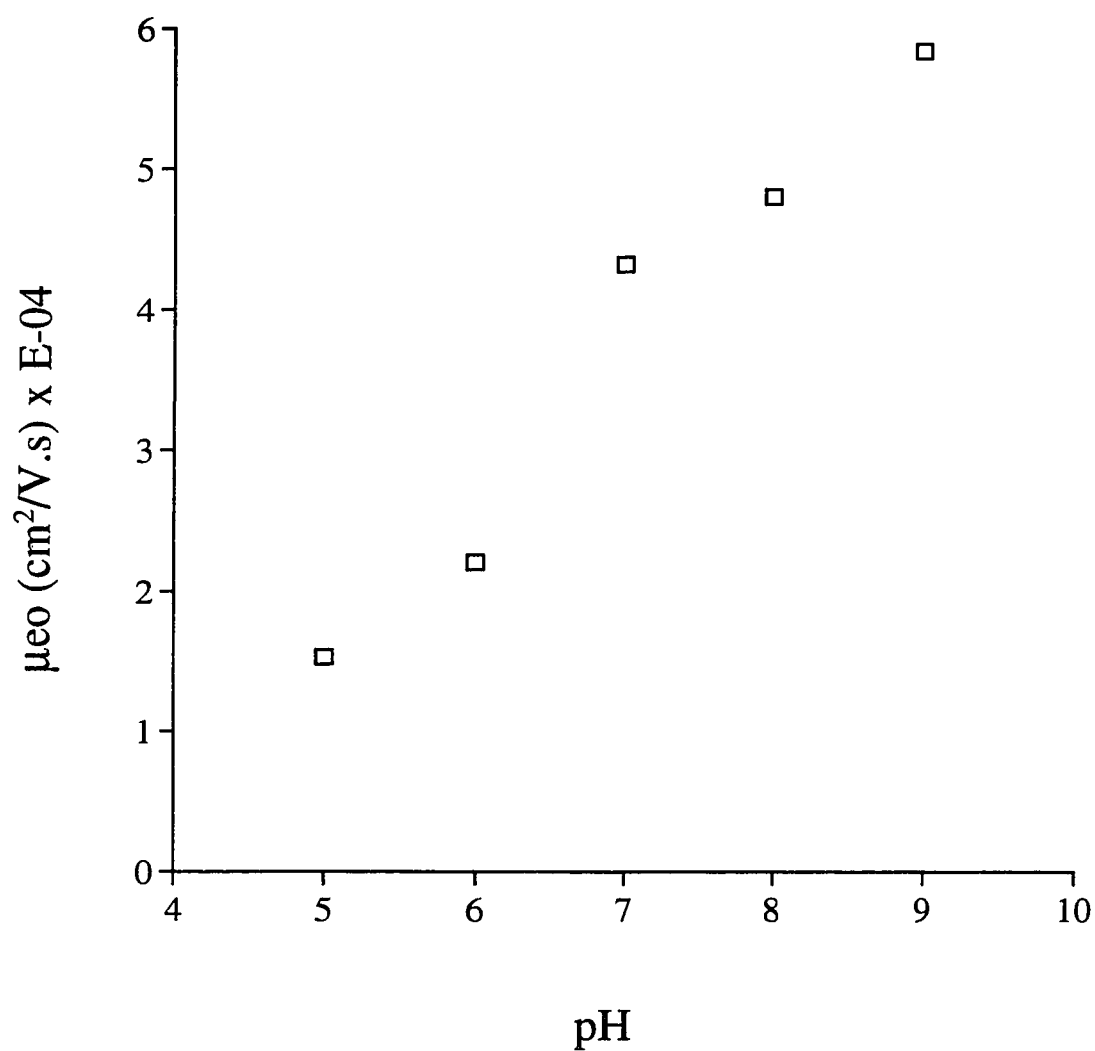


Figure 2-6 Electroosmotic mobility of buffer at different pH values. Buffers were 20 mM Tris, 4 mM boric acid, with 5 mM KCl to control ionic strength. 1 M HCl was used to adjust pH values. (The error bars are smaller than the data points.)

buffers at pH 5, 6, 7, 8, and 9 were measured and are plotted in Figure 2-6, giving the electroosmotic mobility change as a function of a broader pH range. The plot showed the same trend as Table 2-3: μ_{eo} increases with the rising pH. Higher pH raises the surface charge by more deprotonation of the surface, which leads to a greater ζ potential and so to a greater μ_{eo} .

2.4.1.2 Electroosmotic mobility on chip

In this study, we performed separation on-chip and measured the observed mobility of the dye. We used buffers with pH 9.19, 9.02, 8.83, 8.62, 8.39, 8.20, and 7.97, which were the same buffers as we used for the mobility measurements with the capillary. The Na^+ salt of fluorescein was prepared in the buffers with different pH values and used as our sample for LIF detection.

The following data was obtained from a Pyrex glass device, with a side channel length of 40.0 mm, and the main channel length was 48.0 mm. Separation voltage of 1 to 5 kV was applied to the main channel after a small sample plug was injected from the side channel to the main channel outlet. The detector was located 1 cm from the main channel outlet to record the signal intensity and the migration time of the peak. Total observed mobility was obtained by plotting the measured migration time as a function of applied voltage, as shown in Figure 2-7. As we can see, when the applied voltage increases, the reciprocal of migration time increases. The plots had very good linearity, with the slopes indicating the observed mobilities for the Na^+ salt of fluorescein at

individual pH values. Figure 2-7 showed that μ_{obs} on-chip decreased with increasing solvent pH in the range of pH 8 to pH 9.2. The values of the observed mobility are 1.84, 2.47, 2.58, 2.84, 3.20, and $3.27 \times 10^{-5} \text{ cm}^2/\text{V}\cdot\text{s}$ for pH values of 9.19, 9.02, 8.83, 8.62, 8.39, and 7.97, respectively.

Initial measurements of mobility vs. pH were done without controlling the ionic strength of the buffer with KCl. The buffer was composed of 100 mM Tris and 20 mM Boric acid, at pH values of 9.0, 8.5, 8.0, and 8.0 adjusted by 1 M HCl. The device used was made of Pyrex glass, with a side channel length of 20.0 mm, and the main channel length of 48.0 mm. The separation voltage of 1 to 5 kV was applied to the main channel, after a sample plug was injected from the side channel to the main channel waste. The detector was located 1 cm away from the separation waste to record the migration time of the peak. The results showed the commonly expected trend of μ_{obs} increasing with pH, as seen in Figure 2-8. The values of the observed electroosmotic mobility are 7.05, 5.25, 4.33 and $3.92 \times 10^{-5} \text{ cm}^2/\text{V}\cdot\text{s}$ for pH values of 9.0, 8.5, 8.0, and 7.5. However, without a constant ionic strength we could not be certain whether pH or ionic strength caused the observed variation. Consequently, we added 5 mM KCl to all solutions. The effect was significant. Before we controlled the ionic strength, the current with 4 kV applied to the main channel varied between 0.05, 1.2, 2.1, and 3.5 μA for buffers with pH values of 9.0, 8.5, 8.0 and 7.5. However, with 5 mM KCl, the current was stable, it remained as 4.1-4.3 μA with 4 kV applied for buffers with pH values of 9.0 to 8.0 with 0.2 increments. For the leakage studies, the recorded current values were between 1.2 to 2.2 μA for applied voltages varying between 200-2000 V.

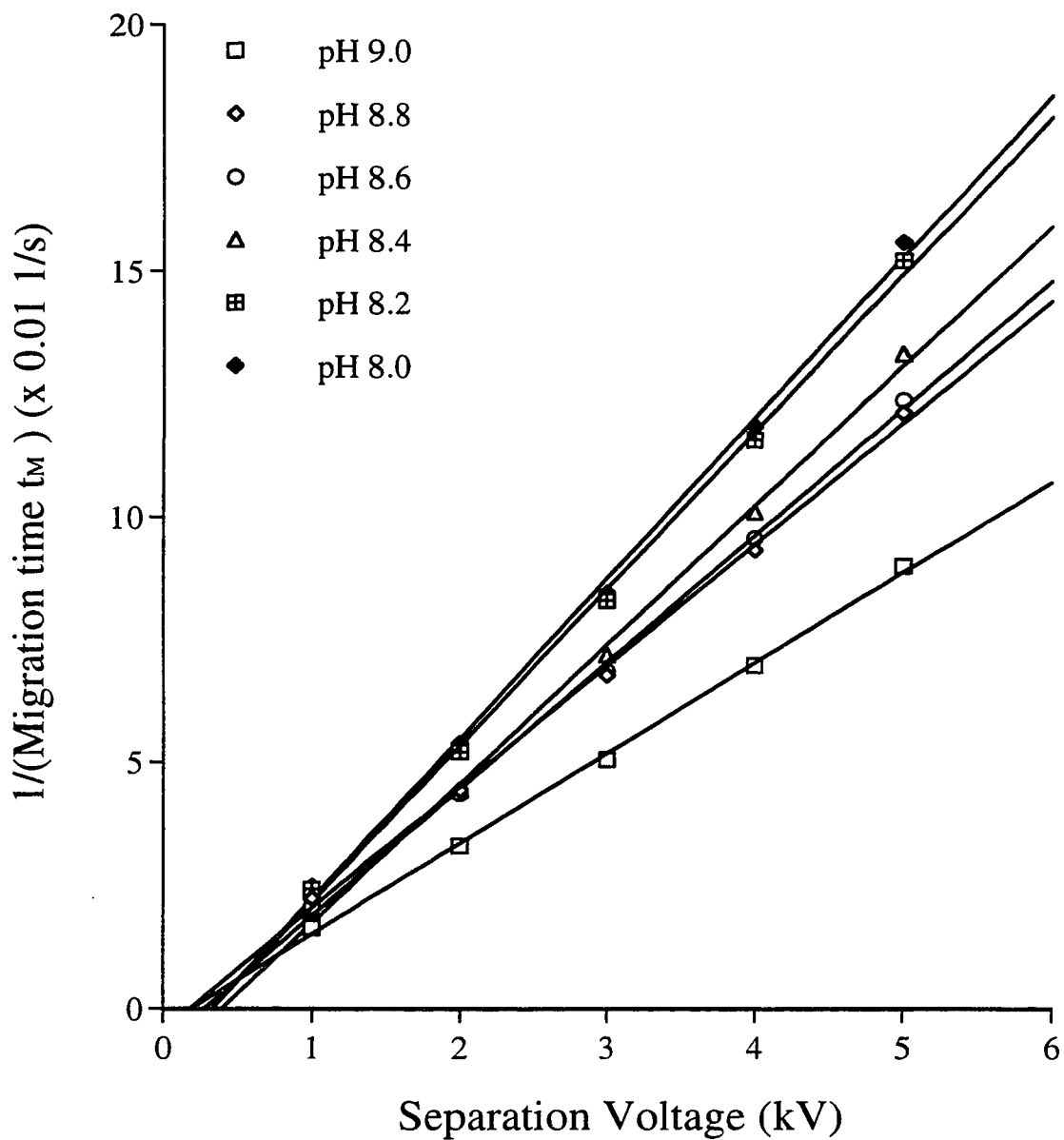


Figure 2-7 Migration time varied with the voltage applied to the main channel. The slope is proportional to the observed mobility, which increased with the decreased buffer pH. (Buffer had the same composition as stated in Figure 2-6, 1 M HCl used to adjust solution pH. The device was made of Pyrex glass)

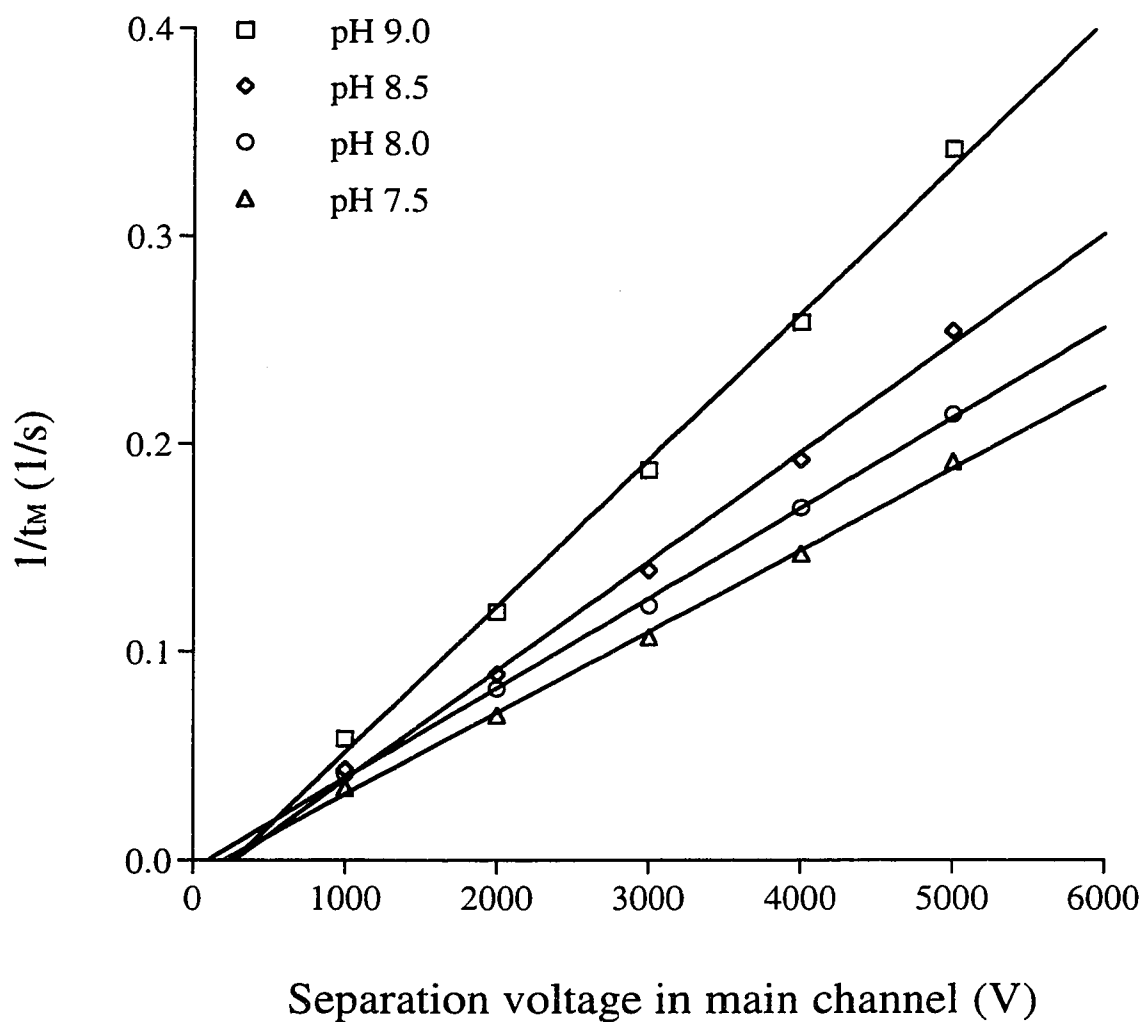


Figure 2-8 Measured overall mobility at different pH--without ionic strength control.

(The buffers were 100 mM Tris and 20 mM Boric acid, 1 M HCl was used to adjust pH)

Figure 2-7 shows that μ_{obs} decreases with increasing pH. Despite the high concentration of buffer relative to KCl, it is well known that tris and boric acid dissociate very weakly in the pH range of 8 to 9, so that 5 mM KCl will dominate the ionic strength. Thus, the effect of a pH change alone is observed in Figure 2-7.

Assuming the electrophoretic mobilities of fluorescein are the same at these pH values for both capillaries and glass chips, we can calculate the electroosmotic mobilities of the buffers with Equation 2-1. Table 2-4 shows the measured μ_{obs} , and the calculated μ_{eo} on-chip obtained from the known values of μ_{ep} in Table 2-3. The results indicate that across this narrow pH range of 8 to 9 there is a weak dependence of μ_{eo} on pH in this Pyrex material. The direction seen is consistent with surface charge increasing with pH.

Table 2-4 Electroosmotic mobility measurements on a Pyrex chip.

pH	$\mu_{\text{obs}} \times 10^{-5}$ (cm ² /V•s)	$\mu_{\text{ep}} \times 10^{-4}$ (cm ² /V•s)	$\mu_{\text{eo}} \times 10^{-4}$ (cm ² /V•s)
9.19	1.84±0.02 ₆	-3.06±0.03 ₂	3.25±0.03 ₂
9.02	2.47±0.04 ₁	-2.77±0.02 ₉	3.03±0.02 ₉
8.83	2.58±0.03 ₉	-2.73±0.02 ₅	2.98±0.02 ₅
8.62	2.84±0.05 ₀	-2.73±0.02 ₃	3.01±0.02 ₃
8.39	3.19±0.05 ₆	-2.69±0.01 ₉	3.01±0.02 ₀
7.97	3.27±0.06 ₁	-2.65±0.01 ₇	2.98±0.01 ₈

2.4.2 Velocity measurement

The velocities of fluid flow from the side and main channels needed to be measured to evaluate the flow behavior. Two methods were used to measure velocity: flow velocity of sample beads provided a direct measurement; while the photo bleaching effect, which leads to velocity dependent fluorescent intensity, could be used to provide an indirect measure of velocity when used with a velocity versus intensity calibration curve.

2.4.2.1 Particle counting

This should be a very simple and obvious way to measure the velocity of the fluid flow. We put some Fluoresbrite Carboxy YG 6 Micron microspheres in the system, in an effort to estimate the bulk fluid flow. These beads are fluorescent at 520 nm wavelength, and will be detectable with the Argon ion laser at 488 nm excitation. These beads are 6.7 μm in diameter according to the manufacturer, and were diluted 250 times from the stock solution supplied commercially with the working buffer when used to monitor the bulk flow.

To calculate the solvent velocity of the flow, we stored the fluorescent beads in the side channel and applied voltages between 200 to 2400 V in 200 V increments from the bead reservoir to the waste. The devices used were made of Pyrex and Borofloat, with the side channel length of 10.0 mm, and the main channel length of 49.0 mm. The

buffer was composed of 20 mM Tris, 4 mM Boric acid, and 5 mM KCl, at pH 9.14. A CCD camera (Sony, Japan) was used to record the particle movement inside the side channel moving towards the intersection. An accurate microscale (Reichert, Carsen Group Inc., ON Canada) was used under the same microscope objective to measure the actual length scale. Knowing the distance the beads traveled and the time taken by an individual bead to move through this length, we can calculate the solvent velocity under different voltages.

Once we obtained the solvent velocity in the channel under various voltages, we put the beads in the side channel and filled the main channel with buffer. We applied voltage to the main channel only and left the side channel floating. Ideally, no beads should “leak” out of the side channel; if there is any leakage of the beads, they should move at the solvent velocity from the side channel.

The measured bead velocities and their overall mobilities under different applied voltages are listed in Table 2-5. Figure 2-9 shows a plot of this same data set. While replicate measurements at each voltage gave an error of $\pm 15\%$, we can see from Table 2-5 that the mobility varied significantly, with an average of $5.95 \pm 39.5\%$. The least square fit looks reasonable, and suggests that a linear relationship between velocity, v and the electric field, E . However, the considerable variation with applied voltage left us concerned that the overall precision of this method would not be high enough. When measuring the leakage flow from the side channel, we found the leakage increased with the solvent velocity in the main channel, as shown in Table 2-6, the velocity of bead was calculated from the calibration curve in Figure 2-9, and the solvent velocity was

Table 2-5 Calibrate the bead velocity under certain applied voltages

Applied Voltage (V)	velocity ($\mu\text{m/s}$)	$\mu_{\text{obs}} \times 10^{-5} (\text{cm}^2/\text{V}\cdot\text{s})$
200	166	8.30
400	353	8.82
600	434	7.24
800	564	7.06
1000	605	6.05
1200	651	5.43
1400	706	5.04
1600	770	4.81
1800	847	4.70
2000	905	4.70
2200	996	4.53
2400	1129	4.70

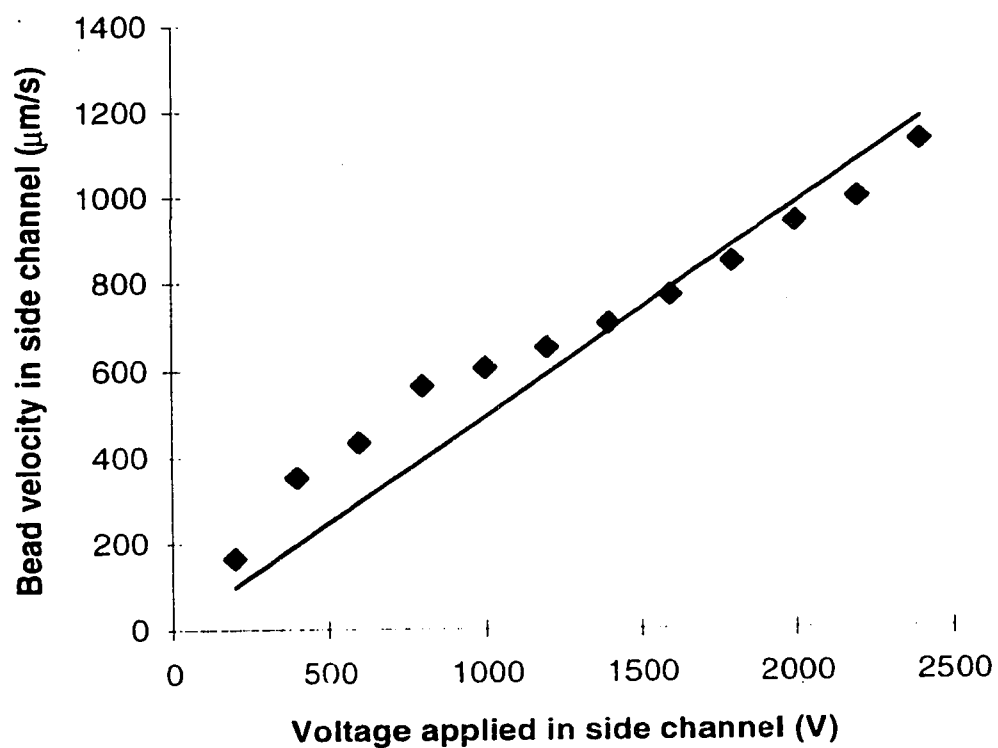


Figure 2-9 Calibration curve for bead velocity with the applied voltage (least square fit). Side channel length was 10.0 mm.

calculated with the electroosmotic mobility of $3.25 \times 10^{-5} \text{ cm}^2/\text{V}\cdot\text{s}$ at pH 9.19 in Table 2-4. This typical electroosmotic mobility value may not be exactly the same in this device, however, it should give a reasonably close μ_{eo} to this measurement. The same data set was plotted in Figure 2-10, showing the linear increase of the leakage bead velocity as a function of the solvent velocity in the main channel. Qualitatively, this measurement agrees well with our prediction with the model, which will be discussed with Figure 2-12. Practically however, it is time consuming to count all the beads under the different voltage conditions, and the precision is not satisfactory. This could be caused by the non uniformity of the bead size, which were visible on the video tape recorded by the CCD camera, or possibly the bead charge, and the bead-wall interactions.

Table 2-6 Bead velocity in the side channel due to main stream flow

Voltage applied to main channel (V)	Solvent velocity in main channel ($\mu\text{m/s}$)	Bead velocity in side channel ($\mu\text{m/s}$)
1000	677	385
2000	1354	847
3000	2031	1129
4000	2708	1209
7000	4740	2117

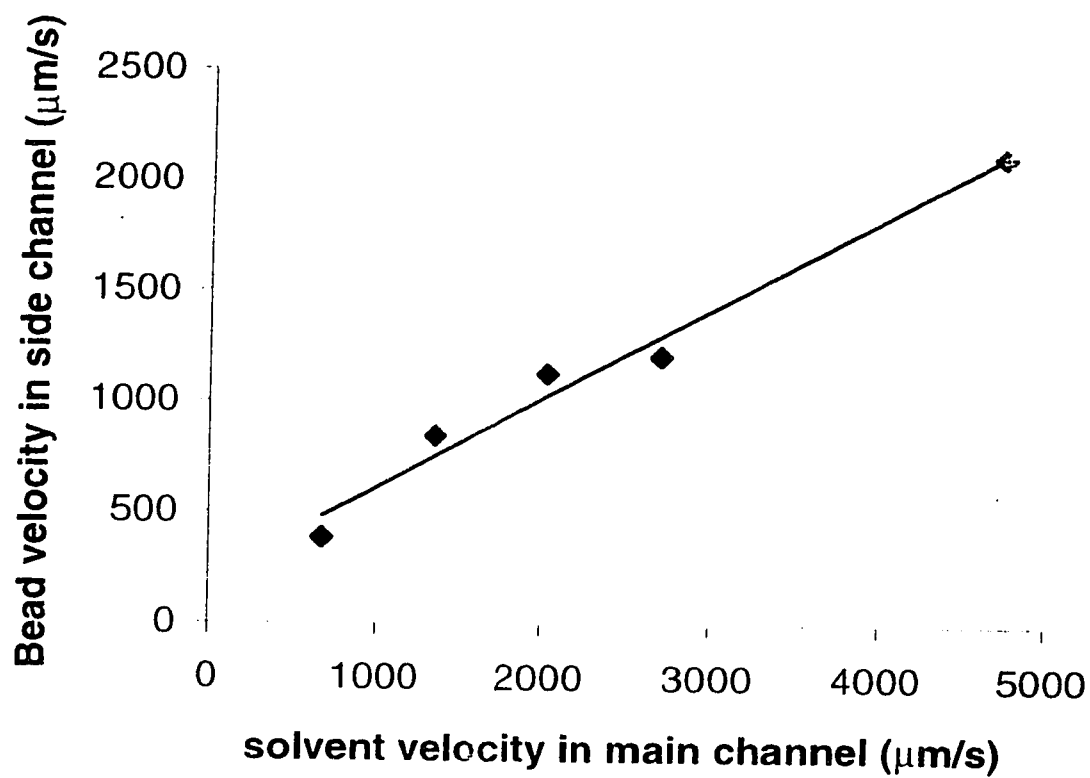


Figure 2-10 Bead leakage velocity from the side channel due to the potential applied to the main channel (least square fit).

2.4.2.2 Fluorescein-based velocity calibration curve

In this method, we used a fluorescein solution as the dye sample detected by laser induced fluorescence. We placed dye in the side channel reservoir, the sample reservoir, and applied voltage from there to the waste in order to make a calibration curve. Figure 2-11 is a representative calibration curve showing the relation of the fluorescence intensity to the dye flow velocity (2). The dye sample is driven directly from the side channel sample reservoir to the main channel waste. The channel length is known, as is the voltage applied to the system. The flow velocity can be calculated from Equation 2-4:

$$v = \mu E = \mu \frac{V}{L} \quad 2-4$$

where v is the dye velocity due to electroosmotic and electrophoretic mobility of the flow, μ is the total observed mobility, V is the voltage applied to the system, and L is the channel length. The value of m was independently measured for each device and each calibration curve. The intensity at each applied V can then be corrected to the observed velocity.

To measure the total observed dye mobility in a chip, a series of separations of fluorescein were performed under different separation voltages, as discussed in section 2.4.1.2. The result of mobility measurements was shown in Figure 2-7. The dye velocity of the solution is proportional to the voltage applied to drive the flow (2). With high laser intensity photobleaching occurs, and the surviving fluorescein concentration becomes a function of the dye velocity. The intensity increases as the velocity does, up

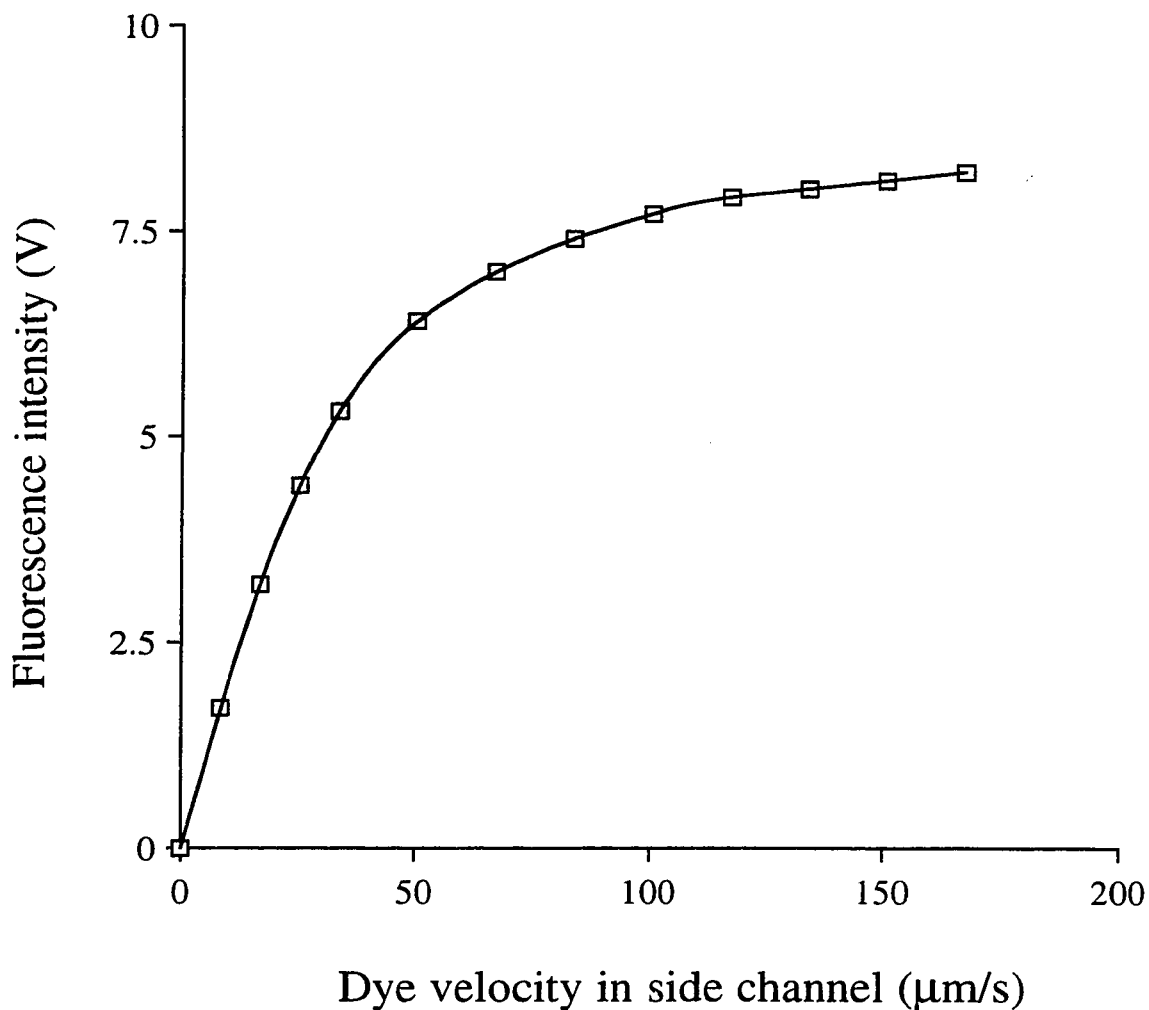


Figure 2-11 Calibration curve showing fluorescent intensity vs. dye velocity, when dye in the side channel was directly driven to the waste. Curve drawn is for clarity only. Main channel length was 49.0 mm, side channel length was 10.0 mm, symmetric design in 0211 glass. Voltage applied from the dye reservoir to separation waste was in the range of 0--1000 V, with 100 V increments. At pH 9.19, the μ_{ob} was 5.88×10^{-5} , and μ_{eo} was 3.27×10^{-4} (cm²/V•s).

to a plateau value, so that the measured fluorescent intensity is an indicator of the dye velocity.

When there is a high dye flow rate, there is a high fluorescent intensity. Once we obtain the calibration curve showing the relationship of the fluorescent intensity with the dye flow rate, we can measure the intensity from the leakage flow and determine the corresponding dye velocity. In the following work, a new calibration curve was measured for each leakage study and velocity measurement.

The side channel leakage velocity needed to be in a range on the calibration curves where signal varied strongly with velocity, rather than near the plateau. This condition is achieved by varying the laser intensity between 2-5 mW. Alternatively, during leakage studies the main channel voltage range was adjusted to insure the leakage intensity was in the strongly varying region of the calibration curve.

2.4.3 Leakage from floating side channel

It has been shown that there will be solution leakage from the side channel when the potential of the side channel is left floating and a voltage is applied to the main channel to cause a flow (3-6). Hu performed a quantitative study of the leakage, mathematically modeling the electrokinetic flow in simple T-shaped capillary channels (28,30,35). The theory showed that the leakage flow from the side channel when it is floating is described by hydrodynamic effects, i.e. a pressure gradient. The model shows, as seen in Figure 2-12, that the leakage from the side channel decreases with increasing side channel length while the main channel length is kept constant. This arises since the

longer the side channel is, the greater the resistance to fluid flow, and the pressure at the intersection region does not vary much with an increase in side channel length. Therefore, the pressure difference between the side reservoir and the intersection will change little. However, the driving force, or the pressure gradient, will decrease significantly, which results in a leakage decrease with side channel length. In this work, a series of experiments was performed to measure the leakage from the side channel when positive voltage was applied to the buffer channel, waste was held at ground, and the side channel, which was filled with dye, was left floating. The pH and ionic strength of both the buffer and dye solutions were identical, so that the electroosmotic mobility should be a constant in all the channels. In this study the side channel was located in the center of the main channel, and the effect of different side channel lengths was compared. The velocity of the dye solution in the side channel upstream of the “T” intersection was monitored by the intensity dependence of the dye on fluid velocity. The solvent velocity was calculated from the solvent electroosmotic mobility and the electric field applied to the main channel. The electroosmotic mobility can be calculated once we know the total observed mobility and the electrophoretic mobility, which was measured as described in section 2.4.1.1.

The measured dye velocity in the side channel versus the solvent velocity in the main channel is shown in Figure 2-13, with differing side channel lengths of 10, 20, and 40 mm for devices #2, #3 and #4. From the plot we can see that when the voltage, and so the solvent velocity in the main channel increases, the dye velocity in the side channel increases, even though there is no applied electric field there. This is

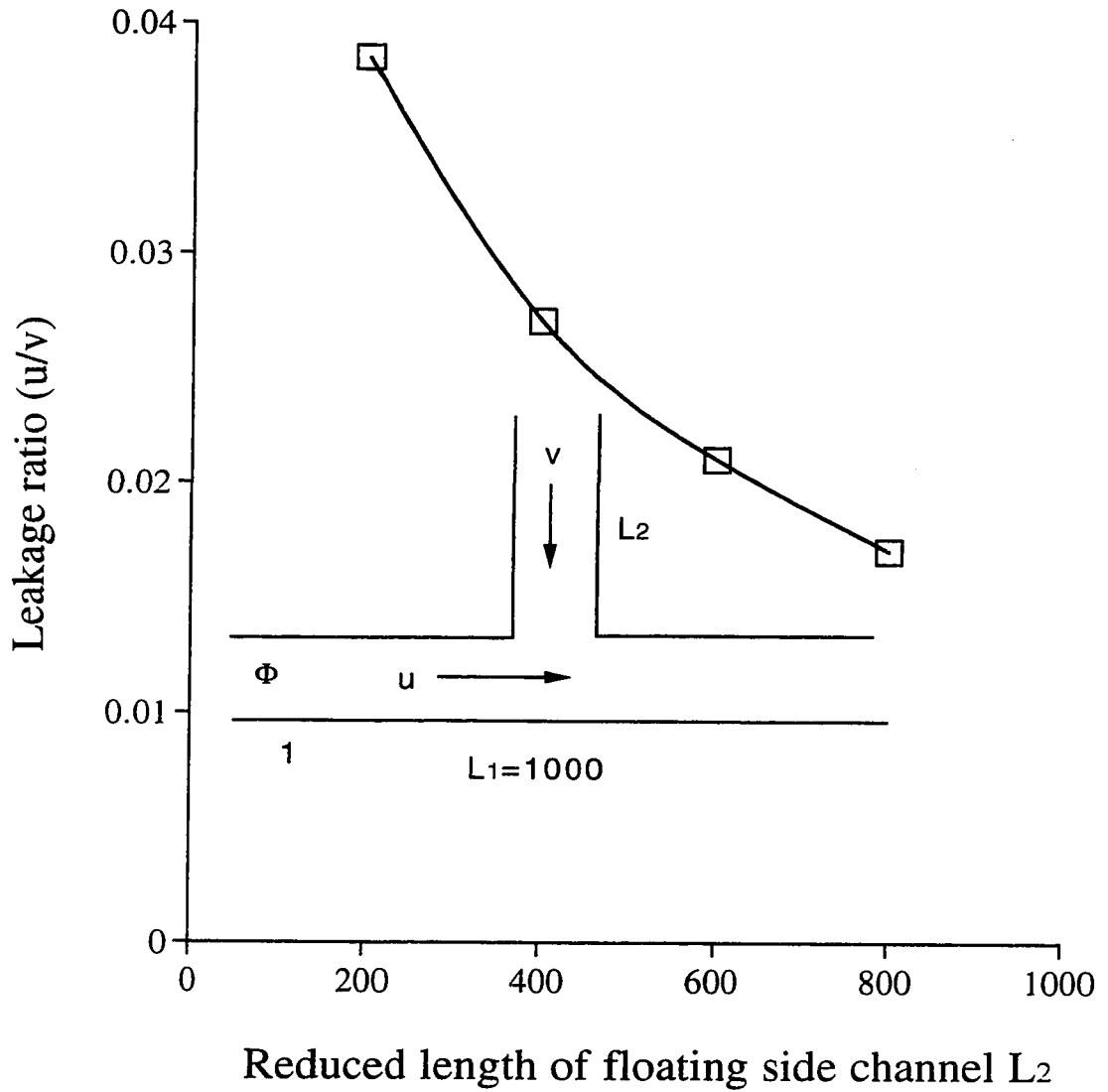


Figure 2-12 (a) Calculated leakage ratio of solvent velocity in the side channel to velocity in the main channel showing the dye leakage from the side channel decreases with increasing side channel length. (b) The reduced length is the channel length divided by half of the channel width. (c) The reduced potential is given by $V_{ap}/25$ mV. (d) The side channel was floating, the left side of the main channel had a reduced potential Φ_1 of 10,000 applied and the other side was grounded. (Adapted from Hu, Ref. 30)

due to the phenomenon we usually call leakage. The calibration curve was obtained at pH 9.2 in each device, with 100-1000 V applied between the side channel and the waste reservoir. Overall mobilities of 4.55×10^{-5} , 5.88×10^{-5} , and $3.27 \times 10^{-5} \text{ cm}^2/\text{V}\cdot\text{s}$ were obtained in each device, giving 3.52×10^{-4} , 3.65×10^{-4} , and $3.39 \times 10^{-4} \text{ cm}^2/\text{V}\cdot\text{s}$ for μ_{eo} in device #2, #3, and #4 respectively. Leakage studies were performed with 1000 to 7000 V applied from main channel to waste reservoir, with a floating side channel. All the buffers used were composed of 20 mM Tris, 4 mM boric acid, and 5 mM KCl controlling the ionic strength. All these devices were made of 0211 glass.

Comparing the three sets of data with different side channel lengths, we found that when the side channel length increased, the leakage decreased. This result is in agreement with the theoretical predictions and makes sense, since the leakage from a side channel should depend on the flow resistance of the side channel. While flow resistance scales linearly with length, the resultant leakage does not, due to the effect of the leakage flow itself on the flow in the main channel. The relative leakage values were calculated to range from 1.7% to 4% for the side channel lengths in Figure 2-12. This trend of decreasing leakage with increasing length is also observed experimentally, as shown in Figure 2-13. For the shortest side channel measured, a leakage of 2% was observed, similar to the 1.8% value predicted in Figure 2-12 for the longest side channel length calculated. (The 1 cm long, 30 μm wide channel used experimentally corresponds to the reduced length of 667.) Practically, it was difficult to carry out experimental work with shorter side channels, while for the simulations the longer side

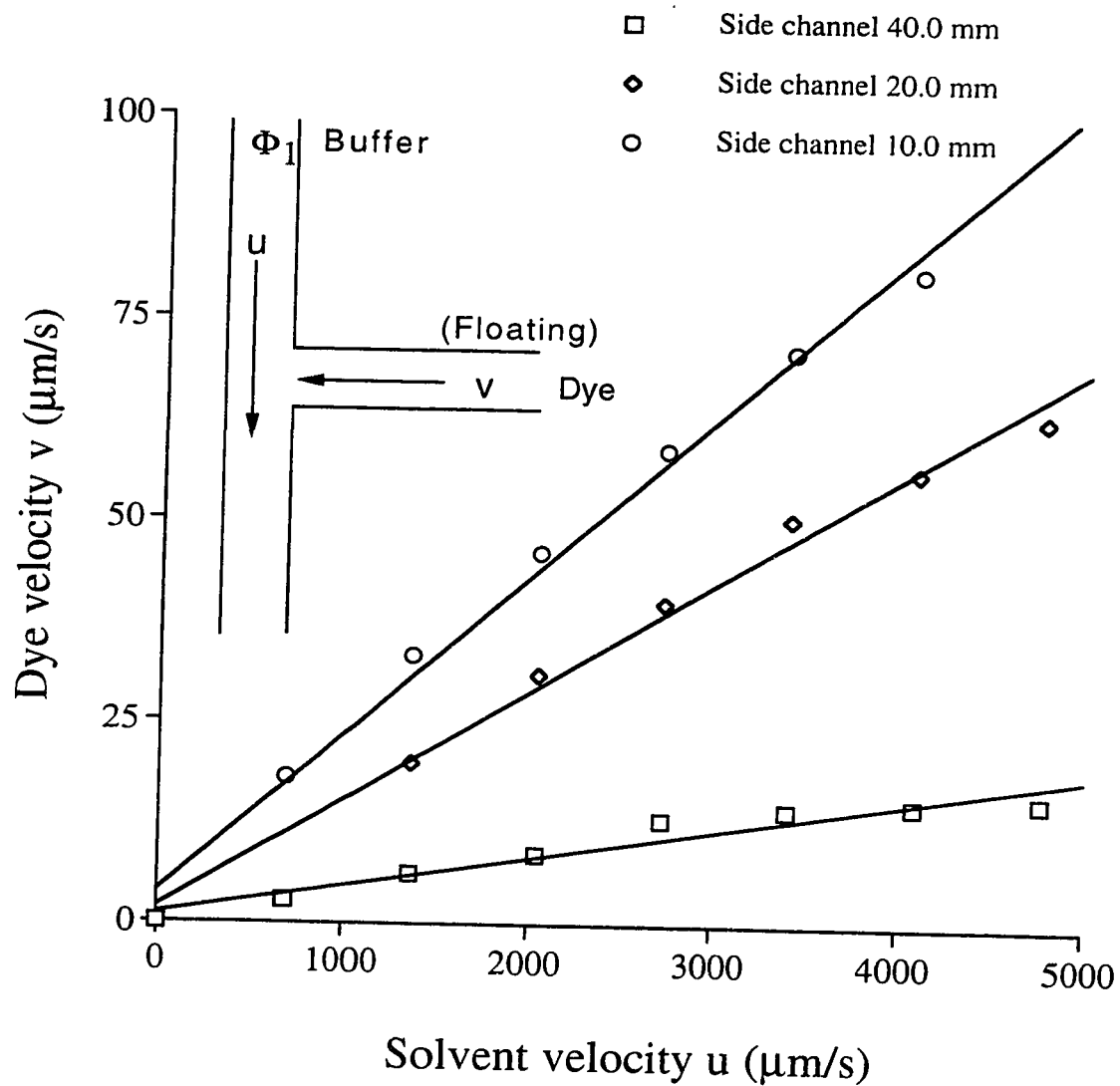


Figure 2-13 Leakage dye velocity from the side channel as a function of the solvent velocity in the main channel. Three sets of data showing the dye leakage in the side channel is channel length dependent.

channels demanded too much computational power. However, for the comparable side channel lengths, the calculated and experimental leakages are very similar, providing confidence in the predictive power of the theory.

2.4.4 Calculations of potential and flow for a potential controlled side channel

It is possible to control the flow of the intersecting channels by applying potentials to all of the reservoirs from which the channels initiate. From the schematic diagram shown in Figure 2-14, we can calculate the junction voltage at the intersection, V_J . With potentials applied to the solvent reservoirs of all three channels, these three intersecting channels can be modeled as a simple network of three resistors (5). We assign the voltages applied to the reservoirs 1 & 2 as V_1 (main channel) & V_2 (side channel), with each reservoir containing the chemicals to be mixed. We apply a ground voltage (V_3) to reservoir 3, which is the mixing waste, and we name the voltage at the intersection of the three channels as junction voltage, V_J . We can convert the known length of each channel to a relative resistance R , which is proportional to the length when the cross sectional area of the channel remains the same. Using Kirchhoff's rules (36) and solving for V_J , we come to Equation [2-5] (3):

$$V_J = \frac{V_1 R_2 R_3 + V_2 R_1 R_3}{R_1 R_2 + R_2 R_3 + R_1 R_3} \quad 2-5$$

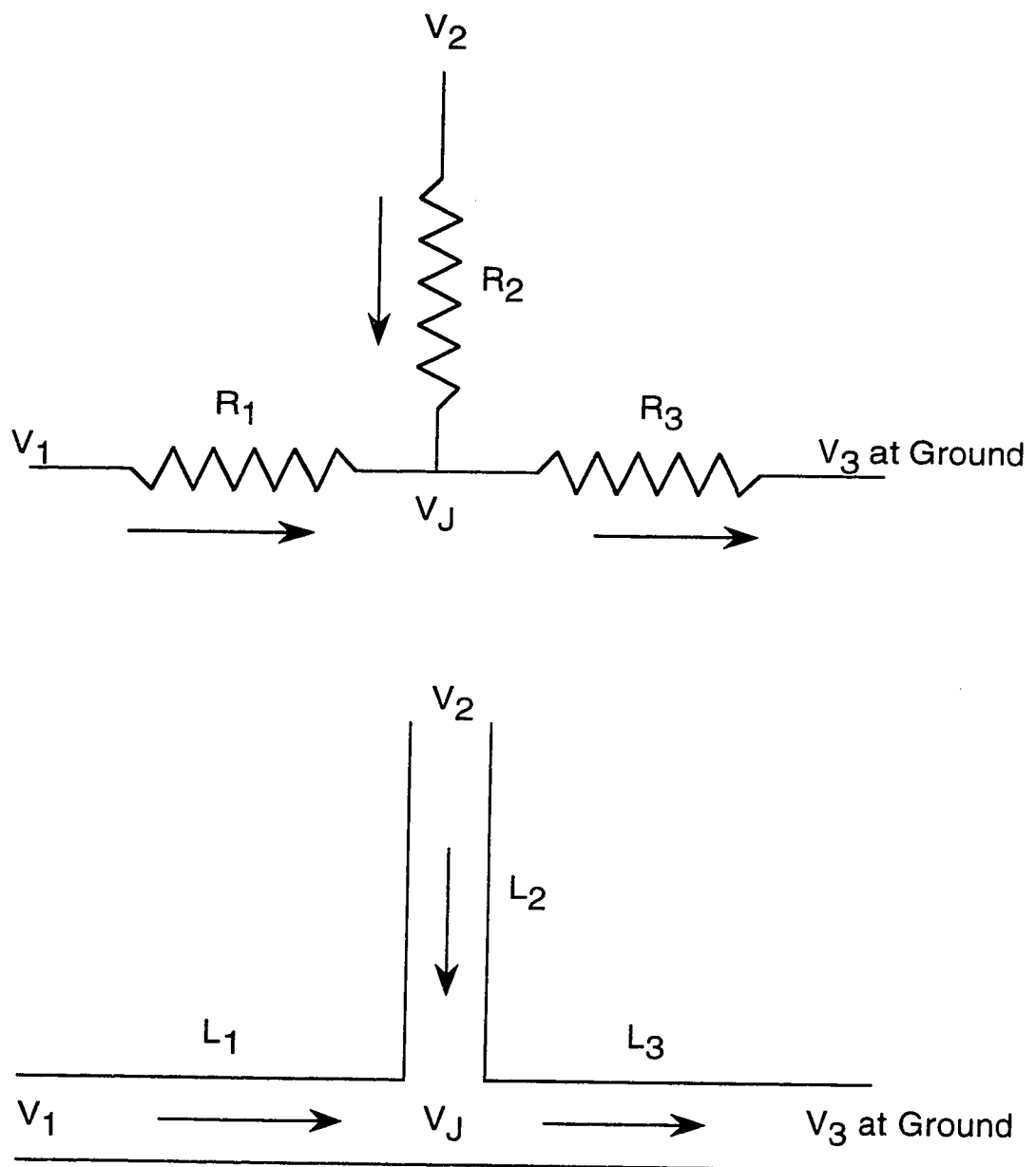


Figure 2-14 Schematic diagram showing the relationship of junction voltage and resistance to the relevant channels.

Knowing the junction voltage value, we can apply a voltage to one of the channels to make it the same magnitude as the junction voltage, in order to stop the flow from that channel. This is an effective method to control the leakage flow. We need to control the leakage flow from the sample channel when we run a separation, otherwise the background from the leakage can lead to poor detection limits and poor sample plug definition. The following sections examine the ability to control leakage in a predictable fashion and the importance of the electroosmotic flow rates in each channel to this control.

The null condition most easily observed is the case where the dye stops moving, but this is not the same condition as zero solvent flow. The development below is meant to clarify the meaning of the null flow experiment. We can write the following two expressions for dye and solvent velocities, respectively:

$$v_{dye} = v_{eo} + v_{ep} + A \frac{\Delta P}{l^2}$$

$$v_{sol} = v_{eo} + A \frac{\Delta P}{l^2}$$

where the “Poiseuille” or pressure driven flow velocity in the side channel is proportional to $\Delta P/l^2$, where ΔP is the pressure drop along the side channel to the intersection, l is the side channel length, and A is the proportionality constant. (Note that v_{eo} and v_{ep} are in the opposite direction for fluorescein at pH 8-9.) At the null condition v_{dye} is zero so that

$$v_{ep} = -v_{sol}$$

This expression may be rewritten as

$$\mu_{eo} \frac{\Delta V}{l} + \frac{A \Delta P}{l^2} = -\mu_{ep} \frac{\Delta V}{l}$$

where ΔV is the potential drop along the side channel. Rearrangement gives:

$$A \frac{\Delta P}{l^2} = (\mu_{ep} + \mu_{eo}) \frac{\Delta V}{l} = \mu_{obs} \frac{\Delta V}{l} \quad \text{when } v_{dye} = 0$$

Thus, the null potential condition provides a direct measure of the magnitude of flow induced by the leakage effect for a specified flow condition in the main channel.

2.4.5 Side channel length effect

The model, as indicated in Figure 2-12, shows that the leakage from the side channel decreases with increasing side channel length while the main channel length is kept constant. This means that the longer the side channel is, the greater the resistance to fluid flow. The pressure at the intersection region does not vary much with an increase in the length of the side channel. Therefore, the pressure difference between the side reservoir and the intersection will change little. However, the driving force, or the pressure gradient, will decrease significantly, which results in the leakage decreasing with increasing side channel length.

The predictions of the model regarding leakage were evaluated using a null flow study, in which we determined the voltage needed to stop side channel flow. As mentioned before, when we apply voltage to the main channel and leave the side channel floating, theoretically, there should be no flow leaking out of or into the side channel. In the following sections, we distinguish the flow directions in the side

channel as “leakage flow” and “pushback flow”. If there would be a flow leaking out from the side channel when it is floating, we refer to it as “leakage flow”; if the flow would be entering the side channel from the main stream when the side channel is floating, we refer to it as “pushback flow”. A series of increasing potentials was applied to the side channel to evaluate the leakage from there. In the absence of leakage effects the voltage required on the side channel to prevent flow is equal to V_J , where V_J is the junction voltage which can be estimated from calculation using Equation 2-5. The actual potential drop required to stop flow in the side channel is referred to as V_{stop} , where $V_{stop} = V_2 - V_J$. The calculated perturbation at the intersection results from the pressure difference between the intersection and the side channel end, and it is this pressure difference that needs to be balanced by the electrical force to obtain zero leakage. By measuring the offset value of V_{stop} , we can evaluate the extent of leakage. When $V_{stop} > 0$, the buffer would have been pushed back into the side channel when the side channel was left floating, so we need an electric force directed out of the side channel to stop the flow from the intersection to the side channel; we refer to this situation as a pushback flow. When $V_{stop} < 0$ dye would have leaked out from the side channel when the side channel was floating, so we need an electrical force into the side channel to stop the flow from the side channel to the intersection; comparing to the case with no leakage we refer to this situation as a leakage flow.

2.4.5.1 Side channels located 10.0 mm from the inlet of the main channels

This experiment was performed with varying side channel lengths where all these side channels were located 10.0 mm from the inlet of the main channels, whose lengths were 48.0 mm. The calibration curve was obtained at pH 9.19 in each device, with 100-1000 V applied between the side channel and the waste reservoir. Overall mobilities of 4.99×10^{-5} , 5.90×10^{-5} , and $7.90 \times 10^{-5} \text{ cm}^2/\text{V}\cdot\text{s}$ were obtained in each device, giving 3.56×10^{-4} , 3.65×10^{-4} , and $3.85 \times 10^{-4} \text{ cm}^2/\text{V}\cdot\text{s}$ for μ_{eo} in device #2, #3, and #4 respectively. The null flow experiments were performed with the side channel potential at 1000 V, and main channel potentials varied from 1000 to 2200 V. All the buffers used were composed of 20 mM Tris, 4 mM boric acid, and 5 mM KCl controlling the ionic strength. All these devices were made of 0211 glass.

The results are shown in Figure 2-15, plotted as dye velocities from the side channels, v_2 , as a function of the electric field in the side channel, V_{stop}/L_2 . For the shorter side channel length, 10.0 mm, V_{stop} has a negative value at the null velocity for the side channel flow. This means that we need some extra electric force to stop the leakage flow from the side channel. Put another way, we can see that for the 10.0 mm side channel dye velocity has a positive value at the value of V_{stop} where theoretically there should be no flow. For the longer side channel length, 40.0 mm, V_{stop} has a positive value at the null dye velocity for the side channel flow, which means that we need less electric force than calculated to stop the leakage flow from the side channel. Looked at the other way, we find that dye velocity has a negative value at the V_{stop} where theoretically there should be no flow, which indicates that the flow pushes into the side channel. For the side channel length of 20.0 mm, V_{stop} is zero at the null

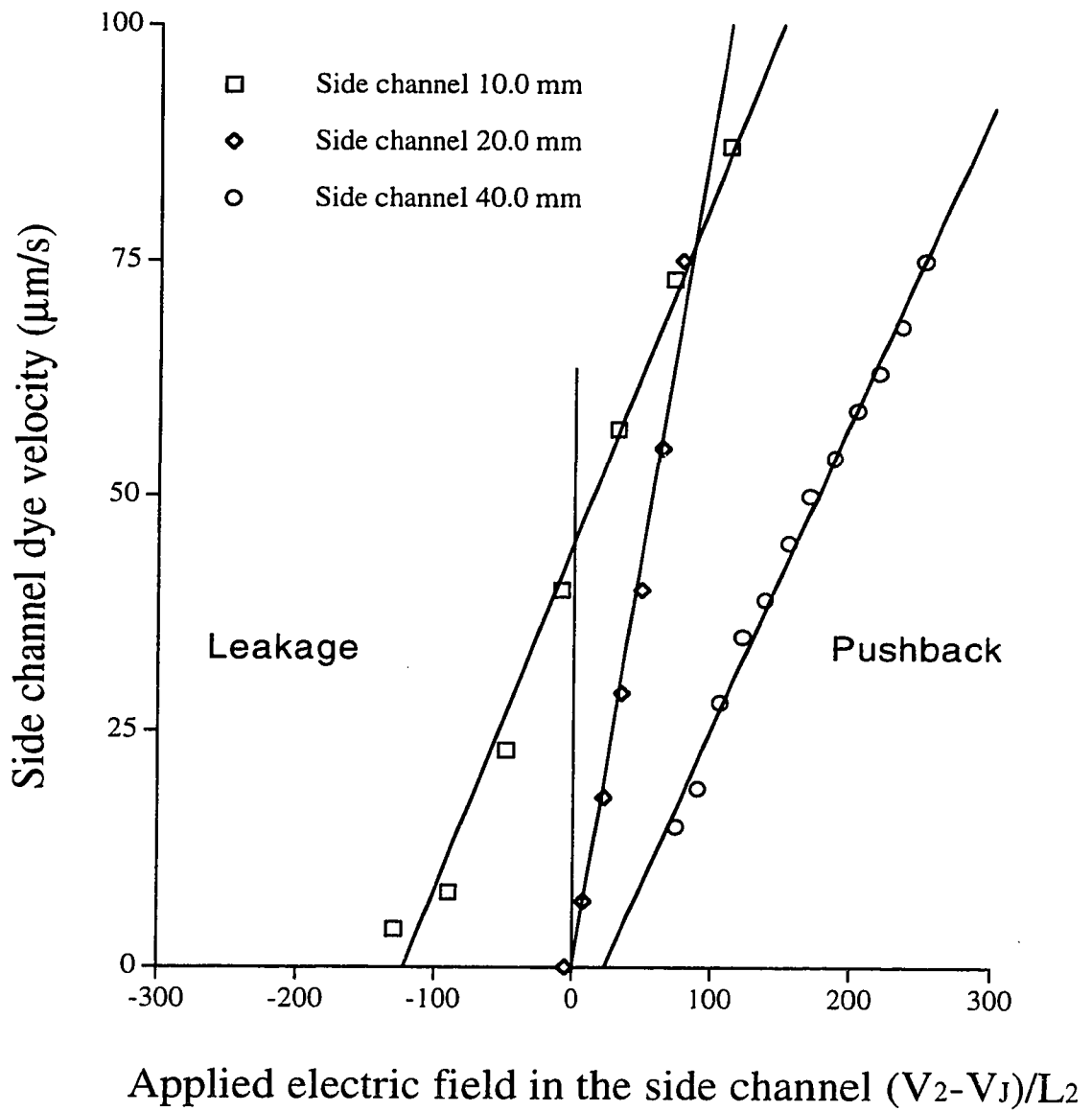


Figure 2-15 Flow velocity in the side channel as a function of the electric field. Flow direction in the side channel changed from leakage flow to pushback flow as the side channel length increased. (Side channel located 10.0 mm from main channel entrance)

velocity for the side channel flow, which indicates that the flow behavior in this design is exactly what the model predicts, no leakage or pushback, and is the perfect case.

From the measurements, we conclude that the short side channel leaks more than the long side channel, which we believe correlates well with the estimation from the resistance consideration: the longer the channel, the higher the resistance. When the side channel gets longer, there would be more resistance for dye to move into the intersection, so we observed less leakage. These results are consistent with the model. However, the results for the longest side channel, 40 mm, are inconsistent with a simple interpretation of the model. Pushback is predicted by the model only when the ζ potential in the main channel is much lower than in the side channel, yet there is no particular reason to expect that this is true here. We have no explanation for this discrepancy at present. This study was performed on 5 different devices, and the same result was obtained 4 times.

2.4.5.2 Side channels locate at the center of the main channels

This experiment was done with different side channel length of 5.0, 10.0, 20.0, and 40.0 mm, and all the side channels were located at the center of the main channel, which is 24.0 mm from either end of the main channel. The calibration curve was obtained at pH 9.19 in each device, with 100-1000 V applied between the side channel and the waste reservoir. Overall mobilities of 4.48×10^{-5} , 4.99×10^{-5} , 5.90×10^{-5} , and $7.90 \times 10^{-5} \text{ cm}^2/\text{V}\cdot\text{s}$ were obtained in each device, giving 3.51×10^{-5} , 3.56×10^{-4} , 3.65×10^{-4} , and $3.85 \times 10^{-4} \text{ cm}^2/\text{V}\cdot\text{s}$ for μ_{eo} in device #1, #2, #3, and #4 respectively. The null

flow experiments were performed with the side channel potential applied at 1000 V, and main channel potentials varied from 1000 to 2200 V. All the buffers used were composed of 20 mM Tris, 4 mM boric acid, and 5 mM KCl controlling the ionic strength. All these devices were made of 0211 glass.

The results are shown in Figure 2-16, plotted as dye velocity, v_2 , in the side channel as function of the electric field applied in the side channel, V_{stop}/L_2 . From the plot, we observe that the side channel with the length of 10.0 mm has a positive V_{stop} value of 80 V at the null velocity for the side channel flow, indicating a pushback flow at the predicted null. Side channel with a length of 5.0 mm has a small negative V_{stop} of 50 V at the null velocity for the side channel flow, indicating a small leakage flow at the predicted null. For the other two side channel lengths, 20.0 and 40.0 mm, V_{stop} is close to 0 V at the null velocity for the side channel flow, indicating proper flow behavior as the theoretical prediction. Three different devices were used, and similar results were obtained three times from each device.

2.4.5.3 Side channels locate at the 38.0 mm from the inlet of the main channels

In this study, we used side channels with different lengths of 5.0, 10.0, 20.0, and 40.0 located at 38.0 mm from the inlet of the main channel, whose length is the same as above, 49.0 mm. The calibration curve was obtained at pH 9.19 in each device, with 100-1000 V applied between the side channel and the waste reservoir. Overall mobilities of 4.48×10^{-5} , 4.99×10^{-5} , 5.90×10^{-5} , and $7.90 \times 10^{-5} \text{ cm}^2/\text{V}\cdot\text{s}$ were obtained

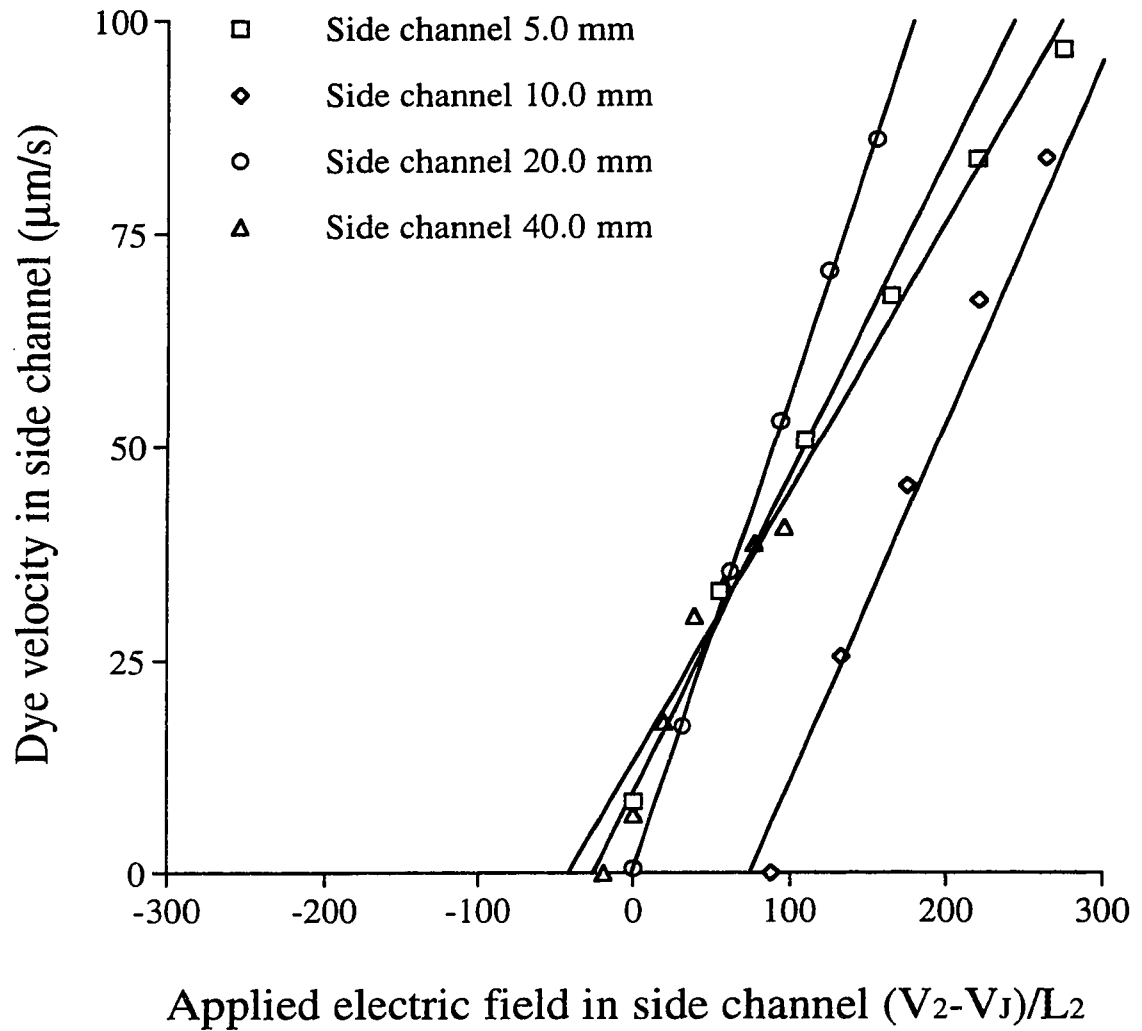


Figure 2-16 Flow velocity in the side channel as a function of the applied electric field there. Flow velocity in the side channel is close to the predicted null. (Side channels were located at the center of the main channel)

in each device, giving 3.51×10^{-5} , 3.56×10^{-4} , 3.65×10^{-4} , and $3.85 \times 10^{-4} \text{ cm}^2/\text{V}\cdot\text{s}$ for μ_{eo} in device #1, #2, #3, and #4 respectively. The null flow experiments were performed with the side channel potential applied at 1000 V, and main channel potentials varied from 1000 to 2200 V. All the buffers used were composed of 20 mM Tris, 4 mM boric acid, and 5 mM KCl controlling the ionic strength. All these devices were made of 0211 glass.

The results are plotted in Figure 2-17, showing dye velocities in the side channel, v_2 , change with the side channel electric field, V_{stop}/L_2 . From the plot, we can see that, for the shortest side channel, 5.0 mm, we needed extra voltage to stop the flow in the side channel. The V_{stop} needed was around -150 V/cm smaller than the electrokinetically predicted null value, which indicates that there would be a strong flow leaking out of the side channel at the predicted null. When the side channel was 20.0 mm long the V_{stop} value was very close to zero. This result indicates that the flow was balanced: no flow leaked out or pushed into the 20 mm long side channel. For the longest side channel, there was a small negative V_{stop} value, which indicated there might be some leakage. This contrasts with the pushback flow seen in the previous study with the side channels located close to the inlet. The second shortest side channel, 10.0 mm, gave a positive value for V_{stop} , which meant that there was a flow pushed into the side channel so that we needed less voltage than the calculated junction voltage to stop the dye flow at the intersection. This result is also the opposite of the previous study with the side channel closest to the inlet. Three different devices were used for this study, and similar data was collected 3 times from each device.

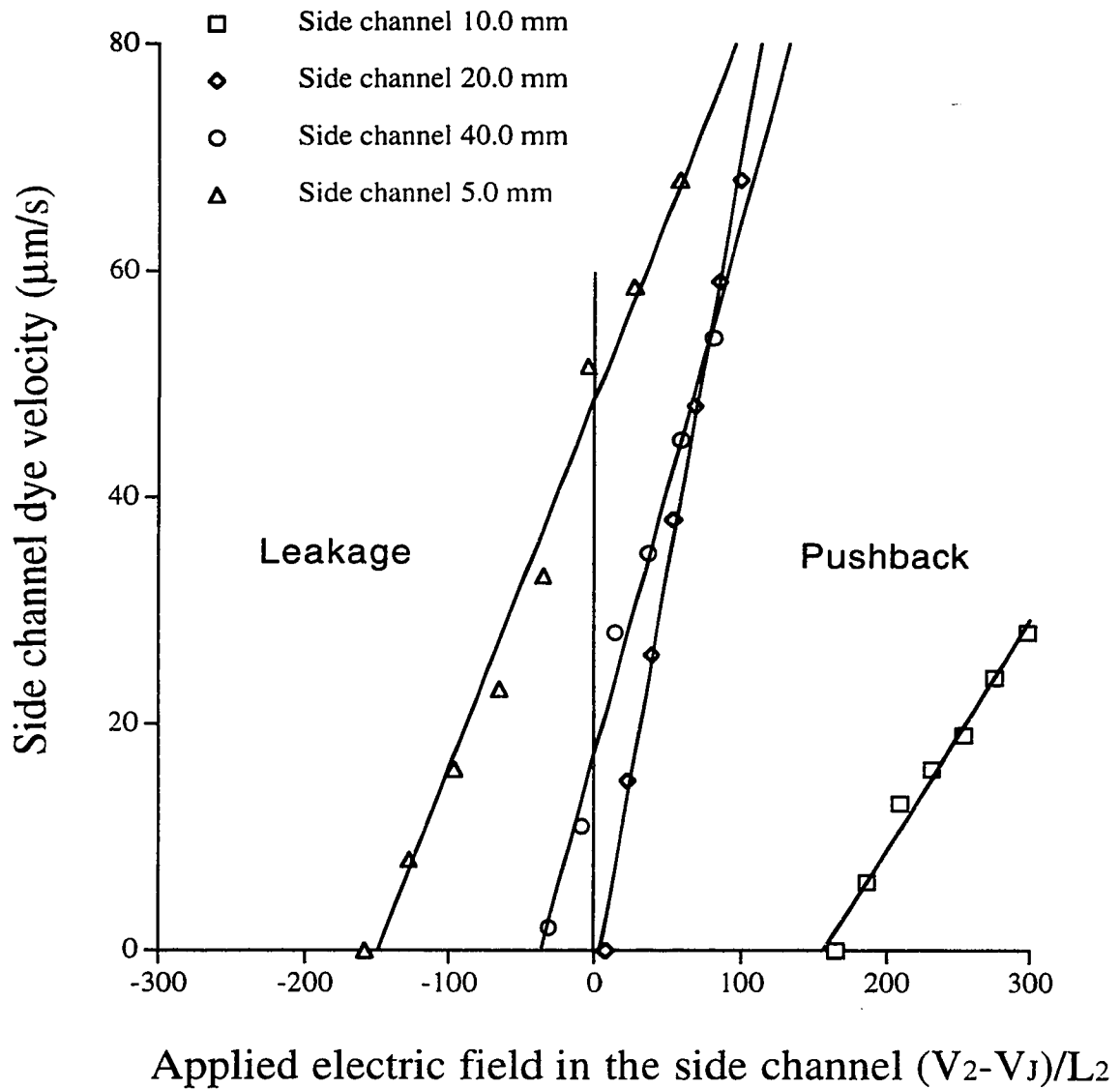


Figure 2-17 Flow velocity in the side channel as a function of the applied electric field there. Flow direction in the side channel changed from pushback flow to leakage flow as the side channel length increased. (Side channels were at 38.0 mm from the main channel entrance)

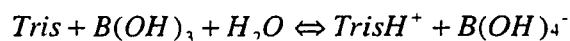
From the model, the pressure drop along the side channel is much smaller when it is close to the exit reservoir on the main channel. This does not completely explain the trends we observed, especially for the 10.0 mm side channel. However, since the forces are small, it may be possible that other forces or unknown effects can play a more significant role.

W. Parce (37) has suggested that pH shifts in the reservoir electrolyte due to electrolysis could possibly be playing a role in these observations. At the cathodes, electrolysis consumes H^+ and raises the pH. If the buffer capacity is exceeded, OH^- ions will be present and could migrate upstream into the channels. This would create changes in ζ potential that would increase the solvent velocity along the main channel. Additional pressure driven flow can be expected due to this ζ potential imbalance, which leads to a complex flow profile. Similarly, at the anode excess H^+ will be generated that will reduce ζ if it exceeds the buffer capacity.

Knowing the current generated in the experiments, and the time needed to finish each pH study, we can calculate the number of moles of electrons generated at the cathode or anode. With the known volumes of the reservoirs, proton or hydroxide produced can be calculated, therefore the approximate pH shift is available through a series of calculations. From our calculation, however, the pH shifts were small; in most of the case, the pH shifts were no more than 0.02 unit. The details of the calculated results are listed in Table 2-7. The first column shows the current generated during high voltage application of 4 kV, which in our case were typically between 1.2 to 3.2 μA . The second column is the total time that a given reservoir buffer solution with a certain

pH value undergoes the whole measurement, before exchanging it. The calculated micro-Coulombs passed, which is proportional to the current and the time during the electrolysis, is listed in column 3. Using the Faraday constant, we can obtain the equivalent number of moles of electrons generated in the buffer waste reservoir as column 5, which can then be used to obtain the amount of OH⁻ made from electrolysis in column 6. Our reservoirs held a total solvent volume of 80 μL. The buffer was usually Tris/Boric acid, pH 9.19. The equilibrium constant for the reaction below was calculated with using the acid dissociation constants (38), to give 0.08. At the equilibrium, the conjugate acid for protonated Tris, and the number of moles of the conjugated base from boric acid, can be assigned as “x”. The concentrations of each component can be calculated as follows (38).

a. When there is no electrolysis:



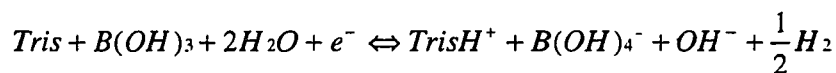
Initial (mM) 20 5

Final (mM) 20-x 5-x x x

At the equilibrium, we have $\frac{(x)(x)}{(20-x)(5-x)} = K = 0.080$

where K is the equilibrium constant for the reaction above. It is determined from the individual K_a values for both weak acids.

b. When there is electrolysis (taking the case shown in the 2nd row in Table 2-7):



Initial (mM) 20 5 0.140

Electrolysis	20	5-0.140		0.140
Final (mM)	20-x	5-0.140-x	x	0.140+x

At the equilibrium, we have
$$\frac{(x)(0.140 + x)}{(20 - x)(5 - 0.140 - x)} = K = 0.08$$

We solved these problems by using the quadratic formula.

The values of x are shown in the column labeled “ x (mM)”, which are the amounts of TrisH^+ and B(OH)_2^- formed as a result of the different electrolysis conditions. The resulting pH values are listed as the last column in Table 2-7, which are calculated from the Henderson-Hasselbalch Equation (38):

$$\text{pH} = \text{p}K_a + \log \frac{[\text{Tris}]}{[\text{TrisH}^+]} = 8.15 + \log \frac{[\text{Tris}]}{[\text{TrisH}^+]}$$

Table 2-7 pH shifts due to electrolysis in waste reservoir (The first row shows the result without electrolysis).

I (μA)	t (min)	Q ($\mu\text{-Coul}$)	$n_e \times 10^{-8}$ (mol)	Vol (μL)	OH^- (mM)	x (mM)	pH
	0			80		1.495	9.24
1.2	15	1080	1.12	80	0.140	1.468	9.25
2.8	15	2520	2.61	80	0.326	1.433	9.26
3.2	15	2880	2.98	80	0.373	1.424	9.26

Similarly, we can calculate the H^+ generated in the anode, which gave no more than a 0.02 pH shift towards acidic conditions.

2.4.6 Fixed side channel length and varying the intersection positions

As illustrated in the previous section, leakage flow from the side channel is due to hydrodynamic effects, i.e. the pressure gradient. When the side channel intersects the main channel at different positions, the flow will be different as the pressure varies with position along the main channel. The entrance effect on the electroosmotic flow obtained from the model shows that the pressure profile along the centerline of the channel undergoes a sharp drop at the entrance mouth (28,30). The pressure then gradually recovers to the outlet value, which is the same as the inlet pressure. As the pressure difference between the intersection point and the inlet of the side channel decreases when the intersecting point is further away from the inlet, one can predict less leakage from the side channel when it is located close to the outlet of the main channel.

2.4.6.1 Short side channel length of 10.0 mm

This experiment is performed with a constant side channel length of 10.0 mm, and the side channels located at 10.0 mm, 24.0 mm, and 38.0 mm from the 48.0 mm long main channel entrance. The experiment was done as a null dye velocity measurement, i.e., the side channel potential was controlled at 1000 V, and main channel potentials were varied to give different V_{stop} values at the intersection. Similarly, a calibration curve was obtained at pH 9.19 in each device for each null flow study, with 100-1000 V applied between the side channel and the waste reservoir. Overall mobilities of 4.99×10^{-5} , 4.45×10^{-5} , $4.99 \times 10^{-5} \text{ cm}^2/\text{V}\cdot\text{s}$ was used in each

device, giving 3.56×10^{-4} , 3.51×10^{-4} , $3.56 \times 10^{-4} \text{ cm}^2/\text{V}\cdot\text{s}$ for μ_{eo} in these devices. The null flow experiments were performed with the side channel potential applied at 1000 V, and main channel potentials varied from 1000 to 2200 V. All the buffers used were composed of 20 mM Tris, 4 mM boric acid, and 5 mM KCl controlling the ionic strength. All these devices were made of 0211 glass.

Figure 2-18 shows the result for this study plotted as dye velocities in the side channel v_2 vs. the electric field in the side channels, V_{stop}/L_2 , for different intersection positions of the 10.0 mm side channel along the main channel. In this case, the further away the intersection from the inlet, the lower the leakage, and the flow from the side channel inverts from leakage to pushback. This trend agrees with the theory (30), which indicates that the pressure drops severely at the entrance of the main inlet, where we expect more hydrodynamic effect which results in more leakage flow from the side channel. However, when the side channel is located close to the outlet of the main channel entrance and there is a reduced hydrodynamic effect, the model still predicts weak leakage, not pushback.

2.4.6.2 Side channel length of 20.0 mm

In this experiment, the side channel length was all at 20.0 mm, and we varied the side channel position as 10.0, 24.0, and 38.0 mm from the main channel entrance. Similarly, a calibration curve was obtained at pH 9.19 in each device for each null flow study, with 100-1000 V applied between the side channel and the waste reservoir.

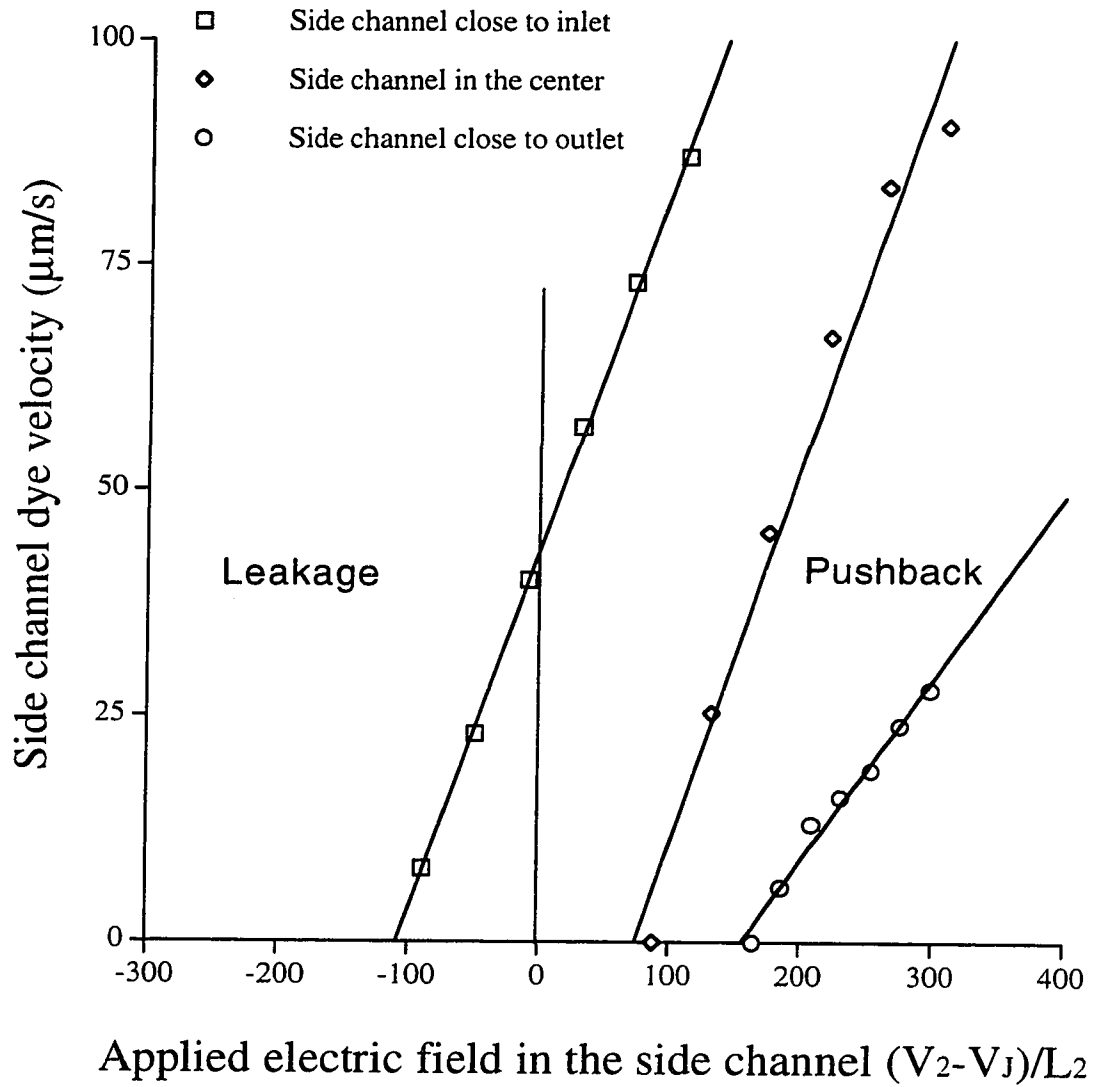


Figure 2-18 Flow velocity in the side channel as a function of the applied electric field there. Flow direction in the side channel changed from leakage to pushback as the side channel moved towards the main channel outlet. (Side channel length: 10.0 mm.)

Overall mobilities of 5.90×10^{-5} , 5.88×10^{-5} , $5.90 \times 10^{-5} \text{ cm}^2/\text{V}\cdot\text{s}$ was used in each device, giving 3.65×10^{-4} , 3.65×10^{-4} , $3.65 \times 10^{-4} \text{ cm}^2/\text{V}\cdot\text{s}$ for μ_{eo} in these devices. The null flow experiments were performed with the side channel potential applied at 1000 V, and main channel potentials varied from 1000 to 2200 V. All the buffers used were composed of 20 mM Tris, 4 mM boric acid, and 5 mM KCl controlling the ionic strength. All these devices were made of 0211 glass.

Figure 2-19 shows the result for this study, dye velocity in the side channel, v_2 , was plotted vs. the applied electric field in the side channel, V_{stop}/L_2 . In this plot, we can see that there was almost no leakage nor pushback flow in the side channel when the theory predicts the null velocity there. This result indicates that when the side channel is similar in length to that of the main channel, the side channel velocity will be very close to the theoretical prediction, thus we get the closest predicted flow at the null condition. This result was obtained 3 times from each devices, and three different devices for each kind were used.

2.4.6.3 Long side channel length of 40.0 mm

In this experiment, the side channel length was fixed as 40.0 mm, and side channel positions were 10.0 mm, 24.0 mm, and 38.0 mm from the main channel inlet. The side channel was controlled at 1000 Volt, and potential for the main channel was varied to find the voltage to stop the flow in the side channel. As usual, a calibration curve was obtained at pH 9.19 in each device before each measurement, with 100-1000

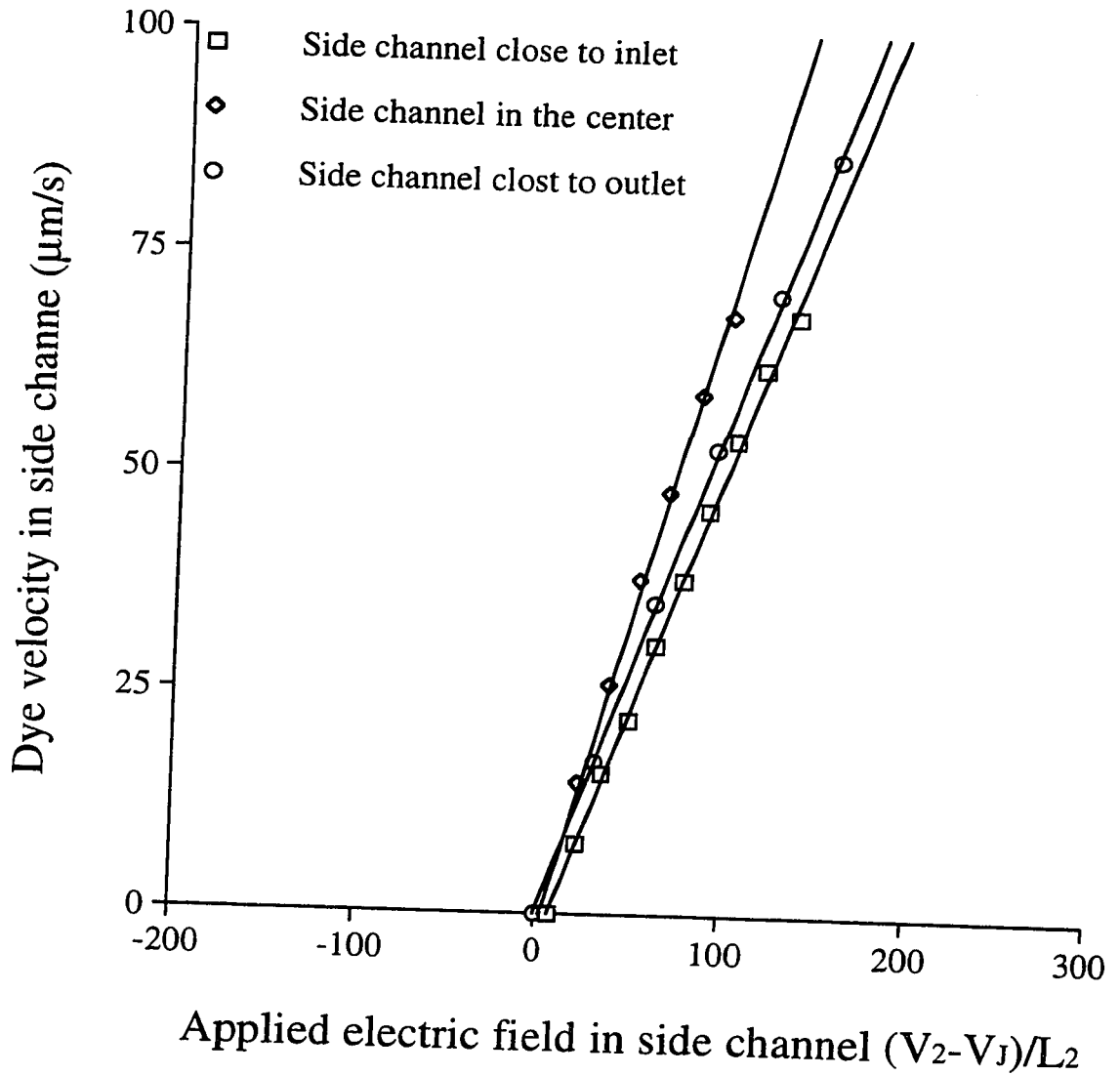


Figure 2-19 Flow velocity in the side channel as a function of the applied electric field there. Flow direction in the side channel changed from pushback to leakage as the side channel moved towards the main channel outlet. (Side channel length: 20.0 mm.)

volt applied between the side channel and the waste reservoir. Overall mobilities of 7.90×10^{-5} , 3.27×10^{-5} , and $7.90 \times 10^{-5} \text{ cm}^2/\text{V}\cdot\text{s}$ were used in each device, giving 3.85×10^{-4} , 3.39×10^{-4} , and $3.85 \times 10^{-5} \text{ cm}^2/\text{V}\cdot\text{s}$ for μ_{eo} in these devices. The null flow experiments were performed with the side channel potential applied at 1000 V, and main channel potentials varied from 1000 to 2200 V. All the buffers used were composed of 20 mM Tris, 4 mM boric acid, and 5 mM KCl controlling the ionic strength. All these devices were made of 0211 glass.

Figure 2-20 shows the result for this study plotted as the dye velocities in the side channel, v_2 , vs. the side channel electric field, V_{stop}/L_2 at the intersection. In this case, push back was observed when the intersection was close to the inlet of the main channel; when the intersection was further away from the inlet, we observed leakage. These results are in complete disagreement with the model of Hu, and we do not presently have an explanation. However, these experiments were repeated 3 times on each device and three different chips were used.

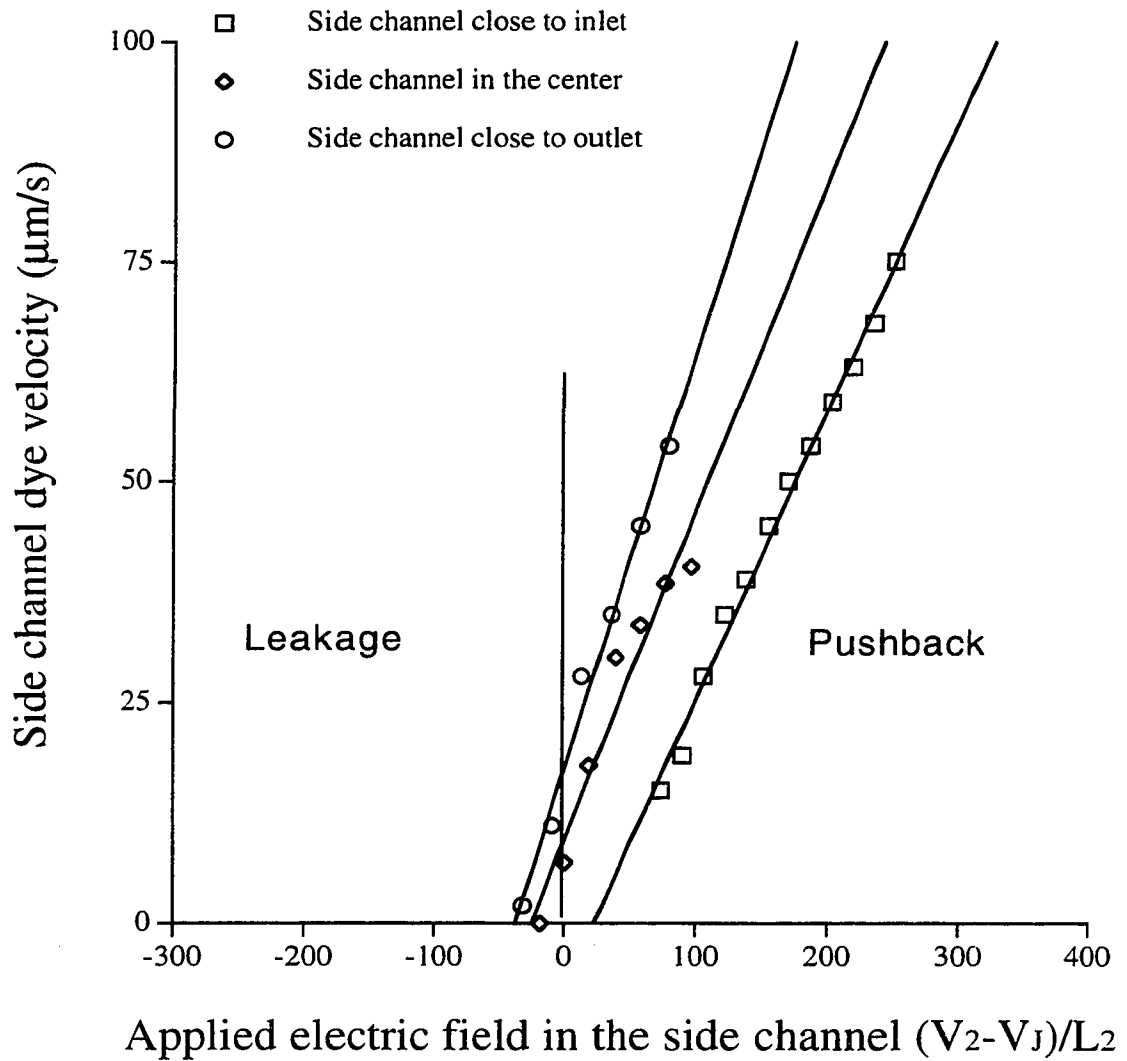


Figure 2-20 Flow velocity in the side channel as a function of the applied electric field there. Flow direction in the side channel changed from pushback to leakage as the side channel moved towards the main channel outlet. Side channel length: 40.0 mm.

2.5 Conclusion

A systematic study on both the side channel length and location along the main channel was undertaken for the intersecting channels in a T-shaped configuration. The series of experiments was done with both floating and controlled voltage on the side channel. It shows that hydrodynamic effects are very important in addition to the electrokinetic phenomenon in the electroosmotic flow system. The magnitude of leakage out of the side channel depends on both the side channel length and the position of the side channel along the main channel.

Given a fixed side channel position along the main channel, the longer the side channel, the higher the resistance to fluid flow. That is why we see less leakage from the longer side channel. The leakage ranges from 2% to more than 10% was observed from the experiments for long to short side channel lengths. Practically, we were not able to use a side channel length shorter than 5 mm, so have not discussed the extreme case for the worst leakage.

For the side channel which has a fixed length, the location of the side channel predominates. The entrance effect on the electroosmotic flow obtained from the model shows that the pressure profile along the centerline of the channel undergoes a sharp drop at the entrance mouth. The pressure then gradually recovers to the outlet value, which is the same as the inlet pressure. The leakage or pushback was observed differently with different side channel lengths, however, with the most symmetric device, neither leakage nor pushback was observed, which indicated that we had predicted flow at the null velocity condition.

Leakage can also be controlled with a bias voltage. Estimation of the voltage needed to stop the leakage flow can be calculated with junction voltage, given the value of the relative resistance which is proportional to the channel length. With this study, we achieved a better understanding of the microfluidic flow in miniaturized systems. This allows us to design devices with an optimized geometry to minimize the leakage contamination and gain better control over microfluidic flow.

References

- 1 Harrison, D.J.; Fluri, K.; Seiler, K.; Fan, Z.; Effenhauser, C.S.; Manz, A., *Science* **261**, 895, **1993**.
- 2 Manz, A.; Effenhauser, C.S.; Burggraf, N.; Harrison, D.J.; Seiler, K.; Fluri, K., *J. Micromech. Microeng.* **4**, 257, **1994**.
- 3 Seiler, K.; Fan, Z.; Fluri, K.; Harrison, D.J., *Anal. Chem.* **66**, 3485, **1994**.
- 4 Harrison, D. J.; Manz, A.; Fan, Z.; Ludi, H.; Widmer, H. M., *Anal. Chem.*, **64**, 1926-1932, **1992**
- 5 Seiler, K.; Harrison, D. J.; Manz, A., *Anal. Chem.*, **65**, 1481-1488, **1993**
- 6 Fan, Z.; Harrison, D.J., *Anal. Chem.*, **66**, 177-184, **1994**
- 7 Cheng, J; Shoffner, M.A.; Mitchelson, K.R.; Kricka, L.J.; Wilding, P., *J. Chromatogr.*, **732**, 151-158, **1996**
- 8 Cheng, J.; Shoffner, M.A.; Hvichia, G.E.; Kricka, L.J.; Wilding, P., *Nucleic Acids Research*, **24**, 380-385, **1996**
- 9 Effenhauser, C.S.; Manz, A.; and Widmer, H.M., *Anal. Chem.*, **67**, 2284-2287, **1995**
- 10 Harrison, D.J.; Fan, Z.H.; Seiler, K.; Manz, A.; Widmer, H.M., *Analy. Chim. Acta*, **283**, 361-366, **1993**
- 11 Jacobson, S.C.; Hergenroder, R; Moore, A.W.; Ramsey, J.M., *Anal. Chem.*, **66**, 4127-4132, **1994**
- 12 Jacobson, S.C.; Koutny, L.B.; Hergenroder, R.; W. Moore, A.W.; Ramsey, J.M., *Anal. Chem.*, **66**, 3472-3476, **1994**
- 13 Jacobson, S.C.; Hergenroder, R.; Koutny, L.B.; Warmack, R.J.; Ramsey, J.M., *Anal. Chem.*, **66**, 1107-1113, **1994**
- 14 Jacobson, S.C.; Hergenroder, R.; Koutny, L.B.; Ramsey, J.M., *Anal. Chem.*, **66**, 1114-1118, **1994**

-
- 15 Jacobson, S.C.; Hergenroder, R.; Koutny, L. B.; Ramsey, J.M., *Anal. Chem.*, **66**, 2369-2373, **1994**
 - 16 Jacobson, S.C.; Moore, A.W.; Ramsey, J.M., *Anal. Chem.*, **67**, 2059-2063, **1995**
 - 17 Jacobson, S.C.; Ramsey, J.M., *Electrophoresis*, **16**, 481-486, **1995**
 - 18 Jacobson, S.C.; Ramsey, J.M., *Anal. Chem.*, **68**, 720-723, **1996**
 - 19 Koutny, L.B.; Schmalzing, D.; Taylor, T.A.; Fuchs, M., *Anal. Chem.*, **68**, 18-22, **1996**
 - 20 Liang, Z.H.; Chiem, N; Ocvirk, G; Tang, T, Fluri, K.; Harrison, D.J., *Anal. Chem.*, **68**, 1040-1046, **1996**
 - 21 Manz, A.; Verpoorte, E.; Effenhauser, C.S.; Burggraf, N.; Raymond, D.E.; Widmer, H.M., *Fresenius Journal of Anal. Chem.*, **348**, 567-571, **1994**
 - 22 Moore, A.W.; Jacobson, S.C.; Ramsey, J.M., *Anal. Chem.*, **67**, 4184-4189, **1995**
 - 23 Raymond, D.E.; Manz, A.; Widmer, H.M., *Anal. Chem.*, **66**, 2858-2865, **1994**
 - 24 Raymond, D.E.; Manz, A.; Widmer, H.M., *Anal. Chem.*, **68**, 2515-2522, **1996**
 - 25 Vonheeren, F.; Verpoorte, E.; Manz, A.; Thormann, W., *Anal. Chem.*, **68**, 2044-2053, **1996**
 - 26 Woolley, A.T.; and Mathies, R.A., *Anal. Chem.*, **67**, 3676-3680, **1995**
 - 27 Sternberg, J. C.; *Adv. Chromatogr.*, **2**, 206-270, **1966**
 - 28 Liu, S.; Masliyah, J.H., *Int. J. Numerical Methods in Fluids*, **16**, 659, **1993**
 - 29 Masliyah, J.H., *Electrokinetic Transport Phenomena*, Alberta Oil and Sand Technology and Research Authority, Ch. 4, **1994**
 - 30 Hu, L., *Master Thesis*, Univ. Of Alberta, **1997**
 - 31 Kaushik, S.; Rubin, S. G., *Computers and fluids*, **24**, 27-40, **1995**
 - 32 Patankar, S. V. *Number. Heat Transfer*, **5**, 409-425, **1981**
 - 33 Patankar, S. V.; Spalding, D. B., *Int. J. Heat Mass Transfer*, **15**, 1787-1793, **1972**
 - 34 Palantar, S. V., *Hemisphere*, Washington, D. C., **1980**
 - 35 Qiu, X.C.; Hu, L.; Masliyah, J.H.; Harrison, D.J., *Transducers'97*, **1997**
International Conference on Solid-State Sensors and Actuator, 923-926, **1997**

-
- 36 Halliday, D.; Resnick, R., *Physics J.* Wiley and Sons: New York, **1960**
- 37 Parce, W. and Harrison, D.J., personal communication.
- 38 Harris, D.C., *Quantitative Chemical Analysis*, 3rd ed. W.H. Freeman and Company, **1991**

Chapter 3

Velocity Dependence on EOF and Mixing with Imbalanced ζ potentials

Abstract

Dye velocity in the side channel was measured for the case where the buffer pH values in the main channel were below the pH of the dye solution in the side channel. The change of the dye velocity was compared with the varying side channel length. When there was a ζ potential difference between the two channels, the monitored side channel dye velocity profile was unstable and complex. A slow oscillation of about 30 s was needed before the stable velocity was observed. Flow misbehavior was also discussed which gave us the reversed flow as we predicted with the normal electroosmotic flow. The causes and the reasons for these low EOF were also presented.

3.1 Introduction

In capillary electrophoresis, a background electrolyte with adequate buffering properties forms a continuum along the migration path. The existence of electroosmotic flow in fused-silica capillaries has contributed significantly to the full automation of capillary electrophoresis, allowing for on-line sample injection and detection as well as simultaneous analysis of cations and anions(1-3). The electroosmotic flow has a substantial influence on the time the analytes reside in the capillary. Electroosmotic flow (EOF) is superimposed on the electrophoretic motion of the analyte and, thus affects its migration time. For micellar electrokinetic chromatography with neutral micelles electroosmosis is the only source of motion, and therefore determines the reproducibility of the analysis. The understanding and control of electroosmotic flow have critical implications in the design of electrophoretic separations. A number of theoretical models have been developed to exert a proper control of electroosmotic flow (4-13).

The fluid mechanics associated with electroosmotic pumping and the use of potentials to control valving must be understood quantitatively in order to allow the development of design rules for microfluidic, electrokinetic device layouts. A number of subtle effects can play a major role in the flow behavior at intersections, particularly when the composition of the fluids being pumped varies within the device. In this chapter, we show that balanced electroosmotic flow is a very important requirement for predictable mixing between intersecting channels, and that the flow profiles and velocities will be complex when ζ potentials in each channel differ from one another.

3.2 Theory

The electroosmotic flow in a capillary column is produced by an electric field and transmitted by the drag of ions acting in a thin sheath of charged fluid adjacent to the silica wall column. The origin of the charge in this sheath is an imbalance between positive and negative ions in the bulk solution due to the need to balance the fixed negative charge on the silica wall. Electroosmosis in capillary electrophoresis has attracted much attention because of its importance for understanding the results of separation and its effect on run reproducibility.

In our present work, electroosmosis was responsible for the solvent mobilization. In this chapter, we will show the dependence of electric flow on zeta potential and the effect of imbalanced electroosmotic flow on the mixing within intersecting channels.

When flow is controlled by electroosmotic pumping in all intersecting channels, the surface charge in each channel is an important experimental variable. Velocity of the flow in each intersecting channel follows Equation 3-1:

$$v = \mu_{eo}E \quad 3-1$$

where v is the electroosmotic velocity, μ_{eo} is electroosmotic mobility, and E is the applied electric field. Also the electroosmotic mobility is proportional to the surface ζ potential, as expressed by Equation 3-2:

$$\mu_{eo} = \frac{\epsilon\zeta}{6\pi\eta} \quad 3-2$$

which relates μ_{eo} with the solvent dielectric constant, ϵ , viscosity, η , and ζ potential.

Variation in the surface, or ζ potential, between the different channels can lead to the addition of a Poiseuille flow term to the normal plug flow associated with electroosmotic pumping. This can be explained with the mass balance concept. At any of the mixing points, there must be mass balance. If we assign U_{in} and U_{out} as the flow velocities “in” and “out” of the intersection of a main channel with a side channel, and V as the flow velocity from the side channel, we come to the following mass balance Equation 3-3:

$$U_{in} + V = U_{out} \quad 3-3$$

This equation states that the flow into the intersection from both main and side channels will sum up to the flow leaving the intersection. This mass conservation requirement is always true.

When the electroosmotic mobility is equal in the system, the velocities in the different streams can be simply calculated from Equation 3-2. However when the electroosmotic mobility is different in each channel, the velocity in each channel will be affected. The ζ potential, and so the mobility is highly dependent on the pH of the solvent. Since the velocity of the flow from the different streams is not the same, when the flow with a higher velocity enters the stream where the flow velocity is low, there will be a pressure generated. This additional pressure driven flow is called Poiseuille flow.

Variation in the surface, or ζ -potential, between the different channels can lead to the addition of a Poiseuille flow term (P) to the normal plug flow associated with electroosmotic pumping, which can be expressed as Equation 3-4 (14):

$$v = \mu_{obs} E + P$$

3-4

This arises due to the need for mass balance, since variations in ζ -potential will lead to a mass flow difference, even if the electric fields are unchanged. This situation will commonly arise experimentally, whenever the ionic strength or the pH in two channels is not the same (15).

In the thesis of Hu (16), a series of calculations was performed in which constant potentials were applied to each channel, the reduced ζ' -potential in the side channel was constant at -1, and the reduced ζ -potential in the main channel was allowed to vary from 0 to -1.5. The ζ potentials used in the Model were all normalized to ze/kT , where z is the charge of analyte, e is the electron charge, 1.602×10^{-19} C, k is Boltzmann constant (J/K), and T is the absolute temperature (K). When we choose near room temperature, 298 K (25 °C), the ζ value will be 25 mV. Here ζ refers to the main channel, and ζ' to the side channel. Figure 3-1 shows that the reduced velocity, V , in the side channel changes significantly as ζ changes in the main channel, even though the electrokinetic pumping forces do not change. In fact, if the pumping force in the main channel becomes low enough, the flow from the side channel can reverse the flow direction upstream (U_{in}) of the intersection (14,16). This phenomenon is known as “pushback” flow as we described in Chapter 2.

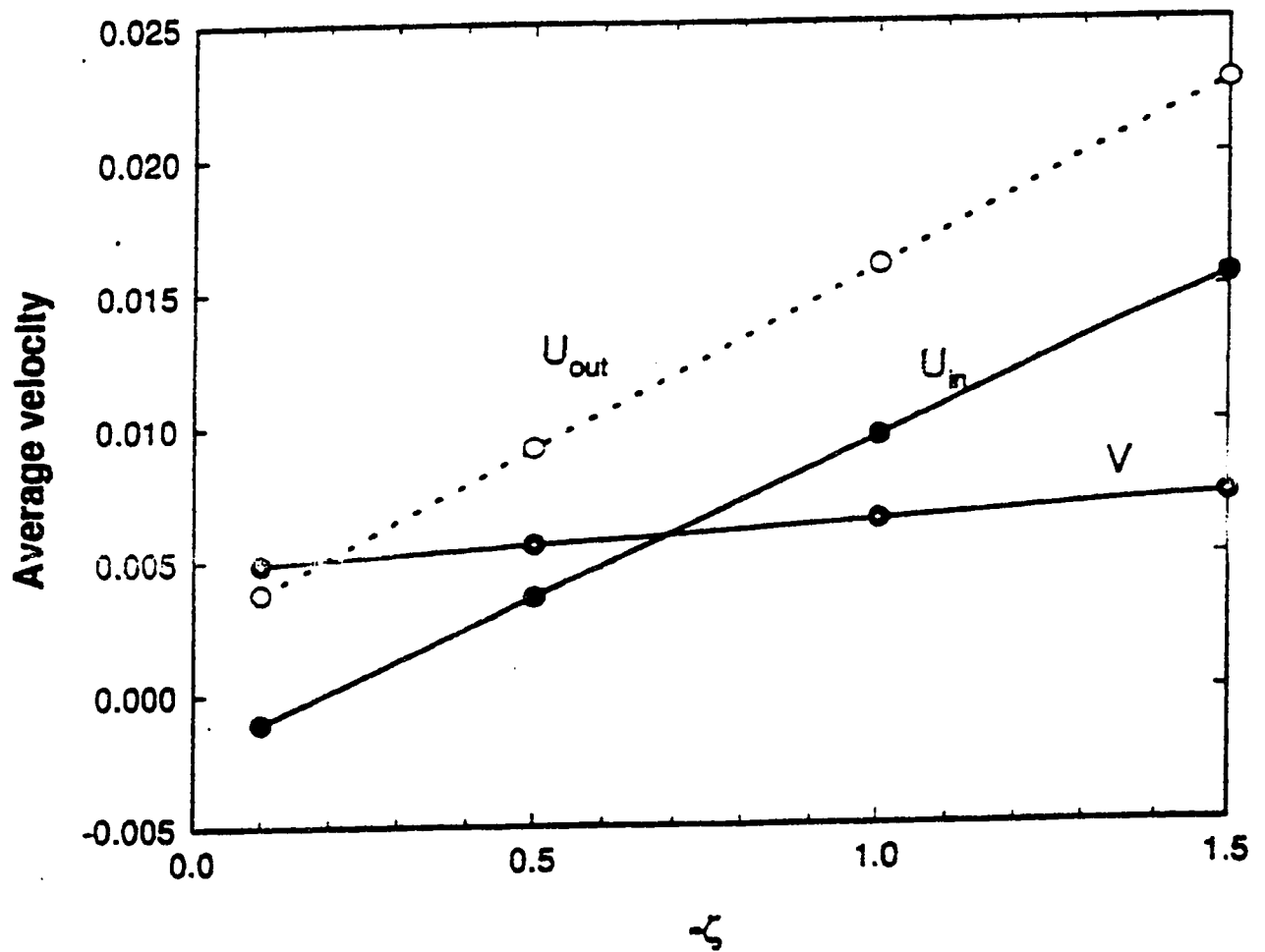


Figure 3-1 Calculated linear dimensionless velocities entering the channels from main (U_{in}) and side (V), while exiting main channel outlet (U_{out}). Reduced potential 5500 were applied to the side channel and the main channel inlet, while the main channel outlet grounded. The reduced length for main and side channels were 1000 and 800. The ζ potential is -1 in the side channel, and is variable for the main channel. (Adapted from Hu in Ref.16)

3.3 Experimental section

3.3.1 Device fabrication

The devices used were UACQ1 and UACQ2, as in Chapter 2. The device dimensions are the same as described in section 2.3.2, detailed channel dimensions are illustrated in Figure 2-4. Briefly, the main length is 49 mm for all 4 different designs, and side channel lengths are 5.0, 10.0, 20.0, and 40.0 mm for designs #1, #2, #3, and #4. All the channels were 10 μm deep and 30 μm wide. The fabrication procedure is the same as described in Chapter 2, section 2.3.1.

3.3.2 Instrumentation

The instrument set-up and signal detection system for all on-chip study was described in section 2.3.3, the block diagram is shown in Figure 2-5. The electrophoretic mobility of fluorescein was measured on the commercial Beckman CE, P/ACE 5010, with a 214 nm UV detector.

3.3.3 Materials and reagents

Borosilicate glass (Pyrex, Borofloat) was from Paragon Optical (Reading, PA). and 0211 glass was from Corning glass (Parkridge, IL). Microslides and Sparkleen detergent were from Fisher Scientific (Edmonton, Canada). The Hollow diamond drill bit

was purchased from Lunzer (Saddle Brook, NJ). Crystal bond came from Aremco (Ossining, NY).

The buffer for all electrophoresis was made of 20 mM tris(hydroxymethyl)aminomethane (Tris) (Terochem, AB, Canada), 5 mM boric acid (J.T. Baker Chemical CO, Phillipsburg, NJ.) and 4 mM KCl. It was used to prepare a series of buffers with different pH values of 9.19, 9.02, 8.83, 8.62, 8.39, 8.20, or 7.97, adjusted with 1 M HCl. With the high salt concentration of the original buffer, these buffers of different pH will remain the same ionic strength. The Na⁺ salt of fluorescein (Molecular Probes, Eugene, OR) was dissolved into the pH 9.19 buffer at a concentration of 2 μ M for studies except where otherwise indicated. This ensured the sample had the same ionic strength and pH as the buffer, in order to eliminate sample stacking effects.

3.3.4 Operation procedure

All reagents were introduced to the channels through syringes equipped with 0.22 μ m microfilters. Running buffer was introduced to all the reservoirs at the beginning of each experiment and channels were flushed with buffer by vacuum for 15 minutes. Fine Pt wires with insulating sleeves were inserted into the reservoirs on the device as electrodes. Fluorescent sample was then introduced into the side channel, and potentials were applied either between sample reservoir and the sample waste, or from buffer reservoir to separation waste for injection or separation mode. An Argon ion laser operated at 488 nm was focused onto the channel, and the photomultiplier tube was aligned with the dye present in the region of detection. After use, channels were flushed

by vacuum with 0.1 N NaOH for 20 minutes, followed by MilliQ Ultrapure pure water flush for 20 minutes. Chips were stored with pure water filling all the reservoirs and channels, and covered with parafilm to prevent water evaporation.

3.4 Results and Discussion

3.4.1. Dye velocity at different pH

From the model cited in Chapter 2, we noted that the dye velocity will be affected if the ζ potentials are different between the main and side channel. The following data sets are the results for flow velocity changes in the side channel with pH changes in the main channel.

We chose to perform the experiments with a constant pH in the dye side channel, and varied pH in the main buffer channel. We monitored the dye velocity in the side channel before its mixing with the buffer in the main channel, so it was not subject to pH changes. In this way the pH dependence of fluorescein mobility and fluorescent yield were not an issue. Any influence on the dye velocity was caused by the main channel buffer pH changes.

3.4.1.1 Dye velocity change with main channel buffer pH--Side channel floating

This series of experiments were done with a constant side channel length of 20.0 mm. The pH in the buffer channel was 9.19, 9.02, 8.83, 8.62, 8.39, 8.20, 7.97 in the series, while the pH in the side channel for dye remained at 9.19. The calibration curve was obtained at pH 9.19, with 100-1000 V applied between the side channel and the waste reservoir. Overall mobilities of 5.88×10^{-5} and $3.27 \times 10^{-5} \text{ cm}^2/\text{V}\cdot\text{s}$ were obtained, giving 3.65×10^{-5} and $3.39 \times 10^{-4} \text{ cm}^2/\text{V}\cdot\text{s}$ for μ_{eo} for 0211 and Pyrex glass devices,

respectively. Leakage studies were performed with 1000 to 2000 V applied from main channel to waste reservoir, with a floating side channel. All the buffers used were composed of 20 mM Tris, 4 mM boric acid, and 5 mM KCl controlling the ionic strength, 1 M HCl was used to adjust the buffer pH.

Figure 3-2 shows the plot of the flow velocity of the dye from the side channel vs. the voltage applied to the main channel. The plot shows that with higher voltage applied to the main channel more leakage occurs. Figure 3-2a and Figure 3-3a show two typical data sets. In one case the expected linear dependence of leakage rate on applied potential was observed. This linear dependence is predicted by Hu's thesis (16). In the other data set deviations from linearity were seen. This variation could be caused by the original shape of the individual velocity calibration curves, which were shown as Figure 3-2b and Figure 3-3b, respectively. Figure 3-2 showed the data from the device made of 0211 glass, and Figure 3-3 were from the Pyrex glass.

This study was done in the floating configuration, which means that we left the side channel disconnected. Since there was no electric field in the side channel, there was no force to drive the dye out of the side channel, so the dye flow we measured was completely from the leakage phenomenon. With a higher voltage applied to the main channel, there was more viscous drag from the main channel when the solvent flowed by. This effect "pulls" more dye solution out from the side channel, and the increased leakage velocity allows us to observe higher dye intensity in the side channel.

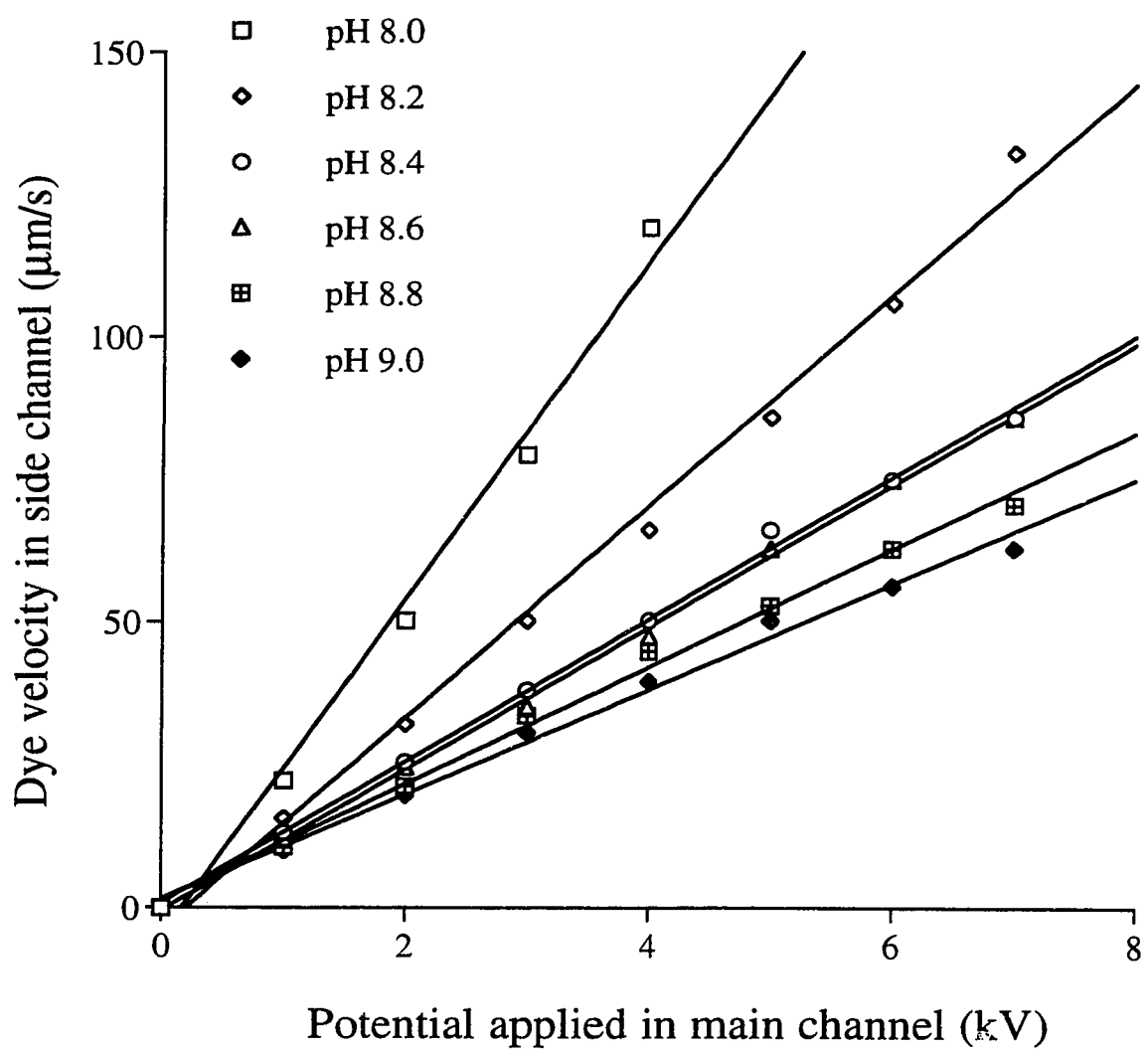


Figure 3-2a Measured dye velocity with the driving force in the main channel. Dye was at pH 9.2, while main channel buffer pH indicated. (Data from 0211 glass device, $\mu_{\text{obs}} = 5.883 \times 10^{-5} \text{ cm}^2/\text{V}\cdot\text{s}$).

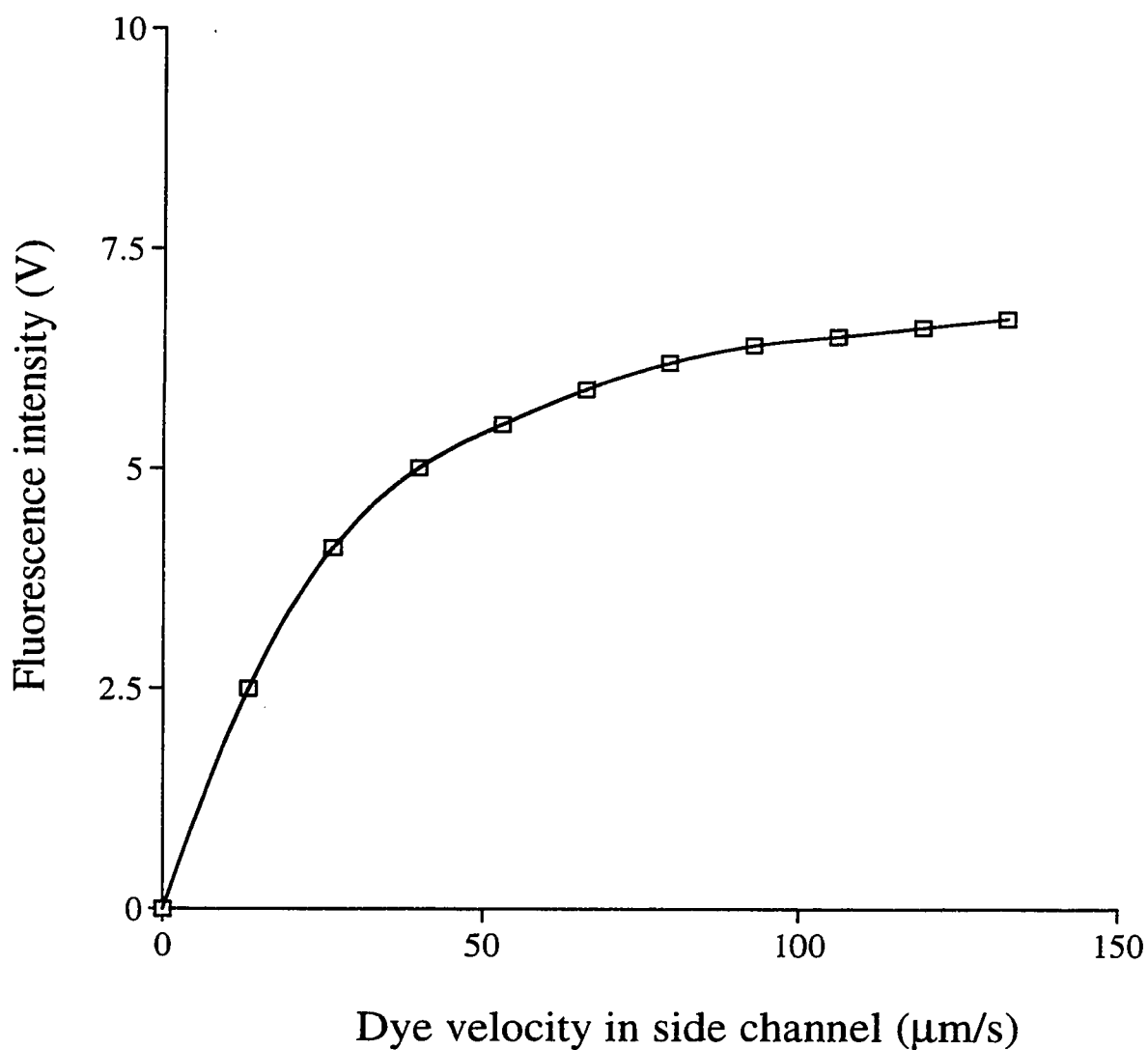


Figure 3-2b Calibration curve showing dye intensity vs. the calculated velocity from the side channel. Voltage applied was from 0 to 1000 V. Curve is drawn for clarity only. (Data from 0211 glass device, $\mu_{\text{obs}} = 5.883 \times 10^{-5} \text{ cm}^2/\text{V}\cdot\text{s}$).

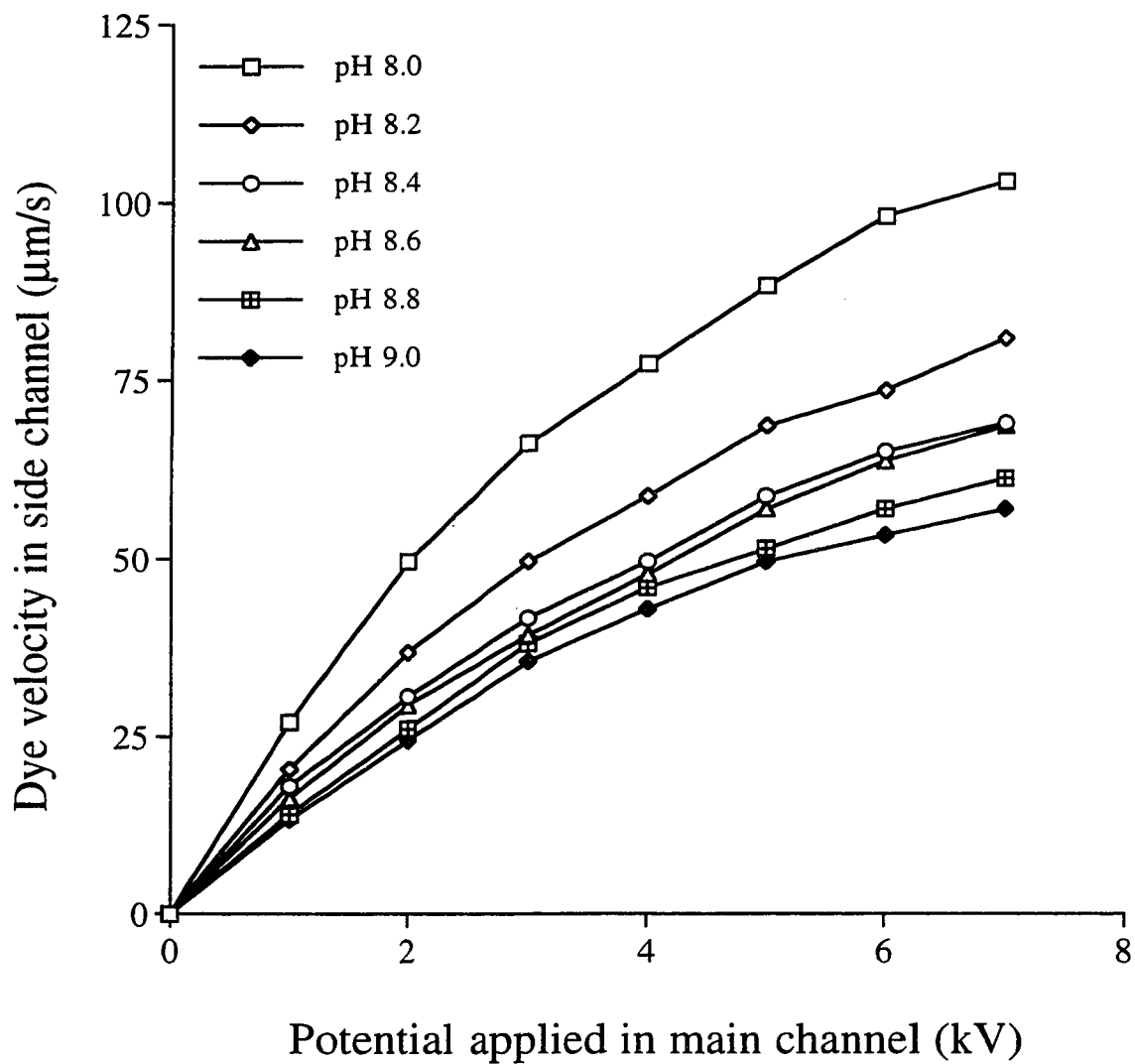


Figure 3-3a Measured dye velocity with the driving force in the main channel, dye was at pH 9.19 (Data from pyrex glass device, $\mu_{\text{obs}} = 3.27 \times 10^{-5} \text{ cm}^2/\text{V}\cdot\text{s}$).

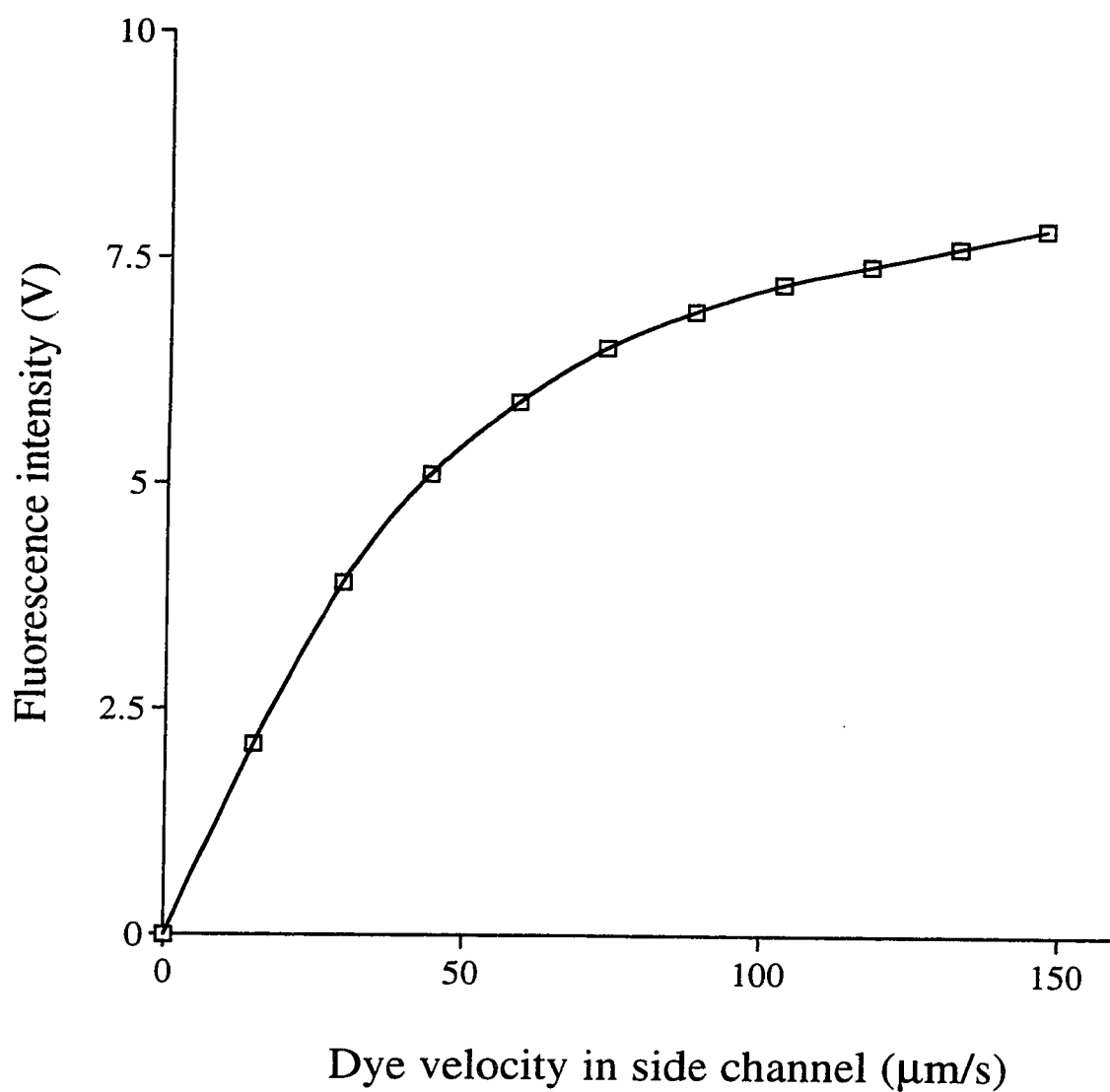


Figure 3-3b Calibration curve showing dye intensity vs. calculated velocity. Voltage applied was from 0 to 1400 V. Curve is shown for clarity only. (Data from pyrex glass device, $\mu_{\text{obs}} = 3.27 \times 10^{-5} \text{ cm}^2/\text{V}\cdot\text{s}$)

Comparing the plots from the buffers with different pH, we found that at the same applied voltages on the main channel, there is more leakage from the floating side channel when the main channel buffer pH is much lower than the side channel dye pH.

With the same applied voltages to the main channel, only the different ζ potential from the different pH buffer will affect the main channel flow velocity. According to the mobility measurements with the different pH buffers, presented in Chapter 2, the buffer electroosmotic mobility decreases from 3.25×10^{-4} to $2.98 \times 10^{-4} \text{ cm}^2/\text{V}\cdot\text{s}$ when the pH decreased from 9.2 to 8.0. This indicates that the lower pH buffer from the inlet of the main channel will have a lower mobility compared to its later mixture with the dye solution, which was at the highest pH. When the low pH buffer in the main channel passed the intersection and mixed with some leaking high pH dye solution, it would produce a higher pH for the mixed solution, so it flowed faster downstream of the main channel outlet. This fast flow resulted in a force, or pressure driven flow, pulling more dye solution out of the side channel, and giving a higher dye velocity. The lower the pH buffer used in the main channel, the bigger the difference in pH between buffer and dye solution, inducing a bigger ζ potential difference downstream, which consequently caused more pressure driven flow.

3.4.1.2 Dye velocity change with buffer pH--controlled side channel

In this study the dye solution was constant at pH 9.19. With a fixed side channel length of 5.0 mm, a series of buffers of constant ionic strength with pH values of 9.19,

9.02, 8.83, 8.62, 8.39, 8.20, and 7.97 were driven through the main channel, while viewing the velocity of the dye in the side channel. The calibration curve was obtained at pH 9.19, with 100-1000 V applied between the side channel and the waste reservoir. Overall mobilities of $5.80 \times 10^{-5} \text{ cm}^2/\text{V}\cdot\text{s}$ was obtained, giving $3.64 \times 10^{-4} \text{ cm}^2/\text{V}\cdot\text{s}$ for μ_{eo} in this device. The null flow experiments were performed with the side channel potential applied at 1000 V, and main channel potentials varied from 1000 to 2200 V. All the buffers used were composed of 20 mM Tris, 4 mM boric acid, and 5 mM KCl controlling the ionic strength. The device was made of 0211 glass.

Figure 3-4 shows the plots of dye intensity from the side channel vs. the voltage applied to the main channel at different pH values. The flow out of the side channel decreased as the main channel voltage increased. This effect is due to the increasing junction potential at the intersection, which decreases the potential drop along the side channel until it goes to zero. A calculation of the potential on V_1 required to reach the null potential condition on the side channel, using Equation 2-5, gives a value of 2000 V. The difference between this value and the experimental data in Figure 3-4, indicate some pushback would occur in a floating configuration. This is to say that since flow from the side channel stopped when there was still an electric field driving it into the intersection, there must have been a countering pressure force from the intersection into the side channel. In a floating configuration that pressure would lead to a “pushback” effect. This effect was greater when the pH difference was greater. Also, we observed that when the buffer pH decreased, the measured signal intensity decreased. This might be due to greater back pressure differences between the side channel and the main channel as the pH difference, and hence the ζ potential difference increased.

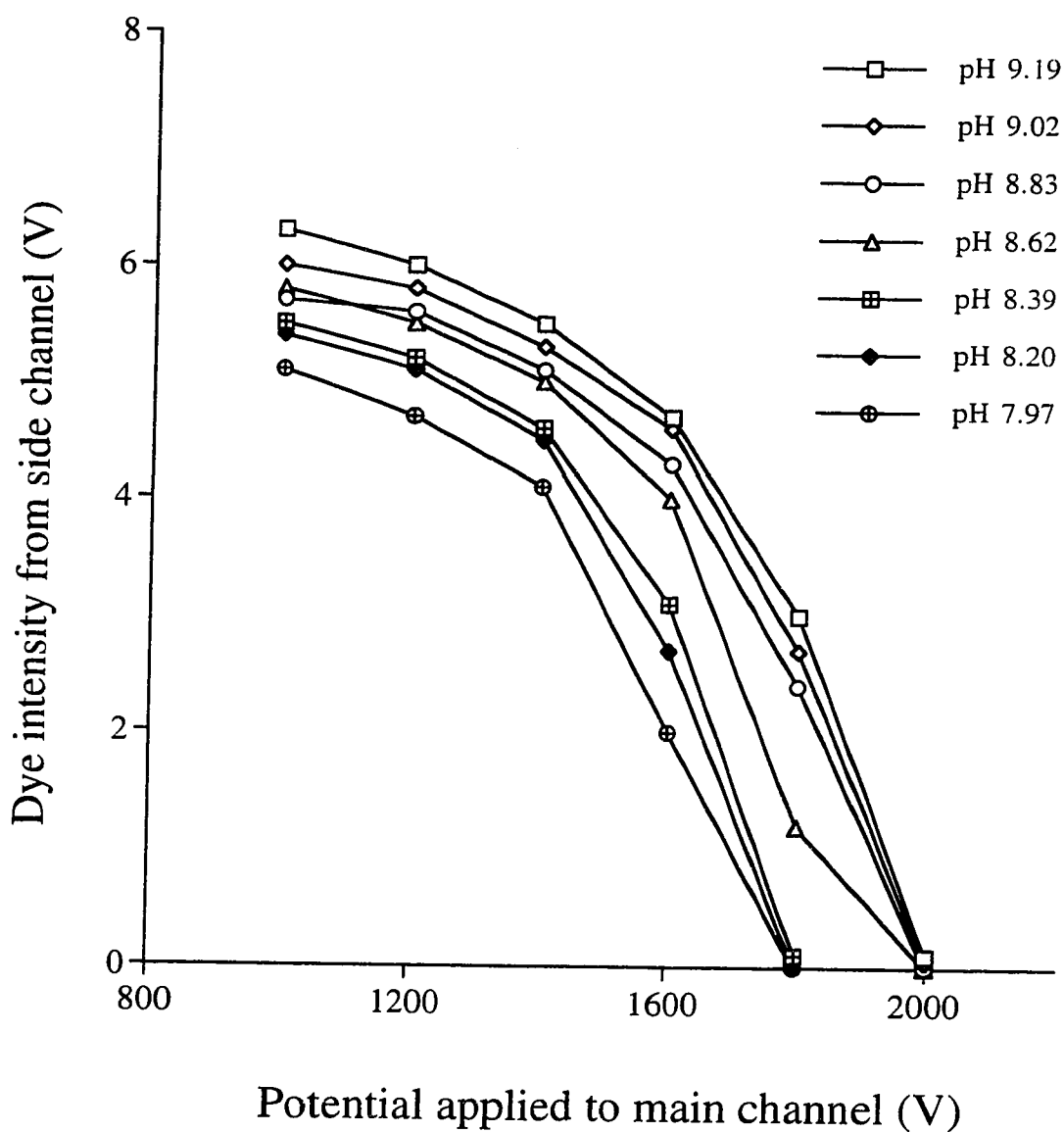


Figure 3-4 Measured fluorescent intensity as a function of voltage applied to the main channel. 1000 V applied to the side channel. Side channel length was 5.0 mm. The detector was located 500 μm from the intersection in the side channel.

From the consideration of electroosmotic flow as the only governing effect, we calculated the theoretical dye velocity with Equation 3-3. However, the measured dye velocity should obey Equation 3-4, with the Poiseuille term. In this section, we plotted the ratio of the measured dye velocity to the theoretical velocity calculated as a function of main channel pH value, which showed the extent of deviation of the true dye velocity from its predicted value.

Figure 3-5 is one of the representative results from a 0211 glass device with a side channel length of 5.0 mm, when the applied voltage in the main channel was 1600V. We monitored the dye flow behavior in the side channel as a function of the pH difference from the main channel, with the ionic strength and solution resistivity kept constant for the two streams. The figure shows the ratio of the measured dye flow in the side channel relative to the flow predicted by simple electroosmotic pumping consideration. We observed a velocity ratio decrease as the pH difference increased from the two streams. This is due to the electroosmotic mobility imbalance. In our valveless microfluidic system, solvents are pumped by electroosmotic flow (EOF). Without the pressure driven flow, the measured dye velocity will be the same as the calculated velocity using the known value of dye mobility. However, when there is a pH imbalance, there will be a ζ potential change in the main channel after the buffer is mixed with dye at the intersection. This is the source of Poiseuille flow, which leads to more complex velocity profiles.

The complicated dye velocity dependence on pH is clearly shown in the above mentioned Figure 3-5, where the true measured velocity is the sum of both electroosmotic flow and the Poiseuille flow. Without the Poiseuille term, the ratio should be plotted as a

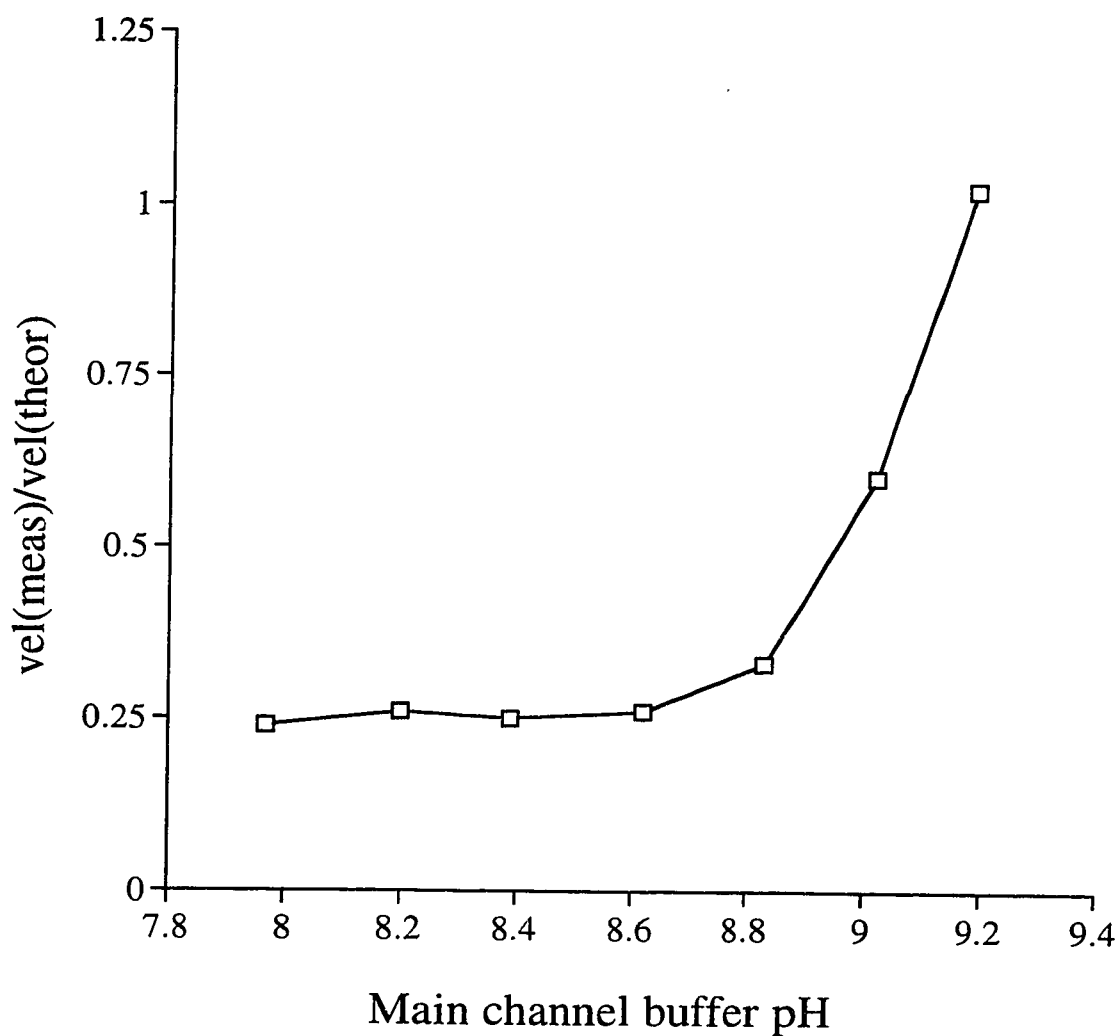


Figure 3-5 The ratio of measured flow velocity compared to the theoretical velocity in the side channel as a function of different buffer pH in the main channel. (Side channel length was 5.0 mm, side channel dye at pH 9.19, $V_1 = 1600$ V, $V_2 = 1000$ V. Dye velocity was calculated with $\mu_{\text{obs}} = 5.80 \times 10^{-5} \text{ cm}^2/\text{V}\cdot\text{s}$)

flat line of 1. However, we observed that when the pH decreased in the main channel, the velocity in the side channel decreased, even though the pH and electric field remained constant in the dye channel. The velocity profile showed the measured dye velocity was close to the theoretical calculation when the buffer pH was the same as the dye pH of 9.2, so that there was no ζ potential imbalance. However, as the buffer pH was lowered while the dye pH remained at 9.2, the measured dye velocity became smaller. The measured velocity decreased abruptly when buffer pH changed from 9.2 to 8.8, then it remained the same as the buffer pH decreased further to 8.0. This result is in accordance with the buffer electroosmotic mobility measurement in Chapter 2, as shown in Table 2-3. Electroosmotic mobility μ_{eo} decreased fast from 3.25 to $2.98 \times 10^{-4} \text{ cm}^2/\text{V}\cdot\text{s}$ when pH changed from 9.2 to 8.8, then μ_{eo} remained close to $3.0 \times 10^{-4} \text{ cm}^2/\text{V}\cdot\text{s}$ when buffer pH decreased further to pH 8.0. This result indicated that there was more ζ potential change from pH 9.2 to 8.8, and almost constant ζ potential from pH 8.8 to 8.0.

Comparing the data from Figure 3-5 to the theory as shown in Figure 3-1, we noticed that the Model suggests a gentle change of velocity (V) in the side channel as ζ potential in the main channel decreases, while the experimental data have an abrupt decrease when main channel pH decreases, and remain constant later. However, we must note that the two plots are not directed comparable. In experimental data from Figure 3-5, we plotted the side channel velocity as a function of main channel pH, while Figure 3-1 plotted velocity vs. the main channel ζ potential, which has a non-linear pH dependence. Another difference is that Figure 3-1 has the same ζ potential along the whole main

channel, but in the experimental data there was a third ζ potential downstream of the solvent mixing. Nevertheless, qualitatively the velocity change we observed in Figure 3-5 agrees with the deviation predicted theoretically by Figure 3-1. Quantitatively the experimental data showed a 50% velocity change or more, while the theory predicted a 20% change in the reduced ζ potential 0-1.5 range. It is possible that both experiment and theory need refining before quantitative comparison work.

The above study shows that the Poiseuille flow plays a profound role when the system has mixing streams with different pH, so that the ζ potential balance is a very important issue in the microfluidic system. At present the resulting flow rate is quantitatively predictable only when the ζ potentials are balanced.

Figure 3-6 is a series of plots from the same device used for Figure 3-5 with different applied voltages in the main channel of 1000, 1200, 1400, 1600, and 1800 V. These correspond to electric fields of 67, 135, 204, 272, and 306 V/cm in the main channel before the intersection, and 275, 220, 165, 110, and 55 V/cm in the side channel. We observed that the ratios of the measured velocity to the theoretical velocity increased with the increasing potential applied to the main channel. Several factors change as the applied voltage in the main channel (V_1) increases: the driving force (electric field) for flow in the main channel increases, while the electric field in the side channel will decrease. This will mean the relative flow from the side channel and the additional pressure driven flow it introduces downstream due to its higher velocity will decrease as V_1 increases. This is consistent with the data in Figure 3-6. However, it must also be noted that the ΔpH downstream becomes smaller as V_1 increases, because less of the high

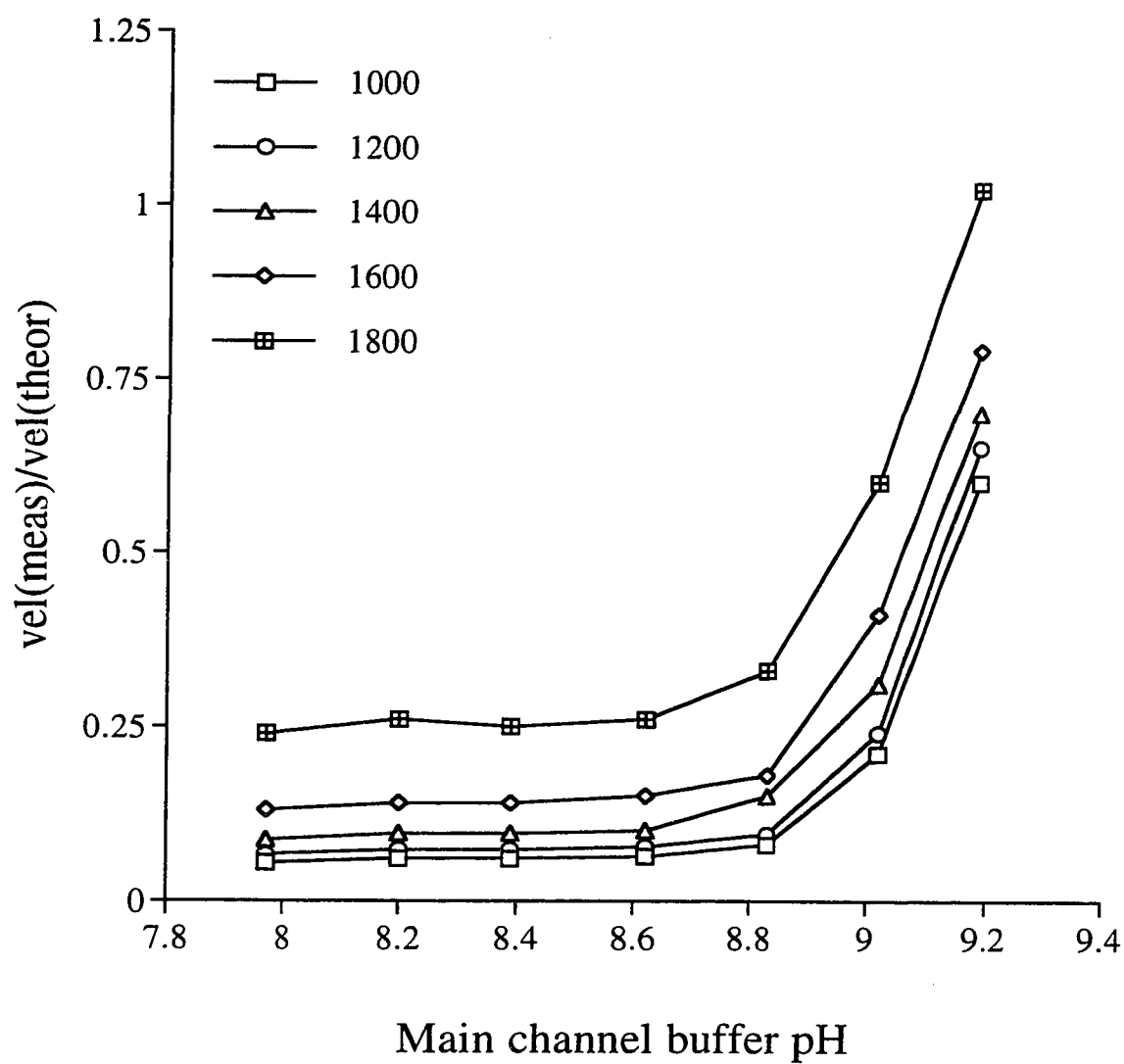


Figure 3-6 Measured velocity ratio of dye in the side channel as the pH in the main channel drops below the value in the side channel. Side channel length is 5.0 mm, V_2 was fixed at 1000 V, while V_1 values as indicated.

pH side channel solution is introduced. Since increasing pH and ζ downstream would work to lessen the back pressure met by the side channel, this effect works in the opposite direction. The data suggest the first consideration must be more important.

3.4.2 Dependence of dye velocity at different side channel length

To establish better design rules, we compared the leakage extent in the devices with various side channel lengths. All the devices had the same length, 49.0 mm, for the main channels, but the side channel lengths were 5.0 mm, 10.0 mm, 20.0 mm, and 40.0 mm. To compare the leakage from different side channel lengths, we used the velocity ratio of the measured velocity to the theoretical dye velocity from the different side channels. The calibration curve was obtained at pH 9.19 in each device, with 100-1000 V applied between the side channel and the waste reservoir. Overall mobilities of 4.48×10^{-5} , 4.99×10^{-5} , 5.90×10^{-5} , and $7.90 \times 10^{-5} \text{ cm}^2/\text{V}\cdot\text{s}$ were obtained in each device, giving 3.51×10^{-4} , 3.56×10^{-4} , 3.65×10^{-4} , and $3.85 \times 10^{-4} \text{ cm}^2/\text{V}\cdot\text{s}$ for μ_{eo} in device #1, #2, #3, and #4 respectively. The null flow experiments were performed with the side channel potential applied at 1000 V, and main channel potentials varied from 1000 to 2200 V. All the buffers used were composed of 20 mM Tris, 4 mM boric acid, and 5 mM KCl controlling the ionic strength. All these devices were made of 0211 glass.

Figure 3-7 is the plot of the velocity ratios from the side channel vs. pH in the main channel. This plot combines all the different lengths of the side channels and was plotted for the condition of constant electric field on the upstream main channel, i.e. the

difference between the voltage applied to the buffer channel and the junction voltage remained a constant for all the different devices. The electric field in the main channel before intersection was around 220 V/cm, which ensured a constant driving force on the buffer in this experiment. However, under this constant main channel electric field condition, the electric fields for the side channel were 165, 132, 93, and 77 V/cm for device #1, #2, #3, and #4, respectively. Another way to compare the effect from the different side channel lengths is to plot the results at a fixed side channel electric field strength, which ensures there is the same electrokinetic driving force for dye solution in the side channel. Figure 3-8 is the plot of the measured to theoretical dye velocity ratios from the side channel vs. pH in the main channel. The electric field for the side channels were the same as 120 V/cm, while the electric fields in the main channels before the intersection were 277, 225, 186, and 160 V/cm for devices #1, #2, #3, and #4, respectively. Both Figure 3-7 and Figure 3-8 showed that the velocity ratios decreased as the buffer pH decreased in the main channel, as we can expect from the previous discussion in section 3.4.1.2. Comparing the different side channel lengths, we can see that the short side channels were most affected by the pH imbalance in the system, while the longest channel, 40.0 mm, was the next most influenced. The most symmetric design, with a side channel length of 20.0 mm, suffered the least influence from the “pH imbalance” phenomenon. This is similar to the geometric results discussed in the Chapter 2, where we concluded that the 20.0 mm side channel had the flow behavior closest to the model, as indicated by the “no leakage” and “no pushback” performance discussed in section 2.4.5.2 in the null leakage study.

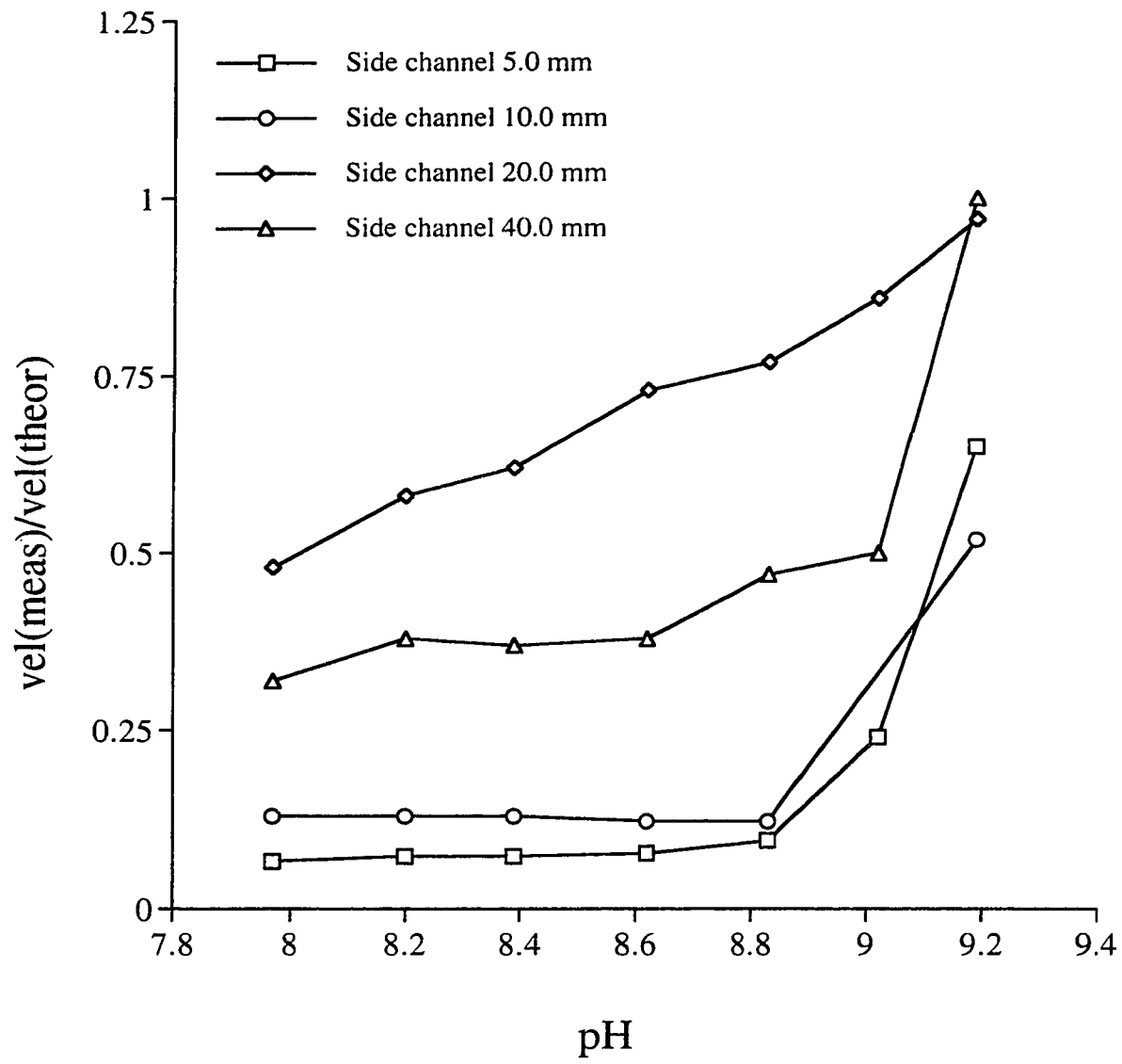


Figure 3-7 Dye velocity ratio in the side channel as the pH in the main channel drops. Different side channel lengths as indicated. Same main channel electric field strength applied.

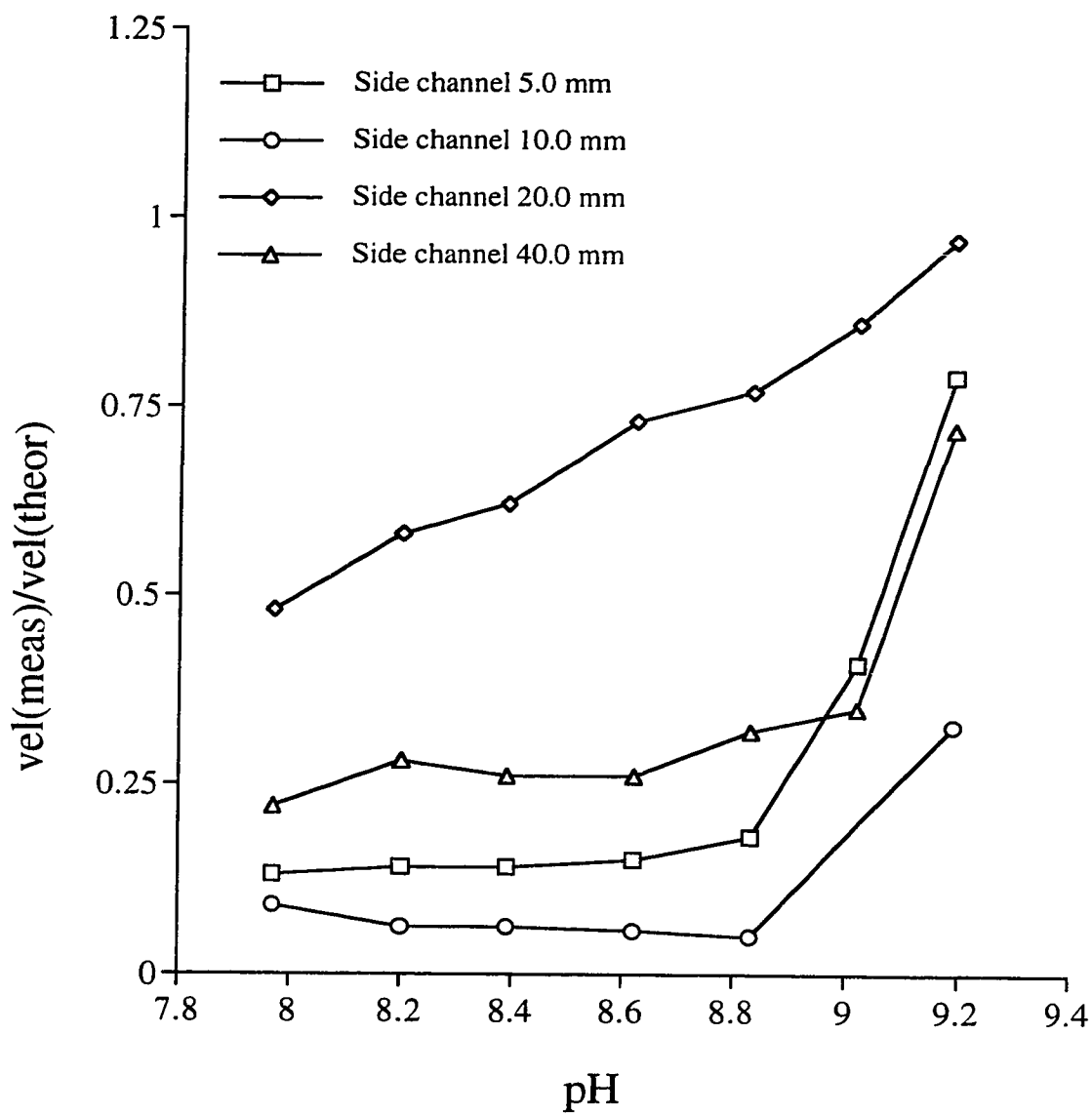


Figure 3-8 Dye velocity ratio in the side channel as the pH in the main channel drops. Different side channel lengths as indicated. Same side channel electric field strength applied.

3.4.3. Mixing pattern and its dependence on ζ potential

Mixing is always an important issue in microfluidic systems. We need to understand the mixing behavior so as to achieve proper mixing. In this work we monitored the mixing with both velocity and concentration studies. For the velocity study, we monitored the dye intensity 500 μm before the intersection in the side channel where the dye resided. The velocity of the dye solution upstream of the T was monitored by the intensity dependence of the dye on fluid velocity. A high intensity of laser power was applied so that the fluorescent intensity of the dye solution depended on the fluid flow velocity. This effect arises from photobleaching effects. For the concentration measurements, we monitored the dye intensity downstream far from the mixing intersection and close to the main channel outlet. We used lower laser power, employing a neutral density filter which cut off 99% of laser power used in the velocity dependent study, so that photobleaching effects no longer occurred. The intensity change at this point is thus due to the concentration change after mixing.

For comparison, we first studied the mixing with balanced ζ potentials. This is to say equal ζ potentials in each channel. The data presented below were obtained from both Pyrex and Borofloat glass devices. We had the same pH 9.0 buffer in both the side and main channels. Figure 3-9 shows the side channel dye velocity change with time, as a function of the main channel applied voltage change. We can conclude that the two streams equilibrated rapidly when the pH was equal in the system. The concentration measurements downstream of the mixer confirmed the same results. These results are consistent with the earlier studies of Fluri from this group (17,18,19).

Figure 3-10 shows how important the effect of unbalanced ζ potentials can be. A time dependent result not modeled by the steady state calculations was seen. In this experiment, two streams of differing pH, but equal resistivity were mixed at a T junction. The flow rate was measured in the side channel, upstream of the mixing point. When there was a pH imbalance between the streams, slow oscillations in flow rate were seen over a period of 30 s upon each adjustment of flow from the two channels. Comparing to the concentration measurement, we again observed unstable mixing for a period of 30 seconds before finally reaching equilibrium. It is clear the time taken to reach equilibrium when the ζ potential differs between channels is long enough to play a significant role during mixing. We have yet to determine the cause of this effect, however, the time frame is similar to the time it would take for the leading edge of the newly formed mixture to pass the length of the downstream channel and exit into the waste reservoir. Note that a newly generated mixture will have a different ζ potential from either the original buffer or the dye. This newly mixed plug might have a higher ζ potential compared to the existing buffer in the downstream main channel, which consequently moves slower than the newly mixed solution plug. Initially upon mixing, this newly formed plug will be small in volume, and face difficulty in pushing the large volume of slow moving buffer downstream. However, later on this higher ζ potential plug becomes bigger in volume, it becomes easier to push the relatively smaller slow moving buffer volume left downstream of the main channel. This process creates variability in the pressures generated, but will finally stop when the leading edge of the buffer/dye mixture at the intersection reaches the outlet of the main channel.

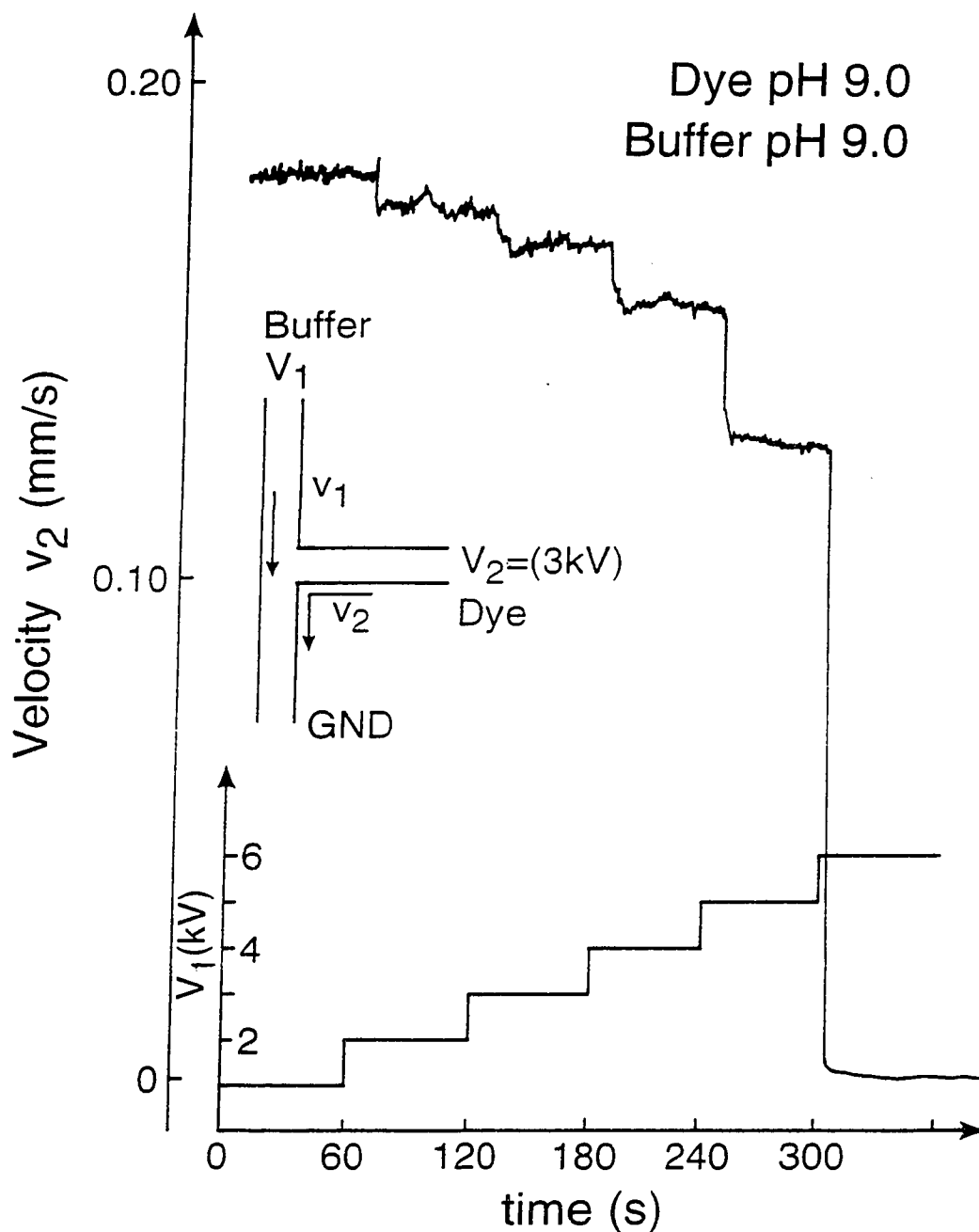


Figure 3-9 Measured dye velocity, v , in the side channel as a function of applied potential on the main channel. With same pH in the two channels, stable velocity profile was observed. (Side channel length was 40.0 mm, μ_{obs} was 1.84×10^{-5} and $2.58 \times 10^{-5} \text{ cm}^2/\text{V}\cdot\text{s}$ and μ_{eo} was 3.25×10^{-4} and $2.98 \times 10^{-4} \text{ cm}^2/\text{V}\cdot\text{s}$ for pH 9.0 and 8.6)

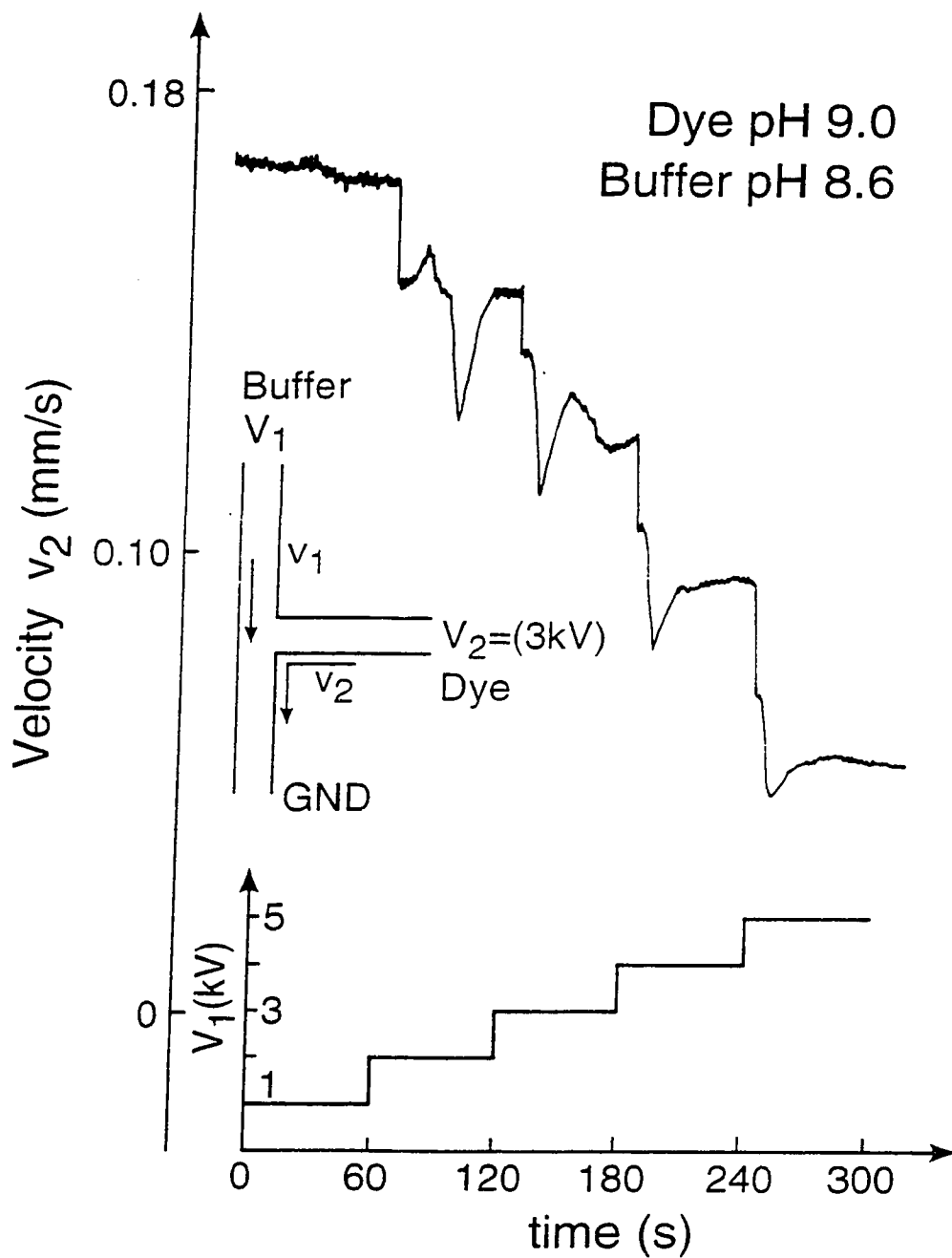


Figure 3-10 Measured dye velocity, v , in the side channel as a function of applied potential on the main channel. With differing pH values in the two channels, stabilization of times of 30 s were needed as the potential was varied. (Same device and conditions as Figure 3-9).

3.4.4. Flow “misbehavior”--no EOF

For some of the etched glass batches, we found the flow behavior was strange. In some of these devices for instance, when we prepared the channel with a 0.1 M NaOH flush for 15 minutes, followed by buffer conditioning at pH 9.0 for 15 minutes as our routine to start the experiment, we found that the flow of fluorescein reversed its direction after 1/2 hour. This strange phenomenon is due to rather low EOF in the devices, some of which gives a low overall mobility for fluorescein of $1.0 \times 10^{-6} \text{ cm}^2/\text{V}\cdot\text{sec}$, compared to a more typical value as $6 \times 10^{-5} \text{ cm}^2/\text{V}\cdot\text{sec}$ for my normal devices. In some cases we even observed flow of fluorescein in the opposite direction. To regenerate the glass surface, we flushed the channel with 1 M NaOH for 1 or 2 hours, and even employed 5 M NaOH flushing, but could only maintain a normal flow for about 1/2 hour. Comparing to the normal situation, we typically use much less concentrated NaOH to generate the surface before we use the devices, and they will last for a whole day without notable change of the overall mobility.

Noticing the phenomenon that the -2 charged fluorescein flowed in the direction of the anode in some devices, we performed the following study to look closely at how differently charged amino acids would behave in this situation. We chose two amino acids, arginine (arg) and phenylalanine (phe), both FITC labeled (Labeled compounds will be shown with “*” later in this chapter and the Chapter 4). With Tris/Boric buffer at pH 9.0, arg* should have a “-1” charge, and phe* should have “-3” charge on it, if we assume that FITC would have -2 charge at this pH value. Separation was followed by a

2-second-injection, and we recorded only an arg* peak at 13 seconds when 4 kV separation voltage was applied from anode to cathode in a device with poor fluorescein mobility. With the reversed polarity, we observed only the phe* peak at 12 seconds with the same electric field, but migrating towards the anode. From these observations, we believe that the EOF or μ_{eo} was low and close to the μ_{ep} of fluorescein, so the electroosmotic mobility had a profound influence on the direction of migration. Thus the -1 charged arg* would move with μ_{eo} to the cathode; while at the same time, -3 charged phe* migrate against μ_{eo} to the anode. In the normal situation, μ_{eo} is much higher so it would still carry -3 charged ions in the osmotic flow direction. We refer to this unusual phenomenon as “reversed flow”, since most of the analytes of interest are negatively charged due to fluorescein labeling, so under the circumstance of very low electroosmotic mobility, they will migrate to the opposite direction if we set our detector close to the cathode.

This “reversed flow” is due to “memory effects” (20) of the etched glass, which were treated or exposed to “harsh” conditions, arising from strong acid baths or contamination by metal ions. One of our device orders having “reversed” flow had experienced prolonged metal etch exposure in *aqua regia*. This strong acidic media exposure apparently resulted in severe changes in the glass surface chemistry which reduced EOF. This process seems irreversible, because EOF could only be recovered for a short period after basic treatment, and then it returned back to the previous very low EOF.

In another case when our glass devices had “reversed” flow behavior, this may have been caused by metal contamination, which could result in the change of the ion exchange properties on the glass wall (21). Marboe and Weyl noted in 1947 that wet glass brought into contact with iron and manganese acquired a brown stain. They found that contamination with iron was rapid, the stain becoming visible 10 minutes after the glass and iron are brought together (22). In our case, when the glass devices were immersed in a solution having polyvalent metal cations, ion exchange may have occurred. This situation occurred during fabrication when the etch bath was shared with others who had a large amount of metal ions released by their devices. Following this experience, we have required fresh etch solutions to ensure no contamination.

3.5 Conclusion

In this chapter, we discussed how subtle effects will affect the flow and mixing behavior at the intersections. The composition of the solvent being mixed can influence the flow velocity due to the imbalanced ζ potential within the system. When there is an imbalance in solvent pH at two intersecting channels, there will be a difference in ζ potential in each channel. This will result in an additional Poiseuille flow added to the electrokinetic flow. The effect of this Poiseuille flow is profound. The measured velocity can be very different from the EOF velocity predicted considering electrokinetic effects alone.

Mixing is also affected if the solvents from two streams having different pH. The velocity trace shows unstable flow profiles with slow oscillations. This instability is caused by the imbalance of ζ potential. It took about 30 seconds for the leading edge of the mixed solution to migrate through the length of the downstream channel, which is close to the time frame of slow oscillation we observed in the velocity profiles.

“Reversed” flow direction was observed when the devices had been treated with harsh acidic solution or immersed in solution contaminated by metal cations. These treatments caused permanent change to the hydroxyl layer on the wall surface which generates EOF. When there is very small EOF in the electrokinetic driven flow, the electrophoretic mobility will be dominant in deciding the analyte flow direction. Most of our analytes of interest are negatively charged, so they may flow in the opposite direction to the condition where we have normal EOF.

References

- 1 Camilleri, P., in Camilleri, P.(Editor), *Capillary Electrophoresis: Theory and Practice*, CRC Press, Boca Raton, **1993**, Ch. 1
- 2 Sepaniak, M.J.; Powell, A.C.; Swaile, D.F.; Cole, R.O., in Grossman P.D. and Colburn, J.C. (Editors), *Capillary Electrophoresis: Theory and Practice*, Academic Press, Inc., San Diego, **1992**, ch. 6
- 3 Kuhr, W.G.; Monning, C.A., *Anal. Chem.*, **64**, 389R-407R, **1992**
- 4 Keely, C.A.; van de Goor, T.A.; McManigill, D., *Anal. Chem.*, **66**, 4236-4242, **1994**
- 5 Reijenga, J.C.; Kenndler, E., *J. Chromatogr. A*, **659**, 403-415, **1994**
- 6 Reijenga, J.C.; Kenndler, E., *J. Chromatogr. A*, **659**, 417-426, **1994**
- 7 Cifuentes, A; Poope, H., *Electrophoresis*, **16**, 516-524, **1995**
- 8 Tavares, M.F.; McGuffin, V.L., *Anal. Chem.*, **67**, 3687-3696, **1995**
- 9 Spitzer, J.J.; Danielson, L.J.; Hepler, L.G., *Colloids and Surfaces*, **3**, 321-328, **1981**
- 10 Martin, M.; Guiochon, G., *Anal. Chem.*, **56**, 614-620, **1984**
- 11 Martin, M.; Guiochon, G.; Walbroehl, Y.; Jorgenson, J.W., *Anal. Chem.*, **57**, 561-563, **1985**
- 12 Rice, C.L.; Whitehead, R., *J. Phys. Chem.*, **69**, 4017-4024, **1965**
- 13 Chien, R-L.; Helmer, J.C., *Anal. Chem.*, **63**, 1354-1361, **1991**
- 14 Qiu, X.C.; Harrison, D.J., *Transducers'97, 1997 International Conference on Solid-State Sensors and Actuators*, 923-926, **1997**
- 15 Bello, M.S.; Capilli, L.; Righetti, P.G., *J. Chromatogr. A*, **684**, 311-322, **1994**
- 16 Hu, L., *Master Thesis*, University of Alberta, **1997**
- 17 Harrison, D.J.; Fluri, K.; Seiler, K., Fan, Z., Effenhauser, C.S.; Manz, A., *Science*, **261**, 895-897, **1993**
- 18 Fluri, K.; Fitzpatrick, G.; Chiem, N.; Harrison, D.J., *Anal. Chem.*, **68**, 4285, **1996**
- 19 Manz, A.; Effenhauser, C.S.; Burggraf, N.; Harrison, D.J.; Seiler, K.; Fluri, K., *J. Micromech. Microeng.* **4**, 257, **1994**.

-
- 20 Lambert, W.J., Middleton, D.L., *Anal. Chem.*, 62, 1587-1591, **1990**
- 21 Virtanen, R., *Acta Polytechnica Scand.*, 123, 1-67, **1974**
- 22 Holland, L., *The Properties of Glass Surfaces*, JohnWilly & Son, **1964**

Chapter 4

Integrated Calibration with On-board Immunological Reaction

Abstract

A mixer was used to demonstrate that voltage controlled mixing and dilution can be achieved. The linear plot showed the signal intensity increased with the sample concentration introduced after mixing. With the knowledge of the voltage controlled mixing, the immunoreactor was used to demonstrate an on-board reaction of antigen and antibody. With the varying voltages applied to the antibody and buffer reservoirs, the concentration of the antibody can be adjusted to make an on-board calibration. The calibration curve showed the complex signal increased linearly with the antibody amount introduced to the mixing coil. The calibration curve was tested with the known concentration samples, and a sample carryover study was performed.

4.1 Introduction

It is sometimes a complicated, time and labor consuming process to prepare an analyte for immunoassay manually. It would be very useful to achieve the whole procedure within the microfabricated chip, integrating the mixing, reaction, labeling, separation and detection steps on a single glass chip (1,4,5,6). For immunoassay, there is always a need to build a calibration curve for analyte quantification. The traditional way is to manually prepare a series of samples of different concentrations by taking a series of aliquots and physically diluting each one to a different concentration. The purpose of this study is to demonstrate that a series of calibration solutions can be prepared on-chip in order to provide a calibration curve. We intend here to achieve on-chip mixing and dilution to reduce the work involved in preparation of different samples, and reduce the possibility of experimental error. At the same time we can reduce the reagent amount demanded for the preparation of a series of standard solutions.

We used a glass device that was designed to introduce an antibody standard, mix it with different amounts of buffer to give various concentrations, then react it with a fixed, known amount of reagent. The device has two mixing junctions. Before the first junction, the amounts of standard and diluting buffer can be mixed using controlling voltages applied to the standard and buffer reservoirs. When this diluted standard solution reaches the second junction, it mixes and reacts with the labeled antigen, which is introduced in a fixed concentration. The reaction coil after the second

junction is relatively long, to ensure the reaction goes to completion during the migration period. This reacted product, as well as the excess of the labeled antigen, is then injected at the intersection between the injection channel and the separation channel. When the system is switched to separation, this sample plug moves down the channel and is separated. It is detected with a fluorescence detector which is located downstream 6 cm from the injector. For the assay studied, the signal measured is linearly proportional to the concentration of the standard that is mixed and reacted with the fixed amount of the labeled antigen. A calibration curve can be built on-line by mixing a series of standards with different concentrations at the first junction. This on-chip mixing and dilution capability could be useful for applications where one is sample limited, or when one is reagent limited. Examples of these cases are drug screening or some clinical measurements for the former, or applications out in the field for the latter.

4.2 Theoretical Calculation

When two streams meet each other, and flow to a third direction, which is represented by the schematic diagram shown in Figure 4-1, we can calculate the voltage at the intersection, namely the junction voltage (V_J). With potentials applied to the solvent reservoirs of all three channels, these three intersecting channels can be modeled as a simple network of three resistors (1). We assign the voltages applied to the reservoirs 1 & 2 as V_1 & V_2 , with each reservoir containing the chemicals to be mixed. We apply a ground voltage (V_3) to reservoir 3, which is the mixing waste, and we refer to the voltage at the intersection of the three channels as junction voltage, V_J . We can convert the known length of each channel to a relative resistance R , which is proportional to the length of a standard cross sectional area (2). Using Kirchhoff's rules (3) and solving for V_J , we come to the following Equation 4-1

$$V_J = \frac{V_1 R_2 R_3 + V_2 R_1 R_3}{R_1 R_2 + R_2 R_3 + R_1 R_3} \quad 4-1$$

This kind of analysis was first used and published by Seiler et al. in this research group (1).

In an electrophoretic system, the flow velocity can be calculated with the Equation 4-2:

$$v = \mu_{obs} E = \mu_{obs} \frac{V}{L} \quad 4-2$$

where v is the observed flow velocity, μ_{obs} is the observed mobility, E is the applied electric field, V is the voltage applied to the channel, and L is the channel length.

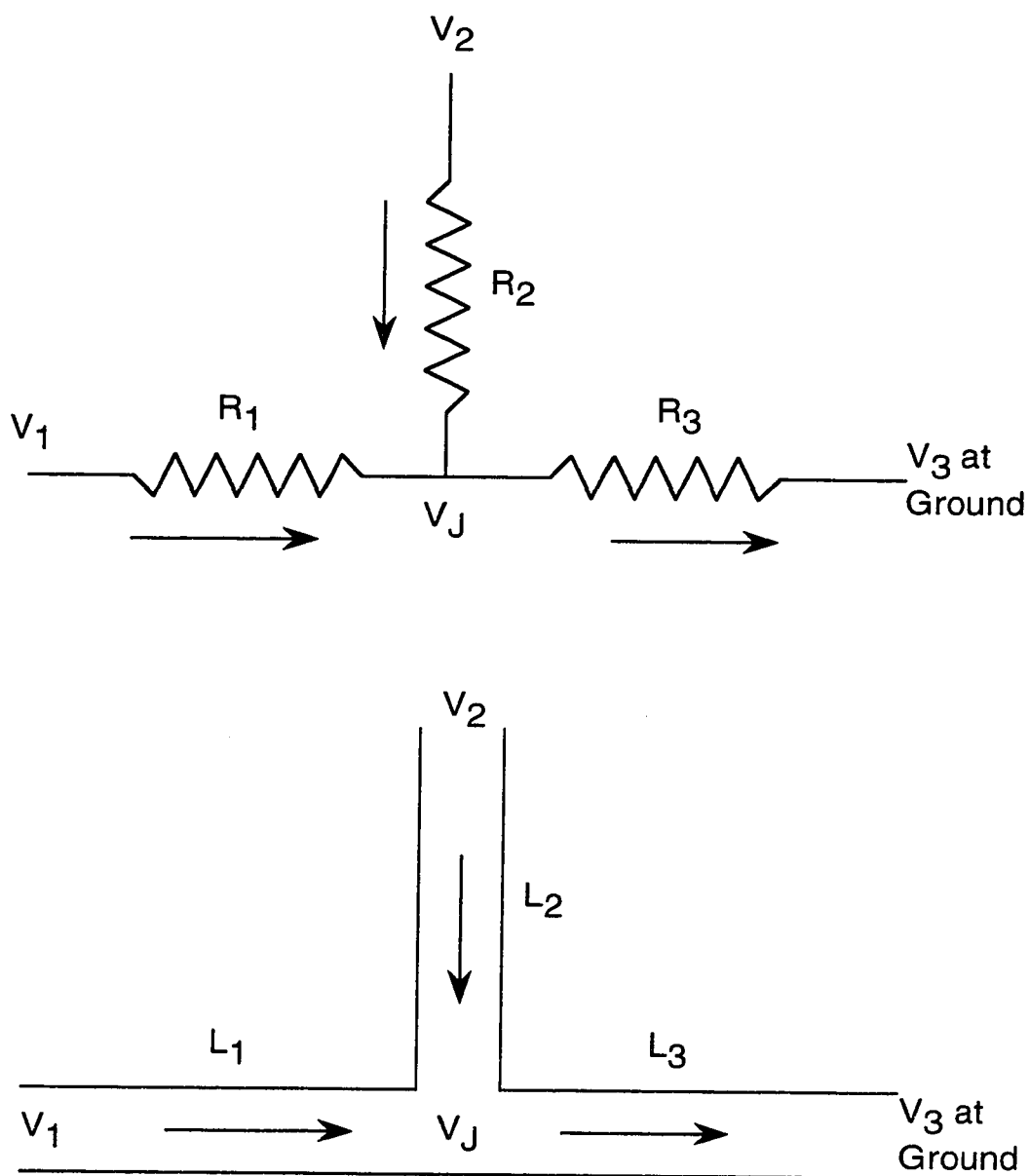


Figure 4-1 Schematic layout of mixing channels showing two reagents coming from two reservoirs 1 and 2 to meet at the intersection and flow to a third reservoir 3. The voltages from reservoirs 1 and 2 are V_1 and V_2 . V_J is the junction voltage at the intersection.

If the electroosmotic mobility is identical in all of the channels, and the two mixing channels have the same lengths and the same cross-sectional areas, then the velocities of the flow from the two channels are proportional to the voltages applied across or along each channel. In other words, the volumes introduced from the two mixing reservoirs to the intersection are proportional to the voltages applied there. Accordingly, we can represent the mixing ratio of the volumes with the applied electric field, as shown in Equation 4-3:

$$\frac{Volume1}{Volume2} = \frac{V_1 - V_J}{V_2 - V_J} \quad 4-3$$

Where *Volume1* and *Volume2* are the volumes introduced from the channels 1 and 2, V_1 and V_2 are the voltages applied to the reservoirs 1 and 2, and V_J is the junction voltage that can be calculated with the Equation 4-1.

Another important equation leading to the concentration after mixing involves the law of mass conservation, which says that the number of moles of a solute is a constant before and after mixing/dilution. This is expressed as Equation 4-4:

$$M_b V_b = M_a V_a \quad 4-4$$

where M_b and M_a are the molarities before and after dilution, and V_b and V_a are the volumes before and after dilution. Also, we know that $V_a = V_b + V_d$, where V_d is the volume from the dilution process. We can then rewrite Equation 4-4, and replace the volumes with volume ratios, which can be related to the electric field ratios, as shown in Equation 4-5:

$$M_a = M_b \frac{V_b}{V_a} = M_b \frac{V_b}{V_b + V_d} = M_b \frac{V_b / V_d}{(V_b / V_d) + 1} \quad 4-5$$

From the previous Equation 4-3, we can replace V_b/V_d with the ratio of applied potentials.

With these equations and conversions we can calculate the diluted concentration of our target standard after mixing, using the known values of the voltages applied between the two channels. In the following sections, we will show that experimentally we can achieve this voltage controlled mixing.

4.3 Experimental Section

4.3.1 Device fabrication

Glass devices (3 in. x 3 in.) were fabricated at the Alberta Microelectronics Centre, using microlithographic patterning and an HF/HNO₃ etchant, with a modified silicon micromachining technique (4,5,6). The substrates were 200 µm thick 0211 glass plates (Corning Glass Works, Corning NY). They were cleaned ultrasonically in detergent (5% Sparkleen, Fisher Scientific), methanol (Reagent Grade), and deionized water in an ultrasonic bath in a class 100 clean room environment. A process of photolithograph was followed as described elsewhere (4,5,6,7).

In this experiment, channels of 10 µm depth were etched on one glass plate. Both the etched glass and a cover plate with holes (1.5 mm) drilled with a diamond drill bit for external access, were cleaned as described above, followed by pressure wash using a Model 2066 High Pressure Cleaning Station (MicroAutomation, CA) under a class 100 clean hood. With careful alignment through the access holes to the etched channels, the cover plate is thermally bonded to the etched plate by heating at 595 °C for 6 hours.

4.3.2 Instrumentation

A modified computer-controlled power supply system (+3 kV, -3 kV and -15 kV, MJ Series, Glassman High Voltage, Whitehouse Station, NJ) with high voltage relays (30 kV Kilovac, Santa Barbara, CA) was used. It was based on the arrangement described previously (1,4). LabView programs (National Instruments, Austin, TX) written in-house were used for data acquisition and instrument control. Laser induced fluorescence detection was achieved using a 488 nm air-cooled argon ion laser (Uniphase/Ionics Model 2011) operating at 3.2 mW output to excite fluorescence, after focusing to about a 30 μm spot size in the device channel. Emission was collected with a 25x Leitz Fluotar objective (0.35 NA), then directed onto a Hamamatsu photomultiplier tube (PMT) after passing through an 800 μm pinhole located at the image plane of the lens. A 518 ± 15 nm optical band pass filter (Omega Optical, Brattleboro, VT) was used to eliminate scatter of the UV source, and to reduce background fluorescence from the 0211 glass. The PMT signal was filtered through an in-house built 25 Hz low-pass cut off frequency filter. The filtered signal was then recorded simultaneously on a strip chart recorder and a computer. The peak parameters, such as area and the number of theoretical plates, were calculated using statistical moments analysis (8,9) with the in-house written Labview programs (National Instruments Corp., Austin, TX).

4.3.3 Materials and reagents

Tricine, fluorescein isothiocyanate isomer I (FITC), arginine, fluorescein labeled bovine serum albumin (BSA*, 11.2:1 average fluorescein to BSA mole ratio, according to the supplier), and monoclonal anti-BSA in mouse ascites fluid were from Sigma (St. Louis, MO). Sodium chloride and sodium hydroxide were from BDH, and Tween 20 was from Aldrich (milwaukee, WI). All chemicals were reagent grade, and ultrapure water (Milli Q, Millipore) was used for all solution preparations.

A buffer of 50 mM tricine, 26 mM NaCl and 0.01% w/v Tween 20 was made and adjusted with NaOH to pH 8.0. FITC was dissolved in 95% acetone, 5 % Ultrapure water. Arginine stock solution was prepared in the buffer at 10.0 mM. FITC was diluted in buffer to 10.0 mM to give a stock solution, and it was stored in the dark at 4 °C. Antigen BSA* was prepared in Tricine buffer at 50 µg/ml. Monoclonal mouse IgG Anti BSA was diluted on-chip in the concentration range of 7-47 µg/ml.

Arginine was labeled with FITC in a manner similar to published works (10,11,12). 100 µL of stock 10.0 mM arginine solution was taken to react with 20.0 µL of stock 10.0 mM FITC solution, and working buffer was added to a total volume of 10.00 ml. For complete reaction, the solution was left overnight before analysis was performed. However, since the arginine was prepared in the tricine buffer, both arginine and tricine were labeled by FITC in this procedure. The concentrations resulting from this derivatizing process were 10.0 µM for arginine, 50.0 µM for the original tricine (but 50 mM tricine in total), and 2.0 µM for FITC. In the later discussion section, the major peak from FITC labeled tricine will be used for analysis. Since all of the FITC appears

to have reacted, the sum of labeled arginine and tricine peaks should be 2 μ M. At least 80-90% of this product appears to be tricine, based on the relative peak heights.

All reagents were introduced to the channels via syringe with either 0.22 μ m pore size microfilter (Millipore), or 0.45 μ m Micropure separators (Amicon, Oakville, Canada) for larger protein molecules in small volumes. Buffer was introduced at the beginning and flushed until all the channels were filled. Fine Pt wires with insulating sleeves were inserted into the reservoirs on the device to serve as electrodes.

4.3.4 Set-up and operation

4.3.4.1. Mixing/dilution of FITC-Arginine

The IACE device, as shown in Figure 4-2, was used for this entire work. This device was designed by N. Chiem in this research group, with dimension of 3 in. x 3 in. The detailed channel width and length information is listed in Table 4-1.

For the mixing/dilution work, the bottom layout of the IACE device was used as a mixing tester, as shown in Figure 4-3. One of the “V” shaped twin injection ports, reservoir #1, was filled with FITC labeled arginine; and the other, reservoir #2, with Tricine buffer. All other reservoirs had Tricine buffer in them. LabView program “IgG.1b.2-ports” was written for this experiment, wherein -6 kV was applied to the injection waste, reservoir #3, during the injection process, while Ground and a positive voltage ranging between 0-250 V, controlled the twin injectors, reservoirs #1 and #2. This voltage difference allows the mixing ratio of dye to buffer to vary between

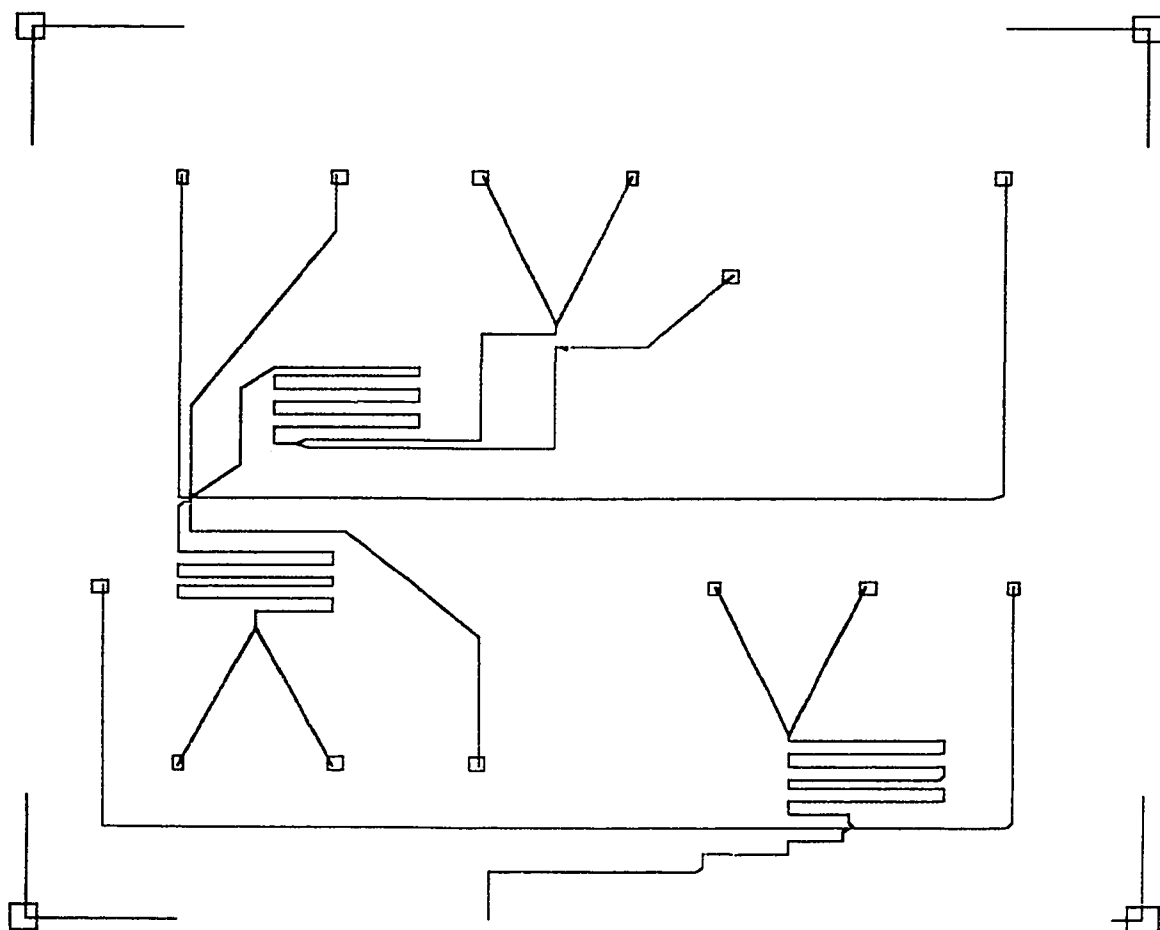


Figure 4-2 Channel layout of the device IACE. The top layout is the immunoreactor, while the bottom one serves as a mixing tester.

Table 4-1 Channel length and width of the device used.

Mixing tester (Channel layout shown in Figure 4-3)									
Channel	AC	BC	CD	DE	EF	GH			
width(μm)	90	90	26	26	210	26			
length(μm)	13	13	70	7	18	100			
equiv. length	3.51	3.51			3				
Immunoreactor (Channel layout shown in Figure 4-4)									
Channel	AC	BC	CF	DE	EF	FG	GH	JG	GK
width(μm)	90	90	26	210	26	26	210	210	26
length(μm)	13	13	25.5	14	25.5	83	36	27	80
equiv. length	3.51	3.51		1.72			4.42	3.4	

0.025 to 39.6, as illustrated in Table 4-2. From calculation, we know that it takes about 30 seconds for the fluids to reach the intersection, however, we chose to first run three consecutive injections for 60 seconds each, with 80 seconds separation period between each injection. This was done to ensure full mixing whenever we changed the mixing ratio. A series of 8 injection periods of 10 seconds each, with 80 seconds separation periods between them was then performed. Usually data was collected for the last five consecutive runs and averaged. For separation, Ground and -6 kV was applied to buffer and separation waste in reservoir #4 and #5, respectively. With this program, the voltages applied to the dye and buffer can be controlled and varied separately, therefore

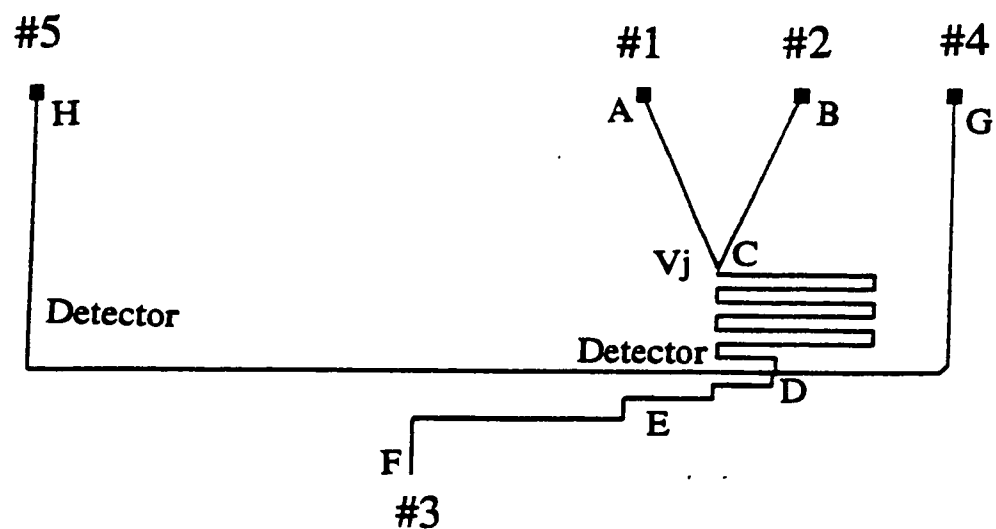


Figure 4-3 Detailed channel layout of mixing tester. Reservoir #1 and #2 forms the twin injector, where FITC labeled Arginine and diluting buffer were stored. Reservoir #3 is the injection waste, #4 and #5 are separation reservoir and separation waste. The positions of detector for mixing measurement and peak height analysis are indicated. V_j is the junction voltage.

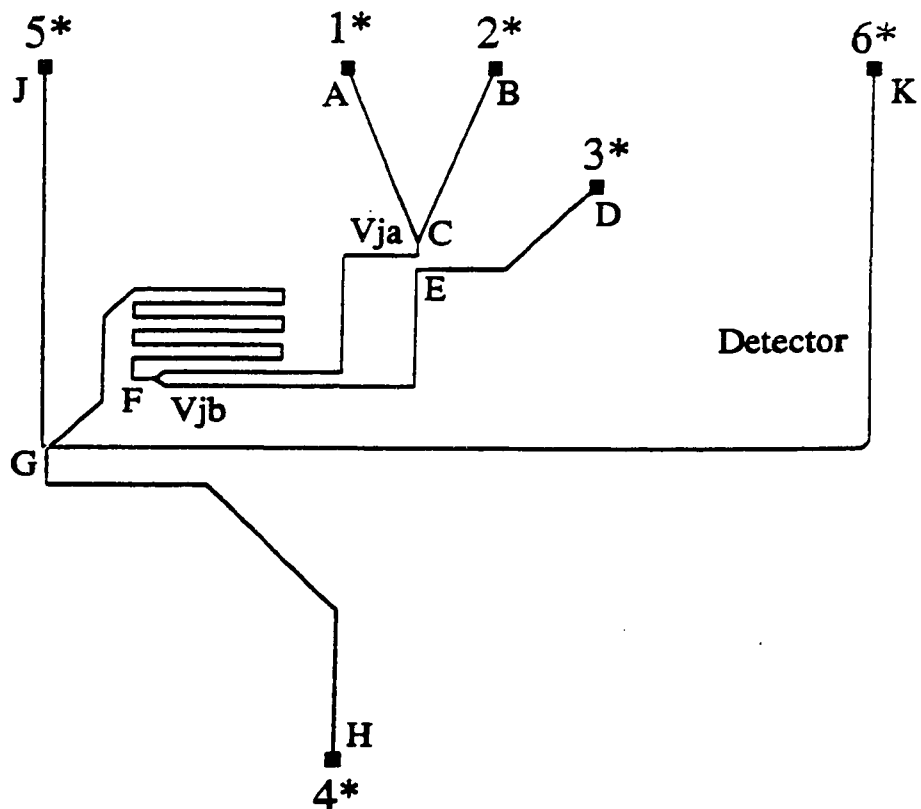


Figure 4-4 Detailed channel layout of immunoreactor. Reservoirs 1*, 2*, and 3* are three injectors, where antibody, diluting buffer and labeled Antigen were stored respectively. Reservoir 4* is the injection waste, 5* and 6* are separation reservoir and separation waste. Detector is located as indicated. V_{Ja} and V_{Jb} indicate the two positions for junction voltage. (See text for details)

the mixing ratio of dye to buffer can be adjusted as required and the dye intensity detected will be varied accordingly.

Table 4-2 Relation between applied voltage and mixing ratio.

$V_3(V)$	$V_1(V)$	$V_2(V)$	$V_j(V)$	mixing ratio	FITC (μM)*	% stock sol'n
-6000	0	250	-6.5	0.025	0.049	0.025
	0	200	-30.9	0.118	0.210	0.105
	0	150	-55.4	0.258	0.410	0.205
	0	100	-79.9	0.437	0.608	0.304
	0	50	-104	0.674	0.805	0.403
	0	0	-129	1.0	1.00	0.500
	50	0	-104	1.48	1.19	0.597
	100	0	-79.9	2.25	1.38	0.692
	150	0	-55.4	3.71	1.58	0.788
	200	0	-30.9	7.46	1.76	0.882
	250	0	-6.5	39.6	1.95	0.975

* Calculated assuming 2 μM FITC in total.

In the mixing study, the detector was located either at the position after the mixing coil and just before the intersection of the injection and separation channels or else along the separation channel 50 mm from the injection point for peak height measurements. The intensity of the fluorescence signal was monitored and measured by PMT. The twin injectors both have equivalent channel lengths of 3.5 mm, while the mixing coil is very long, 80 mm, and the separation channel is 100 mm in length. When we varied the voltages applied to the twin injectors, we were varying the ratio of the amount of dye and buffer introduced to the mixing coil and thus the concentration of the dye at the detector. However, since the resistance of the mixing coil is very large, the total electric field, 600 V/cm, does not change in the mixing coil when the voltages applied to either of the “V” injectors changes within 250 V. In this case, the velocity inside the mixing channel remains constant, so that the intensity change is due to the concentration change only.

4.3.4.2. Integrated calibration of on-chip immunological reaction

The top layout of IACE, as shown in Figure 4-4, was in use as an immunoreactor. The reservoirs 1* and 2* were filled with Anti-BSA and Tricine buffer respectively, while reservoir 3* had FITC labeled BSA (BSA*) in it. All other reservoirs, 4*, 5* and 6* were filled with Tricine buffer. For injection, -6 kV was applied to the injection waste, reservoir 4*, while Ground was applied to reservoir 3* all the time. Reservoir 1* and 2* either had Ground or a positive voltage ranging from 0-100 V applied in turn, to allow a broad mixing ratio of Ab to buffer. With this voltage

range, the Ab to buffer ratio can be varied between 0.03-28.5, which is equal to 3-97% concentration of the stock Ab in reservoir 1*. As described previously, 60 seconds was used as injection times for the first three runs for fully mixing whenever the mixing ratio changed. Data was collected for the last five consecutive runs of a series of 8 runs, with injection times of 10 seconds. For separation, -6 kV was applied to the separation waste, reservoir 6*, while Ground was connected to the buffer reservoir 5*. All other reservoirs were filled with buffer and left floating. LabView program "IgG.1c.3-ports" was written for this experiment. With this program, the voltages applied to the anti-BSA and buffer reservoirs were controlled and varied, so the mixing could be adjusted, while a fixed amount of BSA* was introduced to the reaction coil for each assay. With the long mixing coil, 83 mm, the electric field, 600 V/cm, does not change when the voltage applied to the twin injectors vary within 100 V, so the measured intensity change is due to concentration change only.

4.4 Results and Discussions

4.4.1 Mixing/dilution of FITC-Arginine

4.4.1.1 Mixing measurement

This work was done with the mixing tester as shown in Figure 4-3. In this study, the detector was located 200 μm before the intersection of the injection and separation channels. Even when the mixing voltages were changed, their contribution to the electric field in the long mixing channel and at the detector was negligible, because the resistance of the injecting channel before the mixing coil was so low. As a result, the velocity at the detector remained constant, so that the intensity changes observed were due to the concentration change only, not to velocity changes. We changed the voltage difference between the twin injectors, reservoirs #1 and #2, and monitored the fluorescence intensity of FITC labeled arginine as a function of the control voltages. As shown in Figure 4-5, the plot of intensity versus voltage is linear. A slope of 11.7 ± 0.1 and an intercept of 2963.6 ± 48.2 and r^2 of 0.9983 was obtained. With the known length of each channel, we can use Equation 4-1 to calculate the junction voltage, V_J . Then using Equation 4-3 and Equation 4-5, we can convert the voltages applied to reservoirs #1 and #2 to the concentrations after mixing/diluting. In this way, we can calculate the dye concentration under different controlling voltages. A plot of fluorescence intensity versus dye concentration is shown in Figure 4-6. A slope of 2978.7 ± 41.8 and an intercept of 1.97 ± 48.8 and r^2 of 0.9968 were obtained.

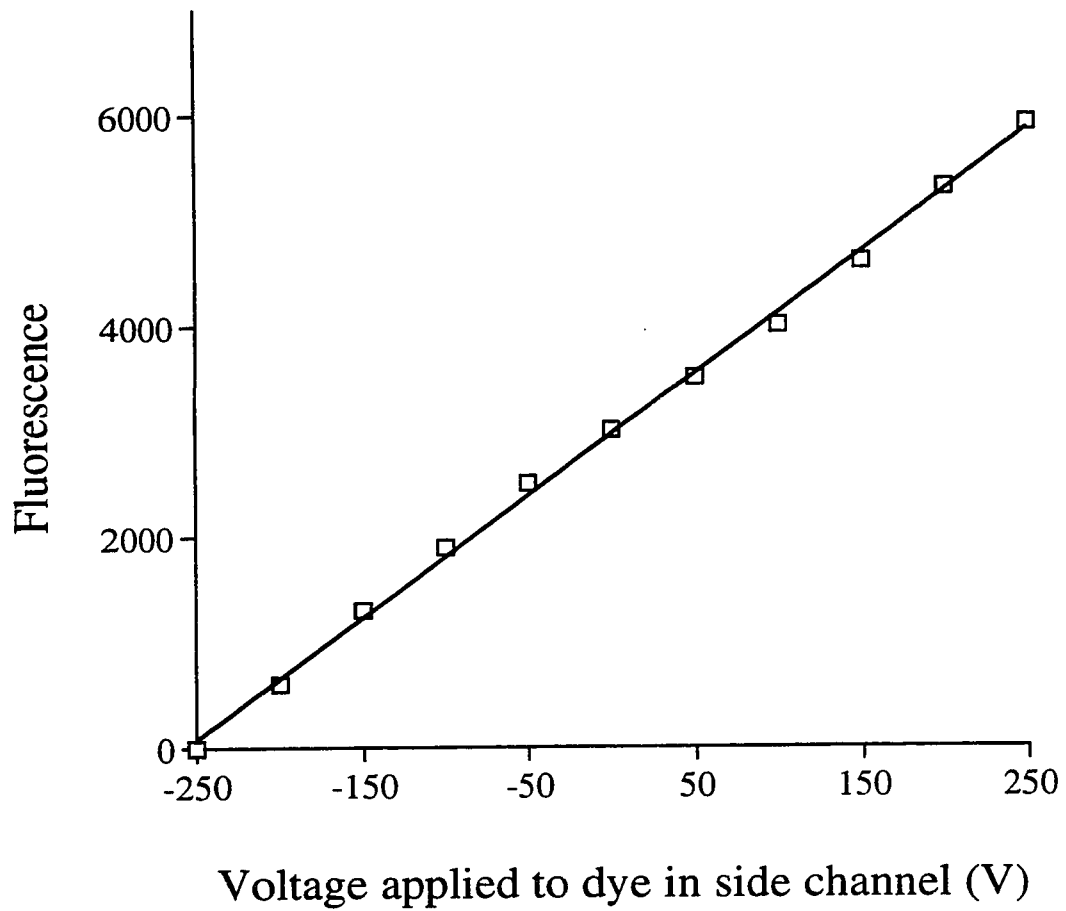


Figure 4-5 The linear response of intensity as a function of the relative voltage applied to the dye reservoir compared to the constant Ground voltage applied the buffer reservoir.

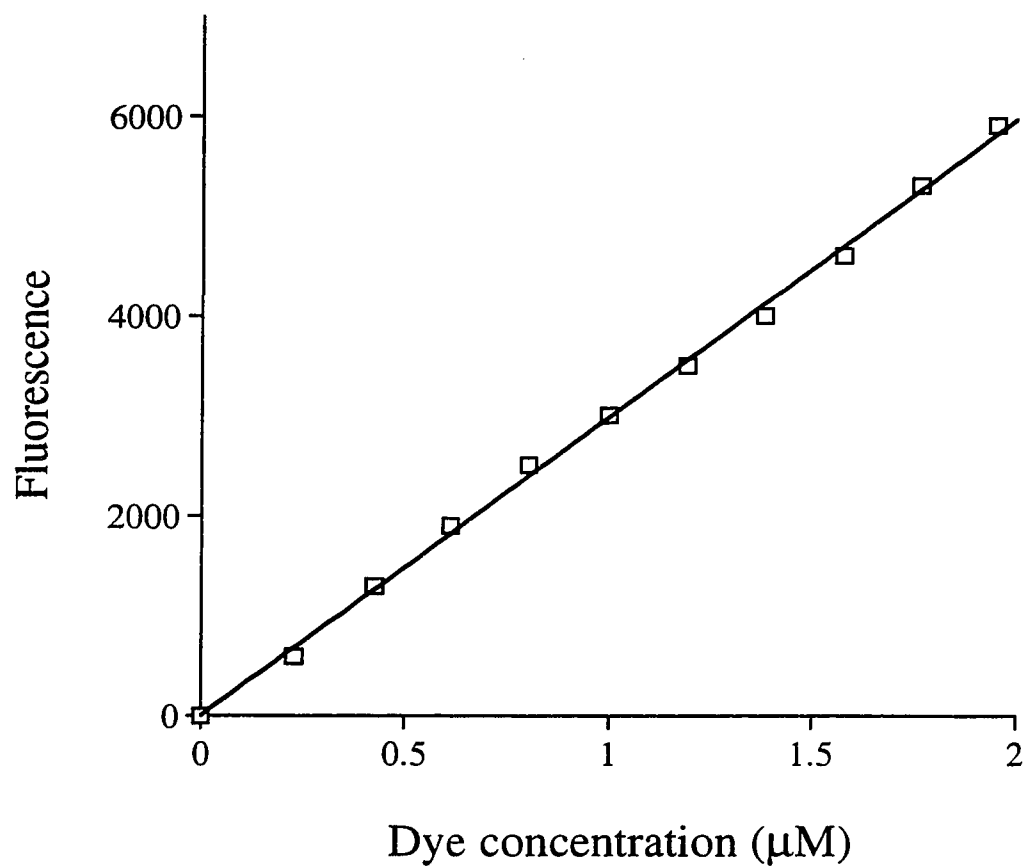


Figure 4-6 The converted response of intensity vs. concentration of the dye.

This study showed that we can change sample concentration with the voltage difference applied to the sample and buffer reservoirs. This shows that we can achieve the desired sample concentrations with controlling the electric fields applied to mixing reservoirs.

4.4.1.2 Peak height/area change with concentration

This work was also done with the mixing tester as shown in Figure 4-3. In this study, the detector was located along the separation channel 50 mm from the intersection where the sample plug was injected. As before, if the voltage applied to the twin injectors is changed, the concentration of the dye will change, so we expect a change in peak height or area after injection and separation. The serial plots in Figure 4-7 and Figure 4-8 show the effects of increasing voltage of the buffer or dye reservoirs, respectively. As seen in Figure 4-7, when the voltage applied to the buffer was increased while the voltage applied to the dye remained at ground the peak height decreased. This is because the dye concentration after mixing was decreased by increasing the amount of buffer delivered. Similarly, as shown in Figure 4-8, peak height increased when the voltage applied to the dye was increased and the voltage applied to the buffer remained at ground. This was due to the higher amount of dye introduced into the mixing coil. Plots of signal versus calculated concentrations were linear, as shown in the Figure 4-9, with a slope of 168.9 ± 4.9 and an intercept of 32.4 ± 28.9 , and r^2 of 0.992. The calculated concentrations were determined from the applied voltages and the mixing ratio using Equation 4-3 and Equation 4-5. These results

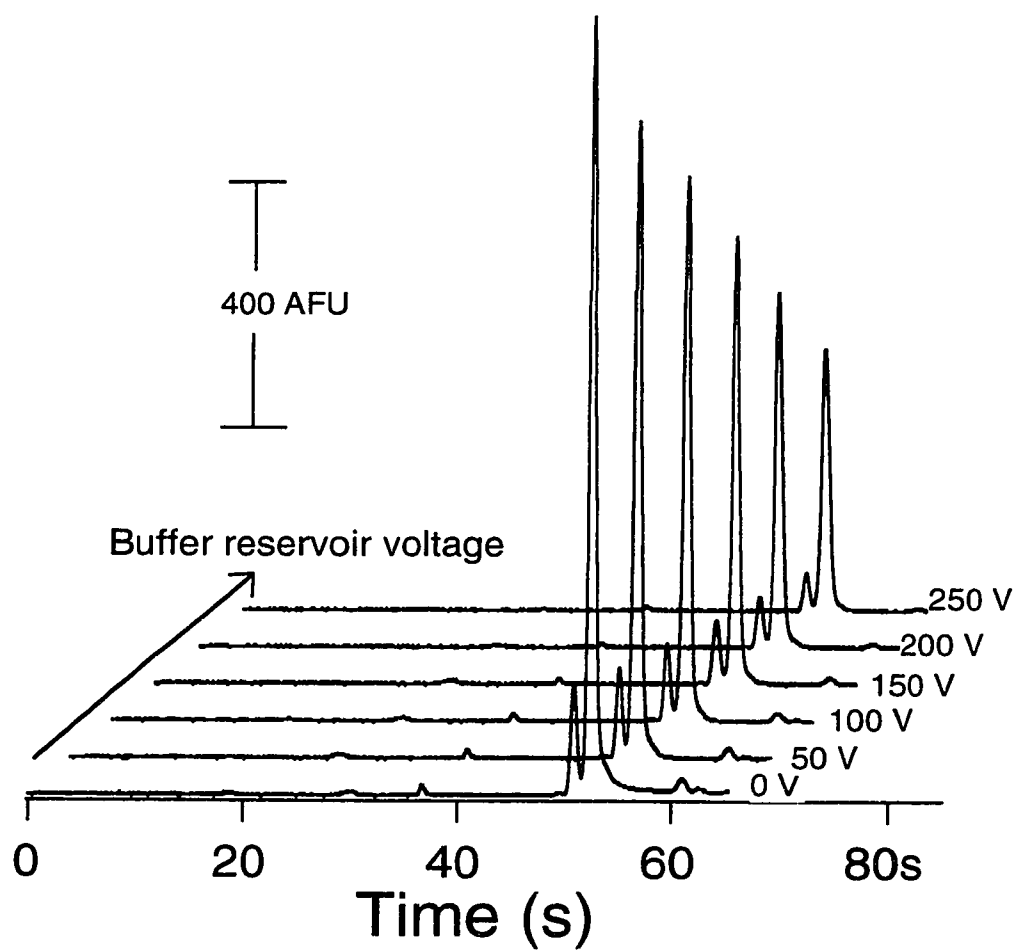


Figure 4-7 The series of electrophoregram showing the signal intensity decreasing with the buffer reservoir voltage increase.

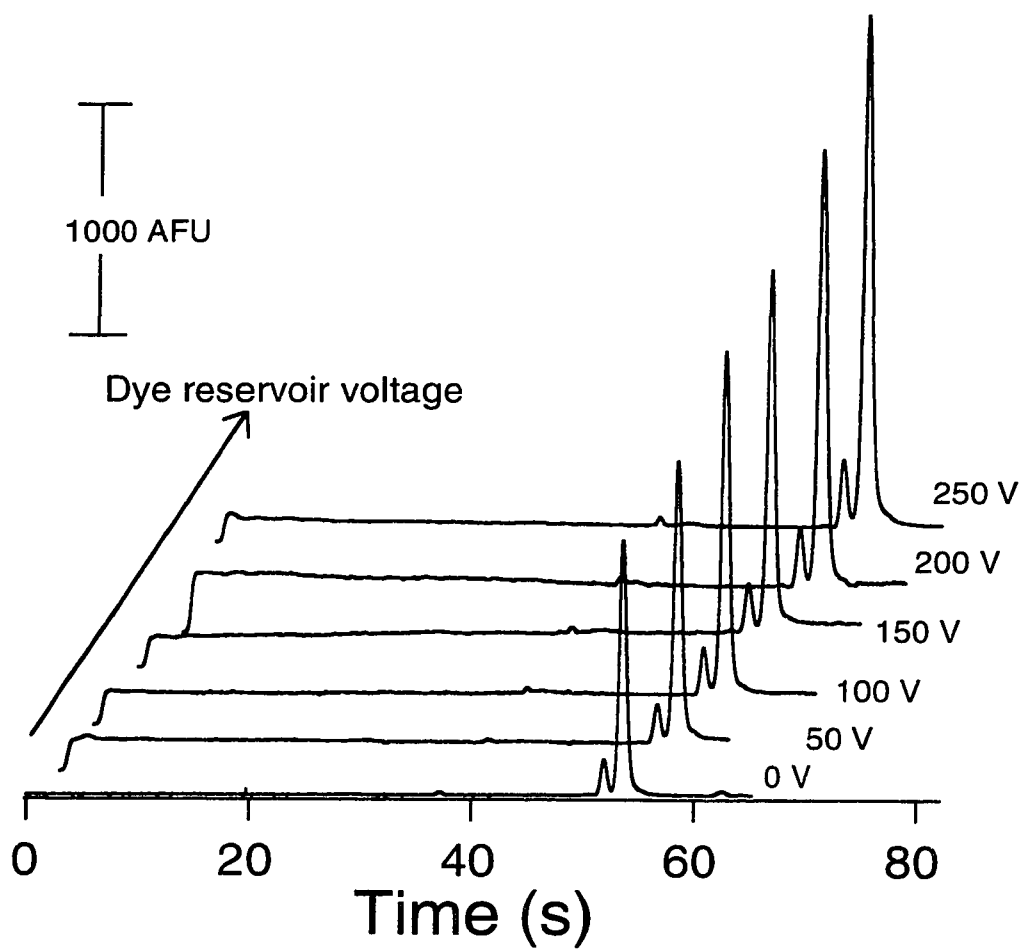


Figure 4-8 The series of electrophoregram showing the signal intensity increasing with the dye reservoir voltage increase.

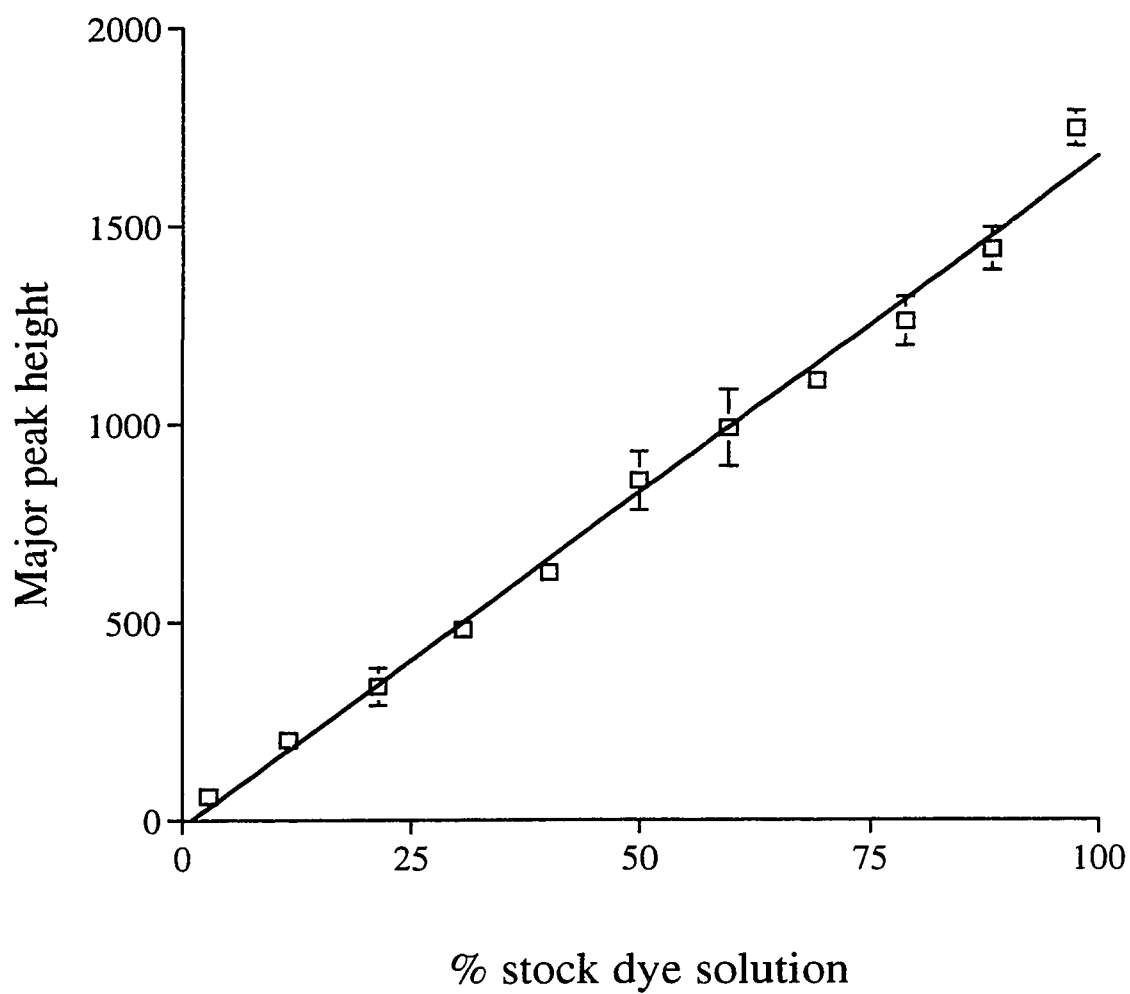


Figure 4-9 Calibration curve showing peak height for major dye peak vs. % of stock FITC solution ($2\mu\text{M}$) from the series of electrophoregram in Figure 4-7 and Figure 4-8.

indicate that voltage differences applied to the two mixing reservoirs had a linear relationship to the concentration generated after mixing, which was predicted by the theoretical calculations (13). Knowing that we can control the mixing of two reagents by applying different voltages to them, we can extend this work to on-line calibration, controlling the voltages of two or more different reagents to achieve the concentration variation of a single standard solution to generate a series for the calibration curve.

4.4.2 Integrated calibration of on-chip immunological reaction

4.4.2.1 Calibration curve

All the work for Section 4.4.2 and 4.4.3 was performed with the immunoreactor as shown in Figure 4-4. An on-chip immunoreaction was performed, followed by the separation of the reaction product, the complex of BSA* and anti-BSA, from the remaining free BSA*. The top trace shown in Figure 4-10 is the trace from BSA* alone. In this case, -6 kV was applied to reservoir 4*, 0 V to reservoir 3* and all other reservoirs were kept floating, so only BSA* was introduced to the system during injection. The bottom trace shows the separation of complex from free BSA*, where -6 kV was applied to the injection waste reservoir 4*, and both reservoirs 1* and 3* were connected to 0 Volt. In this case, both BSA* and anti-BSA were delivered to the reaction coil, allowing formation of the complex, as indicated by the additional peak. In this study, the total observed mobility of fluorescein was $2 \times 10^{-4} \text{ cm}^2/\text{V} \cdot \text{Sec}$, BSA* was introduced at 50 $\mu\text{g}/\text{ml}$, and for the bottom trace, the anti-BSA was at 20.2 $\mu\text{g}/\text{ml}$

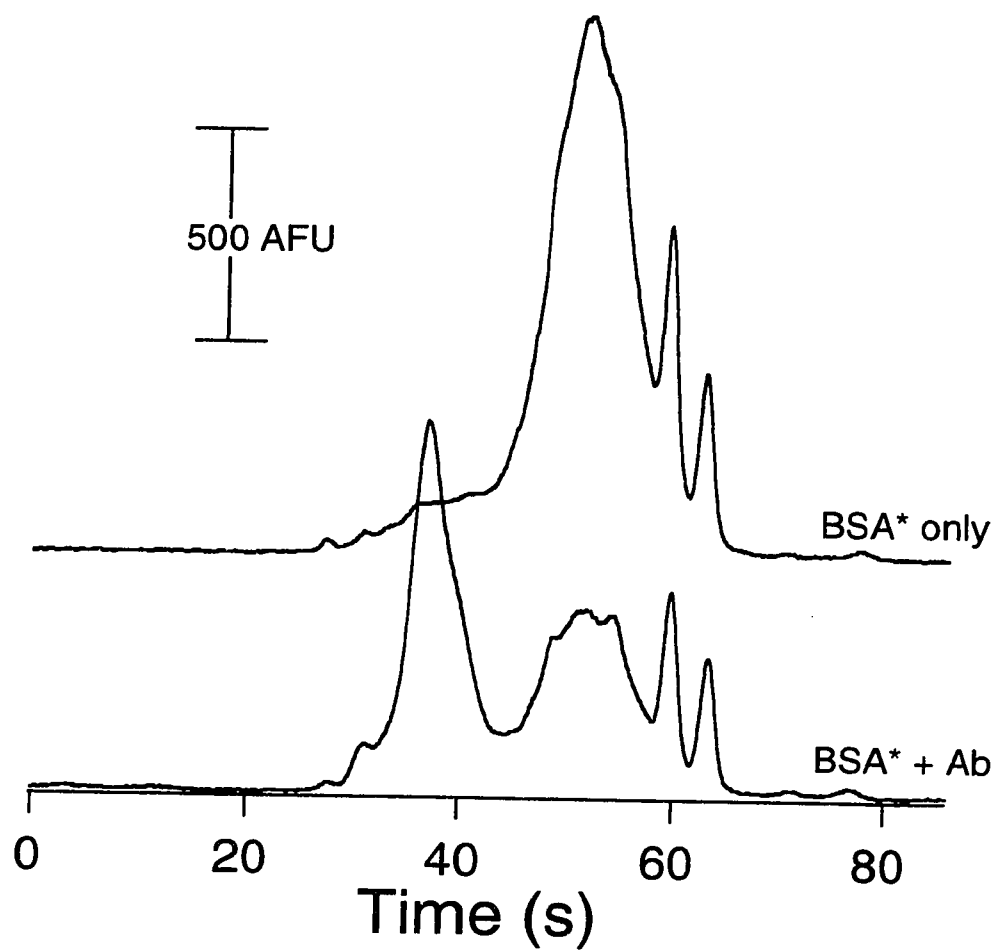


Figure 4-10 On-chip reaction. The top trace is from BSA* alone, the bottom one shows an additional complex peak when Antibody was introduced.

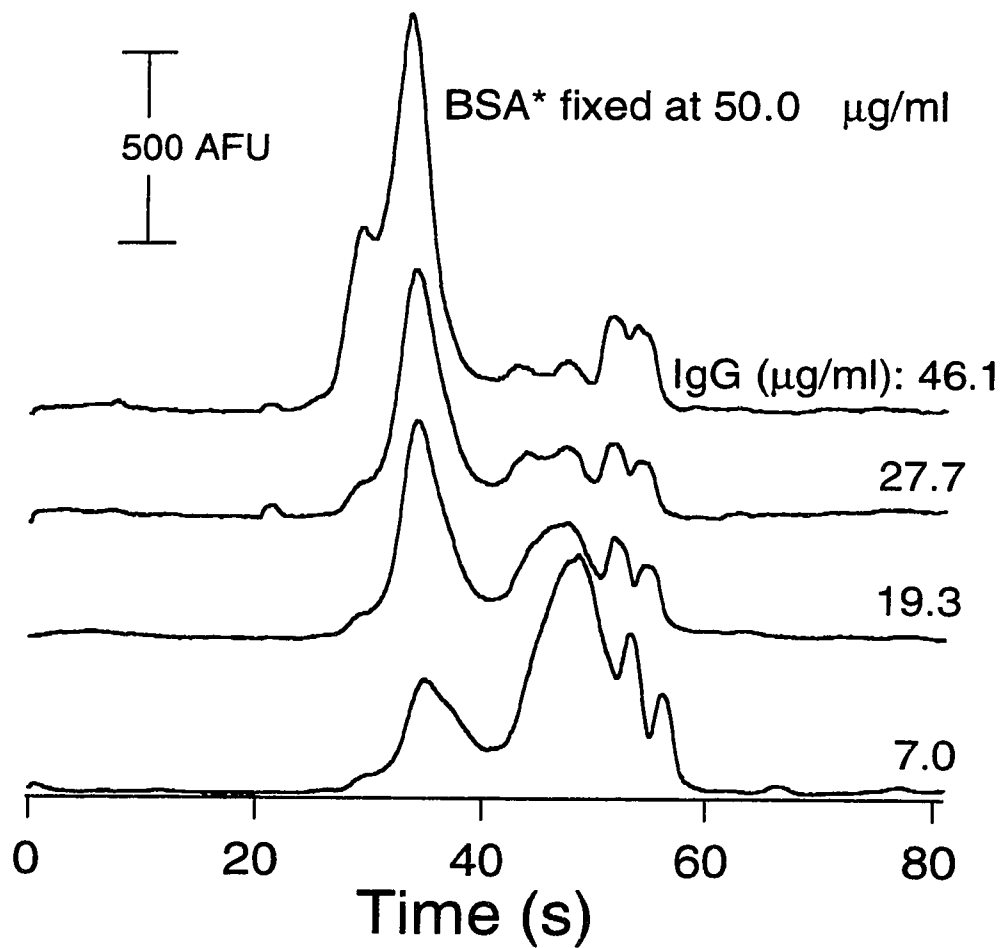


Figure 4-11 Selected traces from on-board calibration series showing the intensity change as a function of anti-BSA delivered. With the increasing amount of IgG introduced, the complex intensity increased, while the free BSA* intensity decreased.

before mixing with BSA*. This experiment demonstrates that we can introduce different reagent streams within our device and perform an integrated process of sample/reagent delivery, mixing, dilution, reaction, and separation on-chip.

To obtain on-board calibration curves with our immunoreactor, a series of different anti-BSA concentrations were delivered to the mixing coil by varying the voltages on reservoirs 1* and 2*, while the amount of BSA* introduced was fixed. In Figure 4-11, we fixed the amount of BSA* at 50 $\mu\text{g/ml}$, and varied the amount of anti-BSA from a monoclonal mouse IgG ascites fluid from 0-46 $\mu\text{g/ml}$. This was done by varying the potentials in order to change the ratio of anti-BSA and buffer. In the series of separations, we can see that the signal from the complex formed from BSA* and anti-BSA increased when we introduced more anti-BSA to the system. At the same time, the signal from free BSA* decreased due to the consumption of BSA*.

Concentrations of anti-BSA for the different mixing ratios were calculated based on the volume ratios of mixing of the anti-BSA and its dilution buffer. Knowing the length of the different parts of the channels, we can convert the lengths to the relevant resistances of the channels. With Equation 4-1, calculation for the voltage at the second junction, V_{jb} , was done as the first step. A potential of 0 Volt was applied to reservoirs 1*, 2*, and 3*, while -6 kV was applied to the injection waste, reservoir 4*. In this study we needed to maintain V_{jb} near constant to ensure that the same amount of BSA* was always introduced to the reaction coil. To calculate V_{jb} , we considered the channels from reservoirs 1* and 2* as a parallel resistance, and referred to its value as R_1 , with

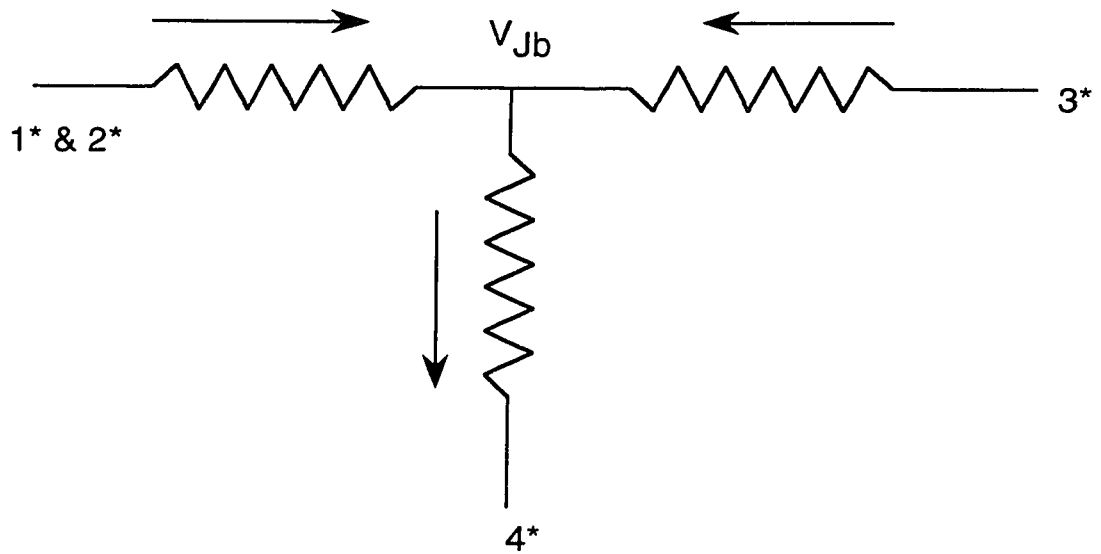


Figure 4-12 Labeling scheme identifying the channel resistances and lengths (R and l) by subscripts associated with the channel segment between intersection J_b and each of the reservoirs.

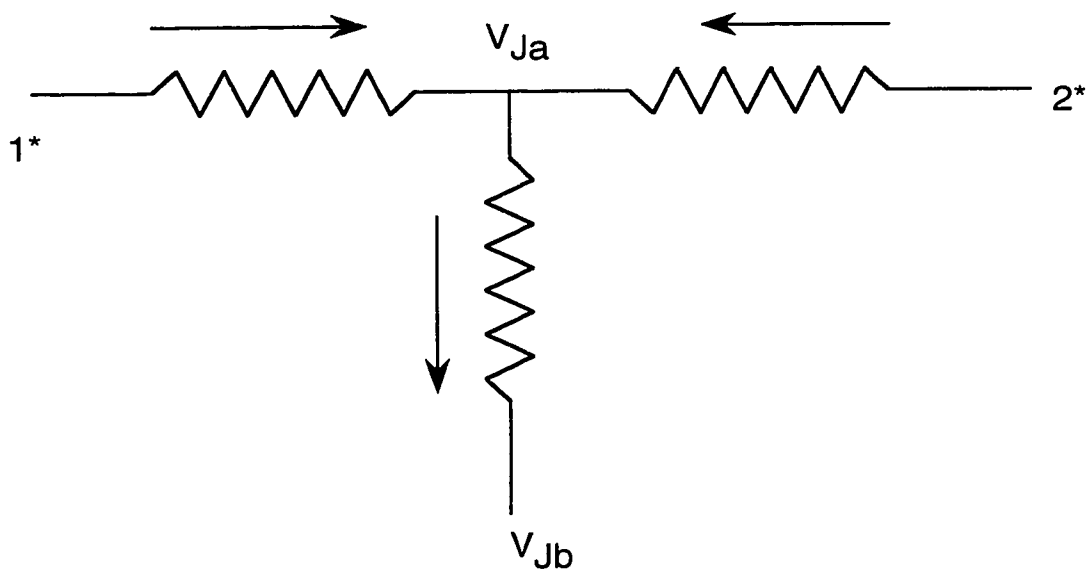


Figure 4-13 Labeling scheme identifying the channel resistances and lengths between intersection J_a and each of the reservoirs.

voltage V_1 applied to this parallel resistance. Meanwhile we took the channel from reservoir 3* as resistance R_2 , with voltage V_2 applied to it. R_3 is resistance from the channel after the junction V_{jb} , which includes the mixing coil and the channel to the reservoir 4*. The lengths used for R values can be found in Table 4-1. The diagram with all these configurations is shown in Figure 4-12.

Once the voltage for the second junction V_{jb} is known, we took this value as the voltage reference point, i.e. we took V_{jb} as Ground for the calculation of the first junction V_{ja} , and we assigned voltages V'_1 & V'_2 for the reservoirs 1* and 2* where the anti-BSA and buffer were introduced from. To maintain the second junction voltage V_{jb} close to constant, we can only vary V'_1 and V'_2 in a small range of 0-100 Volt. The diagram with these configurations is shown in Figure 4-13. Knowing the practical range of the voltages that can be used, we applied voltages to reservoirs 1*, 2*, 3* and 4* simultaneously. We took the ratio of $(V_1 - V_{ja}) / (V_2 - V_{ja})$ as the ratio of the volumes from anti-BSA and buffer for mixing/dilution, with the assumption that the mobility of the two streams is the same. This was illustrated by Equation 4-3. With the known dilution volumes, we can calculate the concentrations for anti-BSA to be mixed and reacted with BSA* at the second junction under the different electric fields, which is done with Equation 4-5. We used these calculated voltages to control each reservoir to carry out the on-board calibration study.

However, we noticed later that a commercial software was available that could perform this modeling. This software is MicroSim, which is a collection of electronic circuit design, simulation and analysis programs based on P-SPICE that are capable of

calculating and plotting the voltages and currents of a circuit easily and accurately. We utilized this software to cross check the calculations we made above by converting the channel lengths to equivalent resistances. We used the same R values which were converted from channel lengths that were listed in Table 4-1. The calculated results showing the accurate values of V_{Ja} , V_{Jb} , mixing ratio between anti-BSA and buffer, and the concentration of IgG introduced is illustrated in Table 4-3. This is the concentration of IgG after dilution in the channel section CF as indicated in Table 4-1. These results are close to our calculation using junction voltages, though our approximation of the constant value for the second junction V_{Jb} was the source of a 2% imprecision of the concentration of IgG introduced. For later analysis, we used the accurate values from MicroSim for estimating mixing ratio and the concentration of IgG.

Table 4-3 Applied voltage and resulting IgG introduced to reaction.

V1	V2	V4	V _{Ja}	V _{Jb}	mixing ratio	Stock %	IgG (μg/ml)
0	100	-6000	-3.63	-813.4	0.03	0.034	1.59
0	80		-13.28	-817.7	0.14	0.125	5.86
0	50		-27.44	-824.2	0.36	0.263	12.4
0	20		-42.22	-830.7	0.68	0.404	19.0
0	0		-51.86	-835.0	1.00	0.500	23.5
20	0		-42.22	-830.7	1.47	0.596	28.0
50	0		-27.74	-824.2	2.80	0.737	34.6
80	0		-13.28	-817.7	7.02	0.875	41.1
100	0		-3.63	-813.4	28.6	0.966	45.4

* Extra significant figures have been carried in this table to reduce round-off errors. No value is better than three significant figures.

Quantitatively, we plotted peak height versus concentration of anti-BSA to determine the linearity of the calibration curve. This plot, as shown in Figure 4-14, gave a linear increase for the complex peak, and a linear decrease for the BSA* peak as the antibody amount increased. A slope of 19.84 ± 0.97 and an intercept of 107.9 ± 27.7 , and r^2 of 0.9857 were obtained for the complex. This means we can change and control the amount of the reagent delivered to the system quantitatively using voltage controlled delivery. It also proves that the voltage control used in this experiment worked reliably, and that the original design of the immunoreactor functioned well with the calculated range of voltage/mixing ratios. We also plotted the signal intensity versus the IgG concentration after dilution with the BSA* solution, in order to eliminate the inaccuracy resulting from the electric field difference between junction J_a to J_b and reservoir 3* to J_b . This plot is shown as Figure 4-15. The electric fields, mixing ratio of anti-BSA to BSA* and reacted IgG concentrations are listed in Table 4-4. A slope of 38.8 ± 1.86 and an intercept of 111.29 ± 26.96 , and r^2 of 0.9863 were obtained from the complex.

Table 4-4 Reacted IgG concentration with dilution consideration.

Electric field (IgG) ($V_{ja}-V_{jb}$)/26.5	Electric field (BSA*) (V_3-V_{jb})/28.2	Dilution ratio	Diluted IgG ($\mu\text{g/ml}$)
30.56	28.85	0.514	0.818
30.36	29.00	0.511	3.00
30.06	29.23	0.507	6.27
29.75	29.46	0.502	9.55
29.55	29.61	0.500	11.7
29.75	29.46	0.502	14.1
30.06	29.23	0.507	17.6
30.36	29.00	0.511	21.0
30.56	28.85	0.514	23.4

* Extra significant figures have been carried in this table to reduce round-off errors. No value is better than three significant figures.

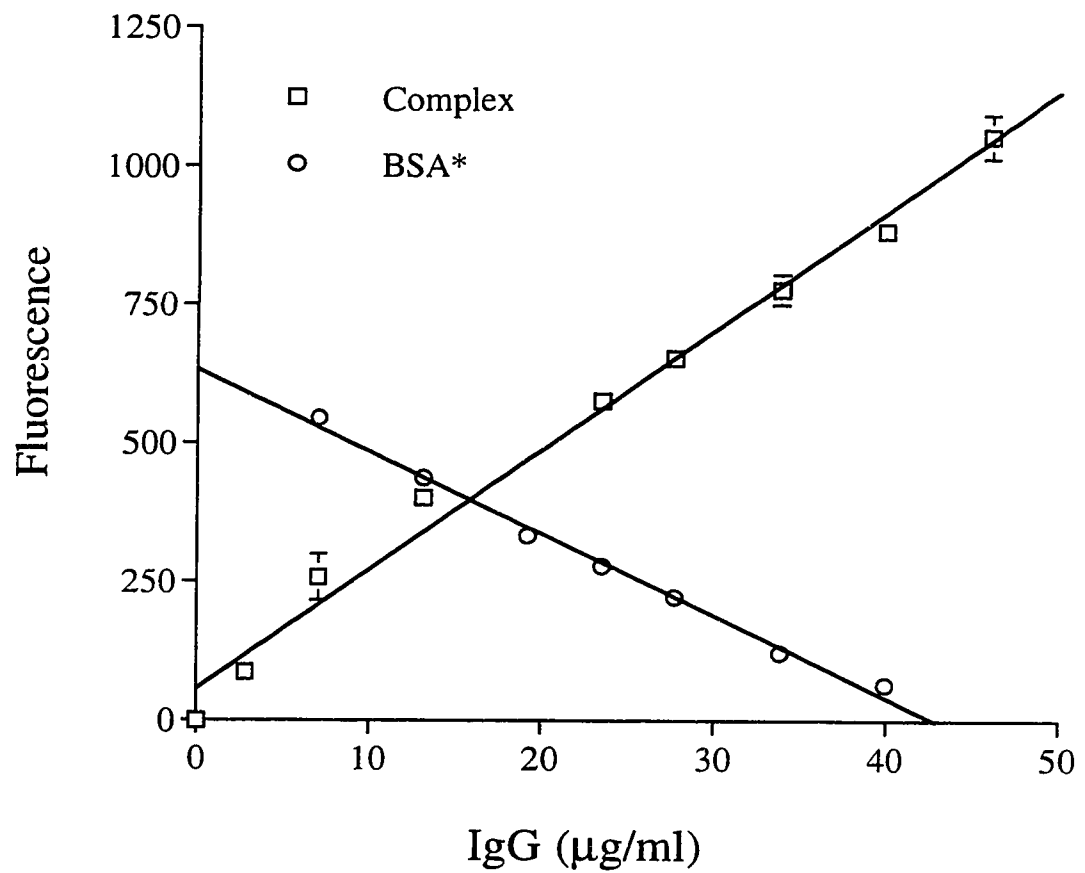


Figure 4-14 Calibration curve showing the complex fluorescence intensity increased with the increasing Antibody IgG amount. Meanwhile, the intensity from free BSA* decreased due to consumption (least square fit).

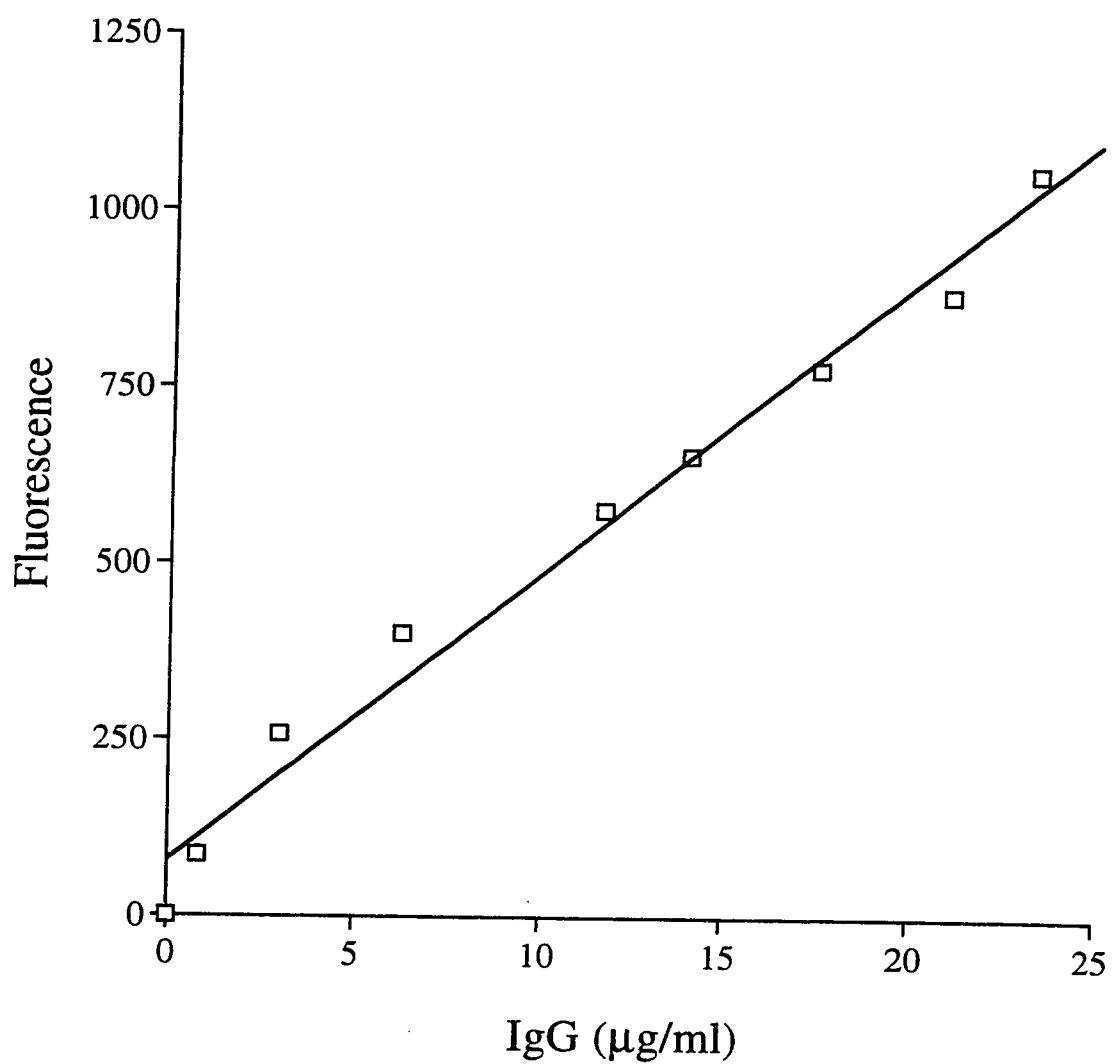


Figure 4-15 Calibration curve showing complex intensity increase and Free BSA* decrease with the increasing IgG concentration. Dilution effect from V_{jb} was considered (least square fit).

From the top trace for BSA* alone shown in Figure 4-10, we can see that there was background signal in the region before the major BSA* peak. This signal came out at the same migration time as the complex peak when we introduced anti-BSA. In early experiments we compensated for this by extrapolating the BSA* interference in the region of the complex peak. However, as more experience was gained the contribution of the background decreased and all data presented here are without modification. (The source improvement was not studied, but it was noted that the complex peak was sharper and stronger.)

4.4.2.2 Samples with known concentrations measured by the calibration curve

Three anti-BSA samples were diluted off-chip for comparison to the calibration curve. The concentrations were 11.75, 23.5, and 35.25 $\mu\text{g/ml}$. The concentration of the BSA* was the same as for the calibration curve, i.e. 50 $\mu\text{g/ml}$.

This “known concentration” sample experiment was performed on the same day as the calibration curve was obtained. Before introducing the sample, reservoirs 1*, 2* and 3* were filled with working buffer and carefully flushed for 5 minutes, to minimize the contamination from the anti-BSA. In the sample fitting study, BSA* was stored in reservoir 3*, just as in the calibration curve measurement, but sample was stored in both reservoirs 1* and 2*. To control sample delivery, we grounded all these 3 reservoirs, and applied -6000 volt to the sample waste reservoir, 4*. In this way, we eliminated the sample dilution step.

When introducing the known concentration anti-BSA samples, we started with the most diluted sample, and moved to higher concentration to minimize the contamination. With the signals of the complex from anti-BSA and BSA*, we determined the concentrations based on our calibration curve, as shown in Figure 4-14. The data is plotted in Figure 4-16, where the three circular dots were signals from the measured samples plotted against their known concentrations, while the rest were from the on-board calibration curve. In this plot, we can see that the known concentrations and their measured peak heights of the samples are in good agreement with the calibration curve. The standard deviation from the measured sample intensity is within the range of that of the calibration curve itself. The recovery of these three samples, calculated from 4 consecutive runs, is $102\pm 8\%$, $97\pm 6\%$ and $94\pm 4\%$ for the 11.75, 23.5 and 35.25 $\mu\text{g/ml}$ concentrations. Similarly, the sample signals are plotted on the calibration curve plot of Figure 4-15 against their known concentrations with the dilution by the BSA* solution taken into account, giving the results in Figure 4-17. The recovery is $101\pm 8\%$, $98\pm 6\%$ and $95\pm 4\%$ for 5.88, 11.75 and 17.63 $\mu\text{g/ml}$ reacted IgG concentration. This is a satisfactory result, which proves the possibility of our on-line calibration. This work shows that we can store calibrant and other reagents in our immunoreactor, and construct a calibration curve by on-board dilution through voltage controlled mixing. With the calibration curve, we can compare the measured signal of unknown sample to the calibration to determine its concentration.

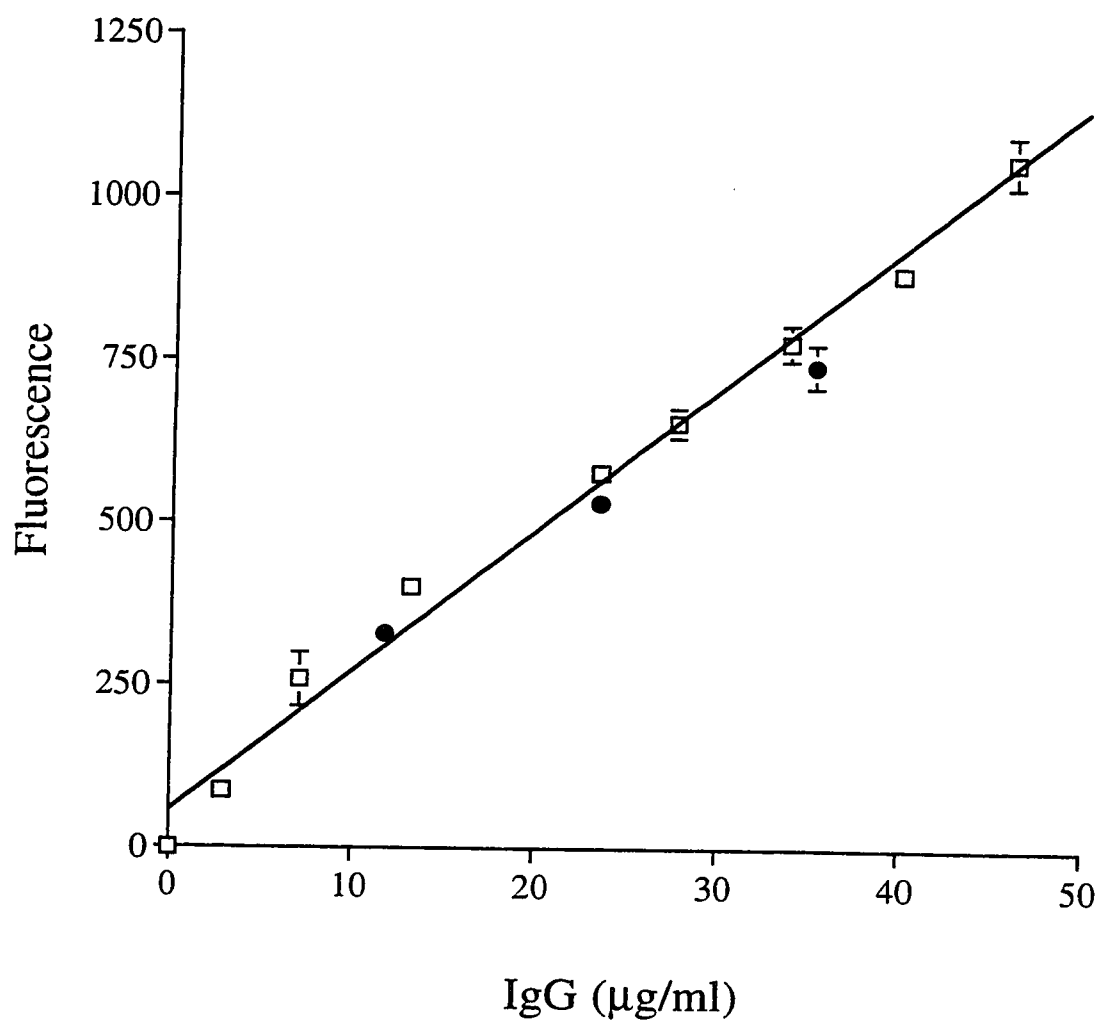


Figure 4-16 Known concentration samples were in good agreement with the calibration curve.

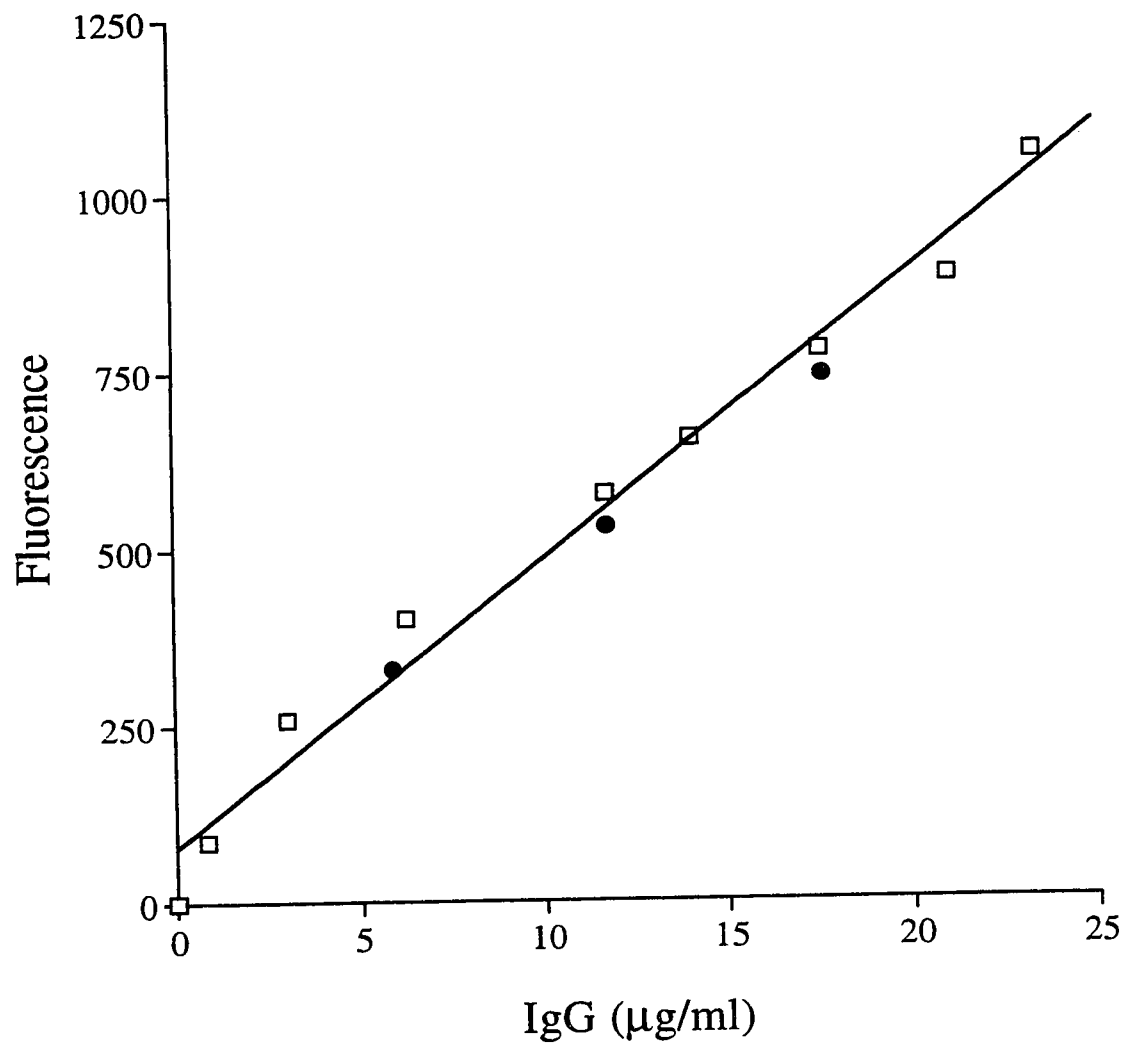


Figure 4-17 Known concentration samples on the calibration curve. Dilution from the junction V_{Jb} was considered.

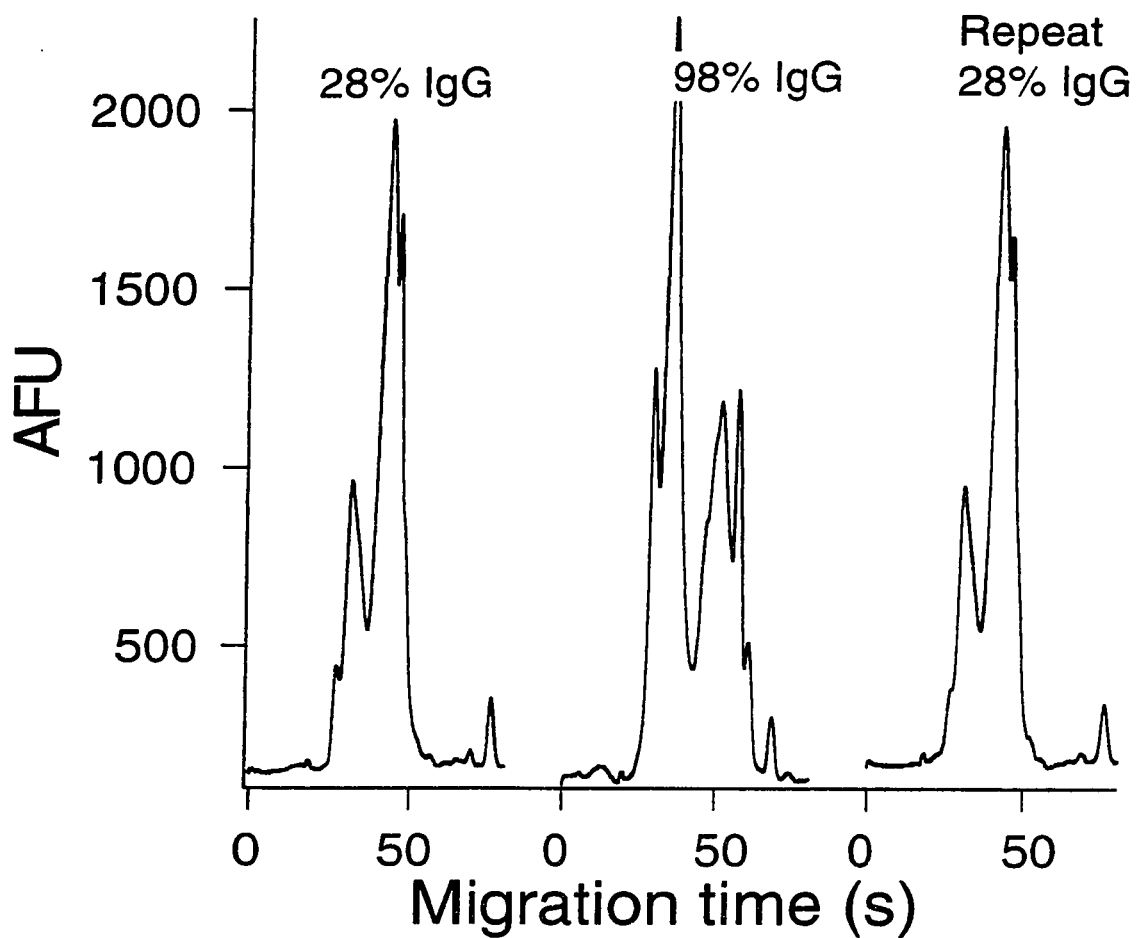


Figure 4-18 Sample carryover test showing no interference from the previous more concentrated sample.

4.4.3 Assessment of sample carryover

To check the system reproducibility, we tested for sample carryover. When preparing the calibration curve, we always started with the lowest anti-BSA concentration, and moved on to the higher concentration of anti-BSA. By doing so, we expected to minimize the cross-contamination of different concentrations. To make sure that there is no interference of the previous sample concentration, we carried out the signal measurement from low concentration to high concentration, and then repeated the low concentration, using voltages to control the concentrations. In Figure 4-18, the first trace represents the lower sample concentration, which was 28% of the stock anti-BSA concentration. The trace in the middle is from the higher sample concentration, 98% of the stock anti-BSA. Finally, the lower sample concentration, 28% of the stock anti-BSA, was reintroduced for measurement, and its trace is shown on the right side. Between the high and low concentrations, the channel was flushed with the buffer, which was stored on chip, in the reservoir 2*, for 5 minutes. Comparing the three traces, the first trace, 28% anti-BSA, had a small complex peak, and a large peak from free BSA*. In the second trace, where the anti-BSA amount increased to 98% of the stock solution, the complex peak increased dramatically, and the free BSA* dropped. The third trace was from the reintroduction of the lower concentration (28% of stock anti-BSA) and appeared to be almost identical to the first trace. The difference of intensity between the first and third traces was less than 2%.

From this sample carryover test, where we observed comparable results for the same concentration after a more concentrated sample was introduced to the system, we

are confident that there is no interference from the previous samples of the different concentrations. The system is stable and reliable under the voltage control we have described.

4.5 Conclusion

In this chapter, we demonstrated that we can use voltage to control delivery and mixing of three different reagents from the solutions stored on-chip. The linearity of the intensity vs. voltage/concentration plots show that we can deliver the required amounts of all reagents with the applied electric fields with proper device design and voltage configuration. With our immunoreactor, we showed that integrating the process of sample mixing, reaction, separation and detection can be achieved on the miniaturized glass device. On-board calibration was successfully performed, and tested with samples prepared off-chip to evaluate its reliability. Reproducibility was demonstrated with the sample carryover test, which proved that there was no interference from the previous more concentrated samples.

Our work showed good reliability and reproducibility, so this is a very valuable contribution to the clinical or field work wherever a calibration is necessary. The chip-based method would be useful when any reagent is in a very small amount and difficult to dilute to a series of different concentrations, or where it is not convenient to make a series of standard solutions with different concentrations on site.

References

- 1 Seiler, K.; Fan, Z.; Fluri, K.; Harrison, D.J., *Anal. Chem.* **66**, 3485, **1994**.
- 2 The relationship between R and geometry is $R=\rho l/A$, where ρ depends on a given electrolyte's resistivity and l and A are the channel's length and cross sectional area, respectively.
- 3 Halliday, D.; Resnick, R., *Physics J.* Wiley and Sons: New York, **1960**
- 4 Fan, Z.; Harrison, D.J., *Anal. Chem.* **66**, 174-184, **1994**
- 5 Fluri, K.; Fitzpatrick G.; Chiem, N.; Harrison, D.J., *Anal. Chem.*, **68**, 4285-4290, **1996**
- 6 Chiem N.; Harrison D.J., *Anal. Chem.*, **69**, 373-378, **1997**
- 7 Qiu, X.C., *Ph.D. Thesis*, Chapter 2, Univ. of Alberta, **1998**
- 8 Karger, B.L.; Snyder, L.R.; Horvath, C. *An Introduction to Separation Science*; J. Wiley and Sons: New York, **1973**;
- 9 Harrison, D.J.; Manz, A.; Fan, Z.; Ludi, H.; Widmer, H.M., *Anal. Chem.*, **64**, 1926-1932, **1992**
- 10 Harrison, D.J.; Fluri, K.; Seiler, K.; Fan, Z.; Effenhauser, C.S.; Manz, A., *Science*, **261**, 895-897, **1993**
- 11 Sweedler, J.V.; Shear, J.B.; Fishman, H.A.; Zare, R.N.; Scheller, R.H., *Anal. Chem.* **63**, 496-502, **1991**
- 12 Cheng, Y.F.; Dovichi, N.J., *Science*, **242**, 562, **1988**
- 13 Qiu, X.C., *Ph.D. Thesis*, Chapter 3, Univ. of Alberta, **1998**

Chapter 5

Conclusions and Suggestions for Future Work

The purpose of this chapter is to summarize the results from the previous chapters and suggest some of the continuing work which could be done in the future. Since there is a broad range of material in this thesis, I will discuss the results in the order of the chapters.

In Chapter 2, we discussed the leakage phenomenon, which could be measured using either bead velocity in the solvent or with a calibration curve made from the fluorescence intensity as a function of dye velocity. We found that the leakage is affected by the length of the side channel in both theoretical predictions and experimental studies. Both studies show that the leakage from the side channel decreases with increasing side channel length if the main channel length is fixed. As well the leakage is influenced by the side channel position along the main channel. With shorter side channel lengths, the leakage from the side channel decreased when the side channel was moved further away from the main channel inlet. However, with a longer side channel length, the measured leakage increased when the side channel was moved further along the main channel from the inlet. From both side channel length and position studies, we observed that the most symmetric design, where the side channel is located in the middle of the main channel,

and the side channel had half the length of the main channel, had the most ideal behavior, that is, there were no strong leakage or pushback effects. From this chapter, we achieved a better understanding for the microfluidic flow behavior, which should lay the foundation for design rules for the microfabricated devices. We also confirmed that the leakage and pushback phenomenon can be suppressed when the bias voltage is used.

We could further study leakage phenomenon quantitatively in the future. Also, our experimental data had some disagreement with the model prediction. Consequently, we may need to do some modifications to both the Model and the experimental work to solve these discrepancies. With the neutral fluorescent dye newly available we can perform a study on electroosmotic mobility measurement directly on-chip, which may give us better precision, and would definitely introduce less propagation of errors. The use of more direct methods to measure velocity, such as alternating sample and buffer plugs might also be useful.

It would be beneficial if we performed further studies on the channel geometry dependent fluidic mechanism. For instance, we would like to know how the angle of intersection of the two channels would be affected by the leakage phenomenon, and what is the best angle value for two intersecting channels.

In Chapter 3, we discussed how differing ζ potentials in intersecting channels would influence fluid flow. When the pH is different in the two intersecting channels, the flow velocities in the two channels are affected because of the mass balance requirement and the fact electroosmotic flow does not meet this demand. The side channel dye leakage measurements showed that when the main channel pH further deviated from the

dye pH value in the side channel, there would be more leakage. The measured dye velocity would further deviate from the predicted velocity, based on the electroosmotic mobility, when the pH difference was greater between the two streams. Also with the imbalanced ζ potential between the two streams, the measured dye velocity profile was unstable and unpredictable during an initial period the mixing occurred. The time showing the instability period is close to the period needed to flush the channel.

From this chapter, we learned that to achieve balanced and predictable mixing we need to have the the same ζ potential in intersecting channels. When the mixing streams have different pH, Poiseuille flow plays a significant role in the flow. Yet this ζ potential depend flow velocity effect is interesting and maybe useful if we have better and more quantitative understanding of this issue. In future, we may look into the device whose channels possess deliberately differently charged surface property. Such devices can be used to introduce two streams with different flow velocity, so that the different mixing ratio can be adjusted accordingly.

In Chapter 4 we performed immunological reactions on-chip and obtained on-board calibration with controlling voltages on the different channels. With the knowledge of the microfluidic mechanics described in Chapter 2 and 3, we designed voltage controlling programs with carefully calculated voltage values to achieve precise mixing and dilution processes. The diluted antibody was then mixed and reacted with a fixed concentration of antigen on-chip. A calibration curve was obtained with the different controlling voltages applied to the antibody and the buffer reservoirs, thus the concentration of the antibody introduced for reaction was varied. The calibration curve

showing that the signal of the reaction complex was linearly proportional to the concentration of the antibody after the dilution. This calibration curve was evaluated with off-chip prepared samples, and gave good accuracy. Sample carryover tests were also performed and the results showed that there was no cross contamination of the previous sample concentration in the mixing coil.

The results from this chapter suggest a promising future for automation on-chip. Approaching the final goal of miniaturized and portable micro-sensors, automation is a key role step forward. With the demonstrated success of the on-board calibration, we can move on to further work applying this technique to real applications, such as drug screening or in-field applications.